6-16-2016

# Test and Verification of a CubeSat Attitude Determination and Control System in Variable Magnetic Fields

Eric A. Bassett


# TEST AND VERIFICATION OF A CUBESAT ATTITUDE DETERMINATION AND CONTROL SYSTEM IN VARIABLE MAGNETIC FIELDS

THESIS

Eric A. Bassett, Captain, USAF

AFIT-ENY-MS-16-J-050

**DEPARTMENT OF THE AIR FORCE**
**AIR UNIVERSITY**

***AIR FORCE INSTITUTE OF TECHNOLOGY***

**Wright-Patterson Air Force Base, Ohio**

AFIT-ENY-MS-16-J-050

# TEST AND VERIFICATION OF A CUBESAT ATTITUDE DETERMINATION AND CONTROL SYSTEM IN VARIABLE MAGNETIC FIELDS

THESIS

Presented to the Faculty

Department of Aeronautics and Astronautics

Graduate School of Engineering and Management

Air Force Institute of Technology

Air University

Air Education and Training Command

in Partial Fulfillment of the Requirements for the

Degree of Master of Science of Astronautical Engineering

Eric A. Bassett, BS, MBA

Captain, USAF

June 2016

AFIT-ENY-MS-16-J-050

# TEST AND VERIFICATION OF A CUBESAT ATTITUDE DETERMINATION AND CONTROL SYSTEM IN VARIABLE MAGNETIC FIELDS

THESIS

Eric A. Bassett, BS, MBA
Captain, USAF

Committee Membership:

Dr. Eric D. Swenson
Chair

Dr. Richard G. Cobb
Member

Dr. Carl R. Hartsfield
Member

AFIT-ENY-MS-16-J-050

# Abstract

The Center for Space Research and Assurance (CSRA) at the Air Force Institute of Technology (AFIT) continues to explore CubeSat initiatives for solving many current space security issues. Regardless of the mission requirements, the success of the CubeSat on orbit frequently depends on the Attitude Determination and Control System (ADCS) functioning correctly. Previous research at AFIT has demonstrated single axis control on a spherical air bearing test bed incorporated within a Helmholtz cage utilizing artificially strong magnetic fields for better signal to noise ratios which are not experienced on orbit. This research explores the process of redesigning, testing, and programming a new 6U CubeSat ADCS to operate in representative magnetic fields using a three wheel reaction wheel array (RWA). A second external magnetometer is utilized while its effect on the quaternion estimate (QUEST) is characterized. The RWA is modularized and displaced from the ADCS $\mu$controller by the addition of a separate $\mu$controller on the RWA to handle Hall sensor interrupts allowing the control and estimation task to run uninterrupted. The displacement of the RWA from the primary ADCS $\mu$controller, which includes the primary magnetometer, minimizes electromagnetic disturbances caused by the RWA on the magnetometer. A quaternion error Proportional-Integral-Derivative (PID) control law is used to control the ADCS test bed while an external motion capture system captures its true orientation. This research effort shows that the quaternion estimate degrades as the magnetic field strength is reduced. The ambient Earth magnetic field increased the final angle error by 7.1° during a 90° rotation maneuver when compared to the maximum Helmholtz cage condition.

AFIT-ENY-MS-16-J-050

*To my wife and son, I love you both to the moon and back.*

# Acknowledgements

First and foremost I would like to thank my research adviser, Dr. Swenson for this research opportunity. I remember asking Dr. Swenson for a thesis project that involved $\mu$controllers and C code, a topic that I was not entirely comfortable with and lacked experience in besides the occasional weekend Arduino project. Dr. Swenson allowed me the freedom to make mistakes and learn from those experiences. His recommendations throughout the research helped me discover, troubleshoot, and learn from the many difficulties in my research.

Next, I would like to thank Philip Smith and Randall Sharp who always gave me professional mechanical insight. You two helped me construct and assemble the CubeSat and your camaraderie in the mechanical lab was greatly appreciated. I could not have done this research without the help, insight, and software wizardry of Matt Lippert. Thank you for your time and dedication to my research project. I'm pretty sure if we didn't get stuck in the mechanical lab during that lock-down exercise I wouldn't have achieved control of the testbed. Jamie Smith saved my research project by replacing the faulty air compressor just in time, thank you for your hard work and dedication to AFIT. Dr. Hartsfield and Capt. Hess also helped me throughout the project by offering insight into the QUEST algorithm and quaternion error calculations. I also want to thank Jay Anderson for his logistical help in obtaining supplies and test equipment.

Finally, I'd like to thank all my friends at AFIT who took the extra time to get me back up to speed academically. I couldn't have done this without you all.

Eric A. Bassett

# Table of Contents

Page

# List of Figures

# List of Tables

TEST AND VERIFICATION OF A CUBESAT ATTITUDE DETERMINATION AND CONTROL SYSTEM IN VARIABLE MAGNETIC FIELDS

# I. Introduction

## 1.1 Background and Motivation

The United States Air Force Institute of Technology (AFIT) Center for Space Research and Assurance (CSRA) continues to research and develop CubeSats for both academic and Department of Defense (DoD) related research initiatives. The CubeSat concept was originally developed in 1999 through collaboration between the Aerospace Departments of Stanford University and the California State Polytechnic University [6]. The standard 10 x 10 x 10 $cm^3$ cube has a volume of exactly one liter is expected to have a mass of 1.33 kg or less, and is referred to as a one unit "1U" [6]. Standardization of the CubeSat design was focused on lowering the cost of entry for other universities, government research incentives, and potential commercial sponsors. The scalability and common form factor of the CubeSat allows for rapid development and integration of necessary satellite subsystems and novel payloads. Initially, only 1U, 2U, and 3U systems were designed; but in the last few years 6U, 12U, and even 27U designs have been developed [7].

The explosive growth of the CubeSat mission domain from both universities and the commercial market has opened many opportunities for space research and experimentation. The DoD Space Test Program (STP) capitalizes on CubeSats through technology demonstrations and experiments that have a high potential for providing new warfighter capability or enhancing an existing capability at a much lower cost

than larger satellite programs [8]. However, CubeSats frequently come with some disadvantages such as higher mission risks, lack of redundancy, and poor estimation leading to degraded pointing capability [4]. Increasing the estimation and pointing accuracy of the larger "6U+" CubeSats would allow increased payload capability and on-orbit reliability. The estimation and pointing accuracy of the CubeSat is ultimately left to the attitude determination and control system (ADCS) used in the design. Although there are many capable commercial off-the-shelf (COTS) ADCS units available, AFIT continues testing in-house solutions for education and research purposes. The AFIT CubeSat test bed is enclosed in a Helmholtz cage as shown in Fig. 1.

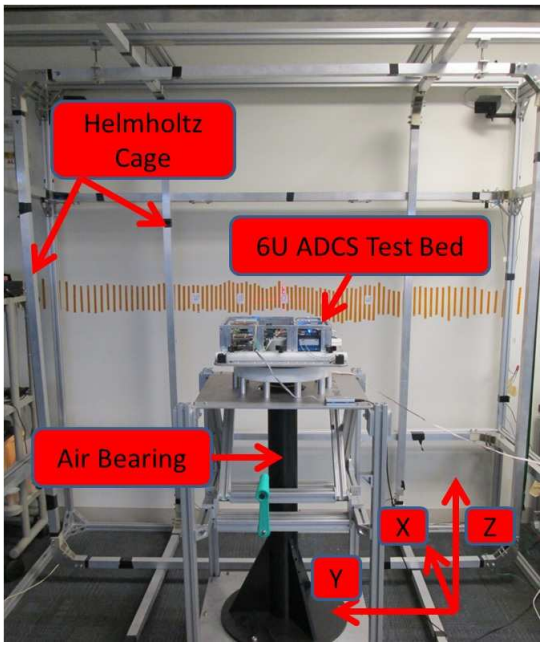


**Figure 1. AFIT CubeSat Test Bed**

The foundation of this research is based on previous work completed at AFIT by Brewer [9], Dannemeyer [3], Tibbs [4], et al. Brewer researched and constructed a Helmholtz cage (shown in Fig. 1) capable of producing custom static and dynamically changing magnetic fields for future CubeSat testing. Dannemeyer characterized the initial AFIT ADCS sensor and integrated the first AFIT 6U CubeSat command and

data handling (C&DH) and the electrical power subsystem (EPS) into the air bearing test bed. Tibbs' research focused on improving the pointing accuracy of the 6U test bed around the $z$-axis and was able to improve static estimation accuracy to $\pm 0.02^o$ ($\pm 3\sigma$).

The previous research involving CubeSat ADCS testing at AFIT utilized the Helmholtz cage with settings which provided artificially strong magnetic fields. These field strengths are approximately four times (6 dB higher) the ambient magnetic field strength of the Earth at sea level. Brewer initially discovered that the magnetometer showed increased noise levels when located within two inches of the reaction wheel motors [9]. Further testing showed that the magnetometer installed on the ADCS in previous research efforts may have been heavily influenced by electromagnetic interference (EMI) generated from the RWA motors. An accuracy of $\pm 20^o$ could be obtained with the ADCS test bed without adding bias to the magnetometer [3]. Obtaining an improvement in pointing accuracy with the addition of magnetometer biasing based on wheel speed signifies that there was significant EMI inherent within the ADCS [4].

The motivation for this thesis ultimately stemmed from AFIT's goal of producing an indigenous low-cost flight-worthy ADCS for future CubeSat missions. In order to accomplish this task, the ADCS must operate correctly with magnetic fields similar to that on orbit. CubeSats are typically released into a low Earth orbit (LEO) which exhibits a weaker magnetic field than the ambient field near the Earth's surface [10]. This research attempts to eliminate various sources of internal noise (EMI) from the ADCS, to experiment with the addition of a secondary external magnetometer, and to apply smoothing filters to improve the overall attitude determination accuracy.

## 1.2 Problem Statement

Prior to this research, the AFIT ADCS could only exhibit single axis control about the $z$-axis, relying on Euler angles which admit singularities at certain orientations. A quaternion was calculated in real time, but was not used for attitude control. The quaternion estimate from QUEST needed to be investigated and improved with the installation of a third sensor vector from an external magnetometer. The $x$- and $y$-axis controllers also needed to be programmed and implemented. Furthermore, the EMI from the brushless direct current (BLDC) motors on the ADCS needs to be reduced to improve magnetometer sensor data quality. Other sources of system noise must also be found and removed to allow the ADCS test bed to provide an accurate attitude estimate. Reconfiguration of the ADCS along with better filtering of the sensor data will mitigate some of the issues experienced in previous research. The ADCS must demonstrate functionality in a more realistic magnetic field if a final flight-ready AFIT ADCS is to become a reality. Finally, the accuracy of the ADCS should also be compared to an external truth source to confirm whether or not the system is estimating the attitude accurately.

## 1.3 Research Objectives

The primary objective of this thesis is to research the accuracy of the attitude estimate of the AFIT ADCS and to compare this estimate with an external truth source for verification. The secondary objective is to evaluate the ability to perform a $360^o$ control around the $z$-axis using a quaternion-based proportional-integral-derivative (PID) controller. To achieve the research objectives, an attempt was made to remove EMI and other sources of interference on the ADCS which degrades attitude estimation and control authority. The moving average filter previously used was compared to and replaced by a discrete-time Kalman filter to smooth sensor data. Finally,

three-axis PID control was evaluated for future ADCS development at AFIT.

## 1.4 Methodology

The AFIT 6U CubeSat ADCS test bed was modified to physically displace the reaction wheel assembly (RWA) from the magnetometer. A secondary $\mu$controller was integrated to alleviate real-time operating system (RTOS) interrupt commands from the RWA motor's Hall sensors. An additional external magnetometer was installed and tested to verify if an additional sensor would improve attitude estimation accuracy. The reconfigured test bed was reprogrammed to include new filtering methods, a three-axis quaternion-based PID controller, and better RWA speed control through the second $\mu$controller. The 6U ADCS test bed was then tested in various maneuvers with differing magnetic field settings. The state data was recorded and compared against a newly installed external PhaseSpace 3D motion capture system providing calibrated truth measurements of the CubeSat's ADCS test bed attitude.

## 1.5 Assumptions and Limitations

Due to the limited time available for development of custom electronics packages and mechanical assemblies at AFIT, there are a few notable assumptions and limitations that still must be addressed. The use of rapid prototyped 3D printed mechanical attachments, custom wire harnesses, and makeshift solutions in order to successfully integrate all necessary components in time for testing adds some level of uncertainty into the research. For example, the moment of inertia (MOI) of the CubeSat is never truly known or kept static as wires and system components are constantly being rearranged and repaired throughout testing. The addition of the PhaseSpace light emitting diode (LED) control package as described in section 3.3.1 also changes the MOI and may or may not cause additional EMI. For the purpose of this research,

the small changes in MOI and potential for additional EMI are considered negligible. There also exist some physical limitations of the ADCS CubeSat test bed; most notable is the mass of the spherical air bearing and CubeSat assembly in relation to the center of rotation (CoR) depicted in Fig. 2.

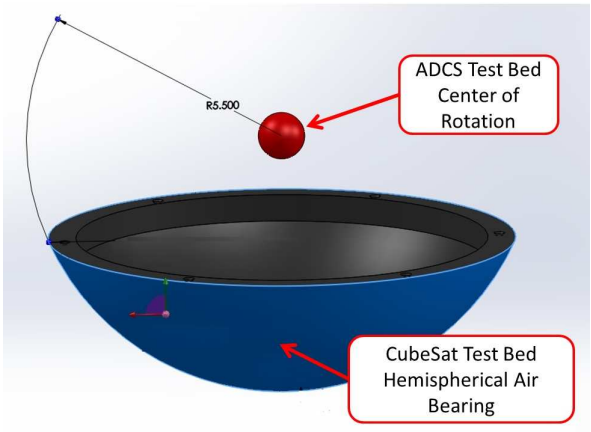


**Figure 2. Air Bearing Test Bed Center of Rotation**

To prevent damage to the 6U CubeSat test bed, the CubeSat must be securely attached to the air bearing attachment plate. To remain in a stable orientation during air bearing operation the entire systems center of mass (CoM) must remain below the 5.5 inch CoR shown in Fig. 2. An attempt was made to bring the CoM as close as possible to the CoR, but the constant movement of the PhaseSpace test equipment to the CubeSat further changed this displacement. The displacement between the CoR and CoM ultimately limits the CubeSat's control authority about the $x$- and $y$-axes as the motors cannot provide enough torque to overcome the moment generated by gravity. As this research aims to implement three-axis control the only observed result will be reduced nutation (nodding, swaying, or wobble) about the $x$- and $y$-axes.

### 1.6 Expected Outcomes

Based on the previous research performed by Tibbs', reconfiguring the RWA away from the magnetometer should mitigate the need for sensor bias in the ADCS soft-

ware allowing for control in an ambient (low SNR) magnetic field. The addition of the second $\mu$controller should also result in better reaction wheel speed control and improve the primary ADCS functionality by eliminating Hall sensor interrupts from the motors. With the addition of the three-axis PID controller it is expected that the noticeable wobble during past testing on the air bearing can be removed. With the improvements made in this research the expected controllable range around the $z$-axis can be increased significantly. However, the addition of the secondary magnetometer may deteriorate the accuracy of the ADCS test bed attitude estimation as this sensor is lower in quality than the primary magnetometer.

## 1.7 Thesis Overview

Chapter I provided the background and motivation for the research topic. This chapter also presents the problem statement, research objectives, methodology, and limitations related to researching the 6U AFIT ADCS. Chapter II documents the background theory necessary to operate and test a CubeSat ADCS and provides fundamental equations and theory relevant to the design and implementation of a working ADCS. It also includes a literature review of related research from other universities working on CubeSat test beds. Chapter III outlines the methodology used to configure, test, and verify the AFIT 6U ADCS test bed. The chapter focuses on the hardware and software implementation used in this research and provides an outline of the testing to be performed. Chapter IV documents the analysis and results from the experiments conducted in this research. Finally, Chapter V summarizes the conclusions of this research effort and offers recommendations for future work on the CubeSat ADCS test bed.

# II. Theory

This chapter presents the fundamental requirements and supporting theory necessary for a modern spacecraft's attitude determination and control subsystem (ADCS). In order to establish notation for the reader, the first section reviews coordinate frames, rotation matrices, Euler angles, and quaternions. The second section develops the kinetic and kinematic equations of motion (EOM) needed for utilization of the reaction wheels for attitude control. The third section covers various methods of attitude estimation with the development of a discrete-time based Kalman filter for use on the AFIT 6U CubeSat ADCS controller card. Finally, the last section provides a literature review of relevant work relating to attitude determination and control systems for CubeSats.

## 2.1 Spacecraft Attitude Concepts

Almost all spacecraft must accurately estimate their current attitude relative to an external frame of interest and to control its attitude with respect to that frame autonomously on orbit. Various sensor suites, optics packages, communication equipment, tracking devices and even solar panels perform their primary function requiring precise pointing. For this reason, it is the primary responsibility of the ADCS to accurately estimate and control the spacecraft's attitude to effectively employ one or more of these primary functions, sometimes in concert with opposing priorities. To compute the control and determination tasks accurately and in a timely manner, a microprocessor or $\mu$controller is commonly used. In order to program these devices, the mathematical relationships between coordinate frames and the parameters used between them must be defined.

### 2.1.1 Coordinate Frames

In order to solve for the orientation of a spacecraft in orbit, various coordinate frames must be defined. The following coordinate frames are all based on the Cartesian coordinate system. These coordinate frames are orthogonal, have right angles, and follow the right-hand rule.

#### 2.1.1.1 Spacecraft Body and Orbital Frames

The spacecraft body frame $\hat{b}$ can be defined by the user or designer of the satellite. Oftentimes, it is easier to have the body frame defined to have its origin at the CoM and its axes aligned with the spacecraft's principal MOI. The spacecraft fixed body and orbital frames are commonly associated with the "roll-pitch-yaw" series when applied to manned spacecraft, such as the space shuttle [11, 12]. The spacecraft fixed frame and the orbital frame are both non-inertial reference frames and can be denoted with $\hat{b}_{123}$ and $\hat{o}_{123}$, respectively, as shown in Fig. 3.

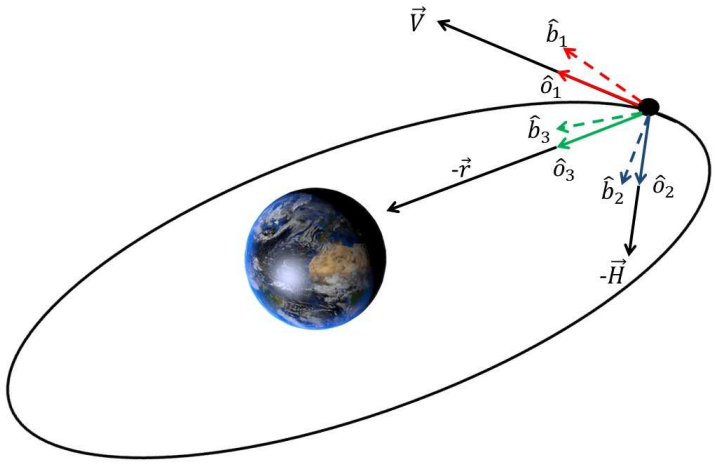


**Figure 3. Spacecraft Body Fixed and Orbital Coordinate Frame**

The shorter solid lines in the figure represent the orbital frame while the dashed lines represent the spacecraft fixed body frame. The $\hat{o}_3$ axis is aligned with the nadir

direction, while the $\hat{o}_2$ axis is in the negative orbit normal direction. The $\hat{o}_1$ axis completes the triad and is coincident with of the velocity vector for circular orbits. The spacecraft body $\hat{b}$ frame axes usually follows the same attitude convention as the orbital frame, but is largely dependent on the mission and design of the spacecraft and changes with respect to the $\hat{o}$ frame [6]. For the space shuttle the spacecraft fixed body $\hat{b}_1$ is the parallel to the orbital structural body axis (positive towards the nose) [12]. The $\hat{b}_2$ axis is referred to as the pitch, while the $\hat{b}_3$ can represent the yaw. The vector representation can be defined as where $\vec{v}_b$ and $\vec{v}_o$ represent the body frame and orbital frames respectively. Likewise with these frames, it is not terribly important how they are defined, but only that they are well known and can be easily converted to other coordinate systems.

#### 2.1.1.2 Sensor Frame

The sensor frame is a non-inertial coordinate system typically aligned with the sensor or actuator. The $x$- and $y$-axes are typically in a predefined sensor plane and form a right-handed orthogonal system which aligns the $z$-axis as the boresight of the sensor [12]. The primary sensor used in this research is the Analog Devices ADIS16405 IMU and is represented in Fig. 4. along with its coordinate system. If the sensor is deployable; such as the solar panel example given earlier, the expected final orientation relative to the spacecraft body frame may be different than designed. Other issues on orbit may also cause errors in the sensors position such as micro-meteorite impacts. For this reason, care must be taken to account for partial deployments and other misalignments in the sensor coordinate system during movement or deployment [6]. Vibrations encountered during the launch phase may also cause displacement of the sensor with respect to the designed orientation and may adversely affect the accuracy of the sensor during use. It should be noted that the

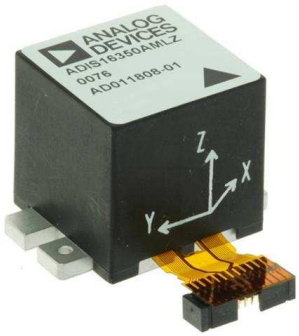


**Figure 4. Analog Devices ADIS16405 IMU with Sensor Fixed Frame Printed on the Side**

application and handling of the sensor frame nomenclature does not solely apply to data collection sensors. Additional frames can be defined in the spacecraft for devices such as reaction wheels, magnetometers, magnetic torque rods, propulsion systems, antennas, and potentially many other devices.

#### 2.1.1.3 Earth-Centered Inertial and Earth-Centered Earth Fixed

The Earth-Centered Inertial (ECI) and Earth-Centered Earth Fixed (ECEF) frames both have origins at the center of mass of the Earth. The ECI frame is considered inertial, but in reality it should be considered pseudo- or quasi-inertial [13], as the spin axis of Earth actually exhibits precession and nutation due to perturbations from the Moon and other planets. The ECI and ECEF frames can be seen in Fig. 5 where the *X, Y,* and *Z* components define the ECI frame, while the *X', Y'* and *Z'* components represent the ECEF frame. *X* is directed towards of the first point of Aries on the vernal equinox for the ECI frame, and *X'* is through the Greenwich meridian (zero longitude) for the ECEF frame. The angle $\theta_g$ is the Greenwich Sidereal Time. The *Z*- and *Z'*- axes are coincident with the Earth's rotational axis and are positive north for both frames, while the *Y* and *Y'* axes are both defined in the equatorial plane by completing the right-handed orthogonal sets. The derivatives in

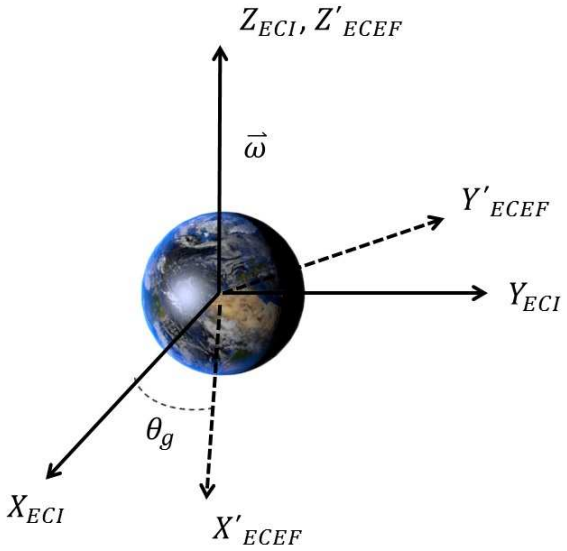


**Figure 5. The Earth-Centered Inertial and Earth-Centered-Earth-Fixed Reference Frames**

the kinetic and kinematic EOM must be computed with respect to an inertial frame. For this reason, the EOMs for this research are derived in the ECI frame, but are tailored for use in the ADCS test bed at AFIT which will be discussed in greater detail in Chapter III.

### 2.1.2 Euler Angles and the Rotation Matrix

As alluded to earlier, it is a common requirement to transform the information from one coordinate system to another more useful reference frame. In the case of spacecraft attitude, the driving EOM are most useful in an body frame where Newton's laws of motion can be modeled mathematically much easier as the MOI stay fixed for rigid bodies. One of the most widely used parametrization of this transformation is through the use of Euler angles [14]. Euler angles describe the orientation of one frame relative to another frame. Leonhard Euler first suggested the use of a sequence of three simple rotations to describe the orientation of one reference frame to another frame. These three rotations can be shown to be the

minimum number of independent parameters to fully describe any three dimensional rotation [15]. A graphical representation of the commonly used 3-2-1 rotation through the angles $(\varphi, \theta, \phi)$ is shown in Fig. 6.

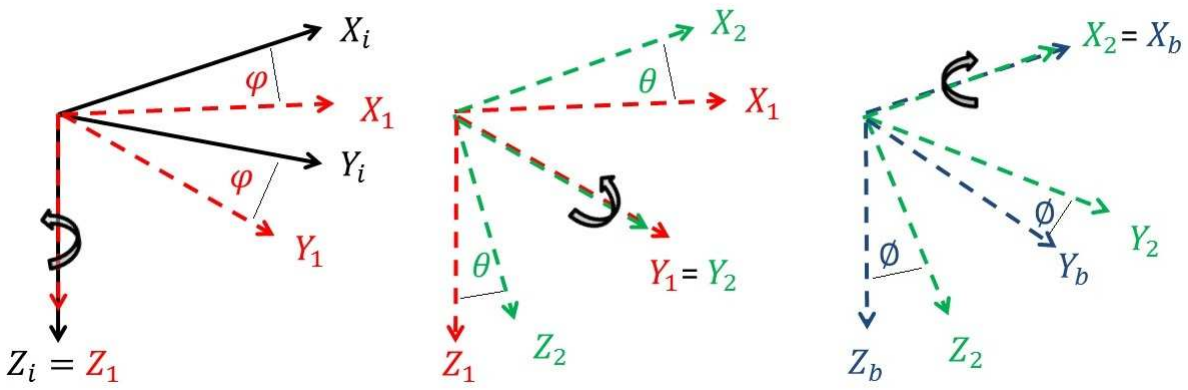


**Figure 6. 3-2-1 Euler Rotation Sequence**

The 3-2-1 rotation is also referred to as the yaw-pitch-roll rotation [13], noting in Fig. 6 it is shown as the $Z_1$-$Y_2$-$X_b$ rotation. The original inertial coordinate system $X_i, Y_i, Z_i$ is first rotated about $Z_i$ which is considered the 3 or yaw axis by angle $\varphi$. Second the new intermediate coordinate frame $X_1, Y_1$, and $Z_1$, is rotated around the 2 or pitch axis $Y_1$ by an angle $\theta$. Finally, the newest intermediate frame $X_2, Y_2$, and $Z_2$ is rotated about the 1 or roll axis $X_2$ by angle $\phi$ becoming the final coordinate system in the body frame $X_b, Y_b, Z_b$. Each frame is related by a rotation matrix $\boldsymbol{R}$ commonly called the direction cosine matrix (DCM). The rotation matrices for the three successive rotations shown in Fig. 6 can be expressed in order as

$$\boldsymbol{R_3^{1i}} = \begin{bmatrix} \cos\varphi & \sin\varphi & 0 \\ -\sin\varphi & \cos\varphi & 0 \\ 0 & 0 & 1 \end{bmatrix} \tag{1}$$

$$\boldsymbol{R_2^{21}} = \begin{bmatrix} \cos\theta & 0 & -\sin\theta \\ 0 & 1 & 0 \\ \sin\theta & 0 & \cos\theta \end{bmatrix} \tag{2}$$

$$\boldsymbol{R_1^{b2}} = \begin{bmatrix} 1 & 0 & 0 \\ 0 & \cos\phi & \sin\phi \\ 0 & -\sin\phi & \cos\phi \end{bmatrix} \tag{3}$$

where the superscripts on the rotation matrix $\boldsymbol{R}$ are read from right to left. These depict which direction with respect to the coordinate frame the rotation matrix is acting on and the subscript depicts which axis the rotation occurs. The final rotation matrix that transforms an arbitrary vector from the inertial frame to the body frame can be seen as

$$\boldsymbol{R^{bi}} = \boldsymbol{R_1^{b2}}\phi\boldsymbol{R_2^{21}}\theta\boldsymbol{R_3^{1i}}\varphi \tag{4}$$

where the order of matrix multiplication is crucial for an accurate transformation between frames [15]. The rotation matrix $\boldsymbol{R^{bi}}$ is an orthonormal transformation, meaning that the angles and lengths are preserved. Because the transformation is orthonormal, the rotation matrix exhibits some useful properties. Although a rotation matrix has nine values, it only has three degrees of freedom. There are a total of six constraints on any rotation matrix; three being that each column have magnitude of one and the other three constraints are that the columns must be orthogonal [15]. One of the most useful properties of the rotation matrix is such that the inverse of $\boldsymbol{R^{bi}}$ is equal to its transpose [13] shown as

$$(\boldsymbol{R^{bi}})^T = (\boldsymbol{R^{bi}})^{-1} = \boldsymbol{R^{ib}} \tag{5}$$

where the rotation matrix denoted $\boldsymbol{R^{ib}}$ can transform a vector from the body frame into the inertial frame. Combining Eqs. (1-3) and multiplying properly as shown in Eq. (4) the final rotation matrix $\boldsymbol{R^{bi}}$ is given by

$$\boldsymbol{R^{bi}} = \begin{bmatrix} \mathrm{c}\varphi\mathrm{c}\theta & \mathrm{c}\theta\mathrm{s}\varphi & -\mathrm{s}\theta \\ \mathrm{c}\phi\mathrm{s}\theta\mathrm{s}\varphi - \mathrm{c}\phi\mathrm{s}\varphi & \mathrm{c}\phi\mathrm{c}\varphi + \mathrm{s}\phi\mathrm{s}\theta\mathrm{s}\varphi & \mathrm{s}\phi\mathrm{c}\theta \\ \mathrm{c}\varphi\mathrm{c}\phi\mathrm{s}\theta + \mathrm{s}\phi\mathrm{s}\varphi & \mathrm{c}\phi\mathrm{s}\theta\mathrm{s}\varphi - \mathrm{s}\phi\mathrm{c}\varphi & \mathrm{c}\phi\mathrm{c}\theta \end{bmatrix} \tag{6}$$

where c and s are shorthand notation for the cosine and sine of the angle, respectively. From Eq. (6) it can be shown that the three Euler angles can possibly be recovered by [16]

$$\theta = \sin^{-1}(-\boldsymbol{R^{bi}_{13}}) \tag{7}$$

$$\varphi = \sin^{-1}\left(\frac{\boldsymbol{R^{bi}_{12}}}{\cos\theta}\right) \tag{8}$$

$$\phi = \sin^{-1}\left(\frac{\boldsymbol{R^{bi}_{23}}}{\cos\theta}\right) \tag{9}$$

where the subscripts on $\boldsymbol{R^{bi}}$ are the row and column entity from Eq. (6), respectively. Eqs. (7-9) can be used to recover the Euler angles, but are only valid for the 3-2-1 rotation matrix. In total, there are twelve unique rotation matrices utilizing the three Euler angles. A singularity occurs for this specific Euler rotation (and all other asymmetric rotations) when $\theta$ is either 90° or 270°. For symmetric rotations; the singularity develops when $\theta$ is 0° or 180° [11]. This singularity results from a divide by zero error, where the two of three required angles are undefined. Although a random orientation would be unlikely to land directly on a singularity during an Euler rotation; the errors resulting from processing this information on-board a spacecraft could be unrecoverable and even catastrophic. Due to the potential for singularities

to arise and along with the high computational cost of performing trigonometric calculations with Euler angles, they are not the ideal attitude representation onboard a spacecraft ADCS system. These singularities led to the development of a singularity-free attitude representation parameterization commonly called the quaternion.

### 2.1.3 Euler's Theorem, Quaternions, and Rodrigues Parameters

Although the Euler angle sequence of rotations is relatively easy to visualize and develop, it is not the most efficient approach for spacecraft dynamics [11]. Euler's Theorem states that the most general motion of a rigid body with a fixed point is a rotation about a fixed axis. This fixed axis is denoted by a 3 x 1 unit vector $\hat{\mathbf{a}}$ and is called the *Euler* axis, or the *eigenaxis*. Instead of three angles, there is only one, denoted $\Phi$, which is called the *Euler angle* or the *Euler principal angle* [11].

The rotation matrix $\boldsymbol{R^{bi}}$ which performs the same rotation as the 3-2-1 Euler angle sequence is then given in terms of $\Phi$ and $\hat{\mathbf{a}}$ by

$$\boldsymbol{R^{bi}} = \cos\boldsymbol{\Phi}1 + (1 - \cos\boldsymbol{\Phi})\mathbf{a}\mathbf{a}^{\mathbf{T}} - \sin\boldsymbol{\Phi}\mathbf{a}^{\times} \tag{10}$$

where $\mathbf{a}^{\times}$ is the skew-symmetric matrix. Given only the rotation matrix $\boldsymbol{R^{bi}}$ from Eq. (6) the components $\boldsymbol{\Phi}$ and $\hat{\mathbf{a}}$ can be computed from

$$\boldsymbol{\Phi} = \cos^{-1}\left[\tfrac{1}{2}\mathrm{tr}\boldsymbol{R} - 1\right] \tag{11}$$

$$\mathbf{a}^{\times} = \frac{1}{2\sin\boldsymbol{\Phi}}(\boldsymbol{R}^T - \boldsymbol{R}) \tag{12}$$

where "tr" is simply the trace of the matrix. From $\boldsymbol{\Phi}$ and $\hat{\mathbf{a}}$ the four quaternion parameters or Euler parameters are then defined by

$$\mathbf{q} = \mathbf{a}\sin\frac{\Phi}{2} \tag{13}$$

$$q_4 = \cos\frac{\Phi}{2} \tag{14}$$

where $\mathbf{q}$ is a 3 x 1 matrix which contains the *Euler axis component* of the quaternion. The $q_4$ is a scalar component of the full quaternion set denoted $\bar{\mathbf{q}}$ defined as

$$\bar{\mathbf{q}} = \begin{bmatrix} q_1 \\ q_2 \\ q_3 \\ q_4 \end{bmatrix} = [\mathbf{q}^T q_4]^T. \tag{15}$$

The use of the quaternion for parametrization of spacecraft attitude is preferred as it lacks a singularity condition [17]. However, the four parameters are not independent of each other, but are constrained by

$$\mathbf{q^T q} + q_4^2 = [q_1^2 + q_2^2 + q_3^2 + q_4^2]^{\frac{1}{2}} = 1 \tag{16}$$

because the Euler axis $\hat{\mathbf{a}}$ is a unit vector such that $[a_1^2 + a_2^2 + a_3^2]^{\frac{1}{2}} = 1$ [17]. Likewise with the Euler axis and the Euler angle, the quaternion can also be used to construct $\boldsymbol{R^{bi}}$ using

$$\boldsymbol{R^{bi}} = (q_4^2 - \mathbf{q^T q})\mathbf{I} + 2\mathbf{q}\mathbf{q}^T - 2q_4\mathbf{q}^\times \tag{17}$$

where $\mathbf{I}$ is a 3 x 3 identity matrix and $\mathbf{q}^\times$ is a 3 x 3 skew-symmetric matrix constructed from $\mathbf{q}$. It is also useful to express the quaternion from the elements in $\boldsymbol{R^{bi}}$ as

$$q_4 = \pm\frac{1}{2}\sqrt{1 + \mathrm{tr}\boldsymbol{R}} \tag{18}$$

which can be quickly computed on-board a spacecraft's ADCS. Since the goal is to ultimately control the attitude of the spacecraft; the error between the current and

desired attitude must be found. This error, denoted $\bar{\mathbf{q}}_\mathbf{e}$, is related to the present quaternion $\bar{\mathbf{q}}_\mathbf{p}$ and the desired commanded quaternion $\bar{\mathbf{q}}_\mathbf{c}$ by

$$\bar{\mathbf{q}}_\mathbf{p} = \begin{bmatrix} q_{4c} & -q_{3c} & q_{2c} & q_{1c} \\ q_{3c} & q_{4c} & -q_{1c} & q_{2c} \\ -q_{2c} & q_{1c} & q_{4c} & q_{3c} \\ -q_{1c} & -q_{2c} & -q_{3c} & q_{4c} \end{bmatrix} \bar{\mathbf{q}}_\mathbf{e} = \tilde{\boldsymbol{M}}(\bar{\mathbf{q}}_\mathbf{c})\bar{\mathbf{q}}_\mathbf{e} \tag{19}$$

where the 4 x 4 matrix $\tilde{\boldsymbol{M}}(\bar{\mathbf{q}}_\mathbf{c})$ is orthonormal and typically called the quaternion transmuted matrix [17]. Since the $\tilde{\boldsymbol{M}}(\bar{\mathbf{q}}_\mathbf{c})$ matrix is orthonormal, taking the inverse is simply the transpose. Then the quaternion error $\bar{\mathbf{q}}_\mathbf{e}$ is obtained directly by

$$\bar{\mathbf{q}}_\mathbf{e} = (\tilde{\boldsymbol{M}}(\bar{\mathbf{q}}_\mathbf{c}))^{-1}\bar{\mathbf{q}}_\mathbf{p} = (\tilde{\boldsymbol{M}}(\bar{\mathbf{q}}_\mathbf{c}))^{T}\bar{\mathbf{q}}_\mathbf{p} \tag{20}$$

which can be used in a feedback control loop to minimize the difference between the desired and current quaternion [18]. The final attitude parameter to be presented is the Rodrigues parameter, sometimes called the Gibbs parameter or vector [17]. The usefulness of this parameter will become apparent later in this chapter when methods of quaternion estimation are presented. The Rodrigues vector $\mathbf{p}$ is defined by

$$\mathbf{p} = \begin{bmatrix} p_1 \\ p_2 \\ p_3 \end{bmatrix} = \begin{bmatrix} q_1/q_4 \\ q_2/q_4 \\ q_3/q_4 \end{bmatrix}. \tag{21}$$

From a given rotation matrix $\boldsymbol{R}$, the Rodrigues parameters can be calculated from

$$\begin{bmatrix} p_1 \\ p_2 \\ p_3 \end{bmatrix} = \frac{1}{1 + R_{11} + R_{22} + R_{33}} \begin{bmatrix} R_{23} - R_{32} \\ R_{31} - R_{13} \\ R_{12} - R_{21} \end{bmatrix}. \tag{22}$$

where again the subscripts on the $R$ are the position within the rotation matrix. The full rotation matrix $\boldsymbol{R}$ can also be reconstructed from only the Rodrigues parameters if needed, but is not used in this research. The interested reader is referred to [17].

## 2.2 Spacecraft Attitude Dynamics

This section describes the fundamental concepts of spacecraft attitude kinematics and kinetics. It builds from the past section's discussion on the existence of a singularity from an Euler rotation. The Kinematic EOM are derived and a kinematic singularity is exposed which leads to the introduction of the kinematic EOM utilization of quaternions. The second portion of this section formulates the three coupled nonlinear Euler equations for use in describing spacecraft rigid body rotations. The last portion describes how reaction wheels can be utilized to control the attitude orientation.

### 2.2.1 Spacecraft Kinematic Equations of Motion

The previous section described the use of the rotation matrix when defining a spacecraft's attitude. This same rotation matrix plays a similar role when developing the rotational EOMs as the relative rotation of each frame must be accounted for when taking a time derivative in the inertial frame [15]. The kinematic EOM relates the body frame to the inertial frame in terms of angular velocity $\vec{\omega}$ or $\vec{\omega}^{bi}$, which is written interchangeably in this document. The instantaneous angular velocity of the spacecraft in the body frame is defined

$$\vec{\omega} = \omega_1 \hat{b}_1 + \omega_2 \hat{b}_2 + \omega_3 \hat{b}_3 \tag{23}$$

were $\omega_1$, $\omega_2$ and $\omega_3$ are the scaler body axis components of angular rate in the body frame from Eq. (2). Using the Euler angles from the previous section and adding the

angular rates from each intermediate frame results in

$$\vec{\omega}^{bi} = \vec{\omega}^{b2} + \vec{\omega}^{21} + \vec{\omega}^{1i} \tag{24}$$

where $\vec{\omega}^{b2}$, $\vec{\omega}^{21}$, and $\vec{\omega}^{1i}$ are the angular rates from each intermediate frame in the 3-2-1 Euler rotation. This can be calculated by

$$\begin{bmatrix} \omega_1 \\ \omega_2 \\ \omega_3 \end{bmatrix} = \begin{bmatrix} \dot{\phi} \\ 0 \\ 0 \end{bmatrix} + \boldsymbol{R_1^{b2}}(\phi) \begin{bmatrix} 0 \\ \dot{\theta} \\ 0 \end{bmatrix} + \boldsymbol{R_1^{b2}}(\phi)\boldsymbol{R_2^{21}}(\theta) \begin{bmatrix} 0 \\ 0 \\ \dot{\varphi} \end{bmatrix} \tag{25}$$

where $\boldsymbol{R_1^{b2}(\phi)}$ and $\boldsymbol{R_2^{21}(\theta)}$ are rotations defined in Eqs. (1-3). After performing the multiplications and adding the resulting angular rate in the body frame becomes

$$\begin{bmatrix} \omega_1 \\ \omega_2 \\ \omega_3 \end{bmatrix} = \begin{bmatrix} -\sin\theta & 0 & 1 \\ \cos\theta\sin\phi & \cos\phi & 0 \\ \cos\theta\cos\phi & -\sin\phi & 0 \end{bmatrix} \begin{bmatrix} \dot{\varphi} \\ \dot{\theta} \\ \dot{\phi} \end{bmatrix} = \boldsymbol{S}\omega \tag{26}$$

and after taking the inverse of $\boldsymbol{S}$ the kinematic differential equations become

$$\begin{bmatrix} \dot{\varphi} \\ \dot{\theta} \\ \dot{\phi} \end{bmatrix} = \boldsymbol{S}^{-1}\omega \tag{27}$$

for the 3-2-1 Euler sequence. Noticing that a kinematic singularity occurs when $\theta = \pi/2$ or $3\pi/2$ which is problematic on board a spacecraft [11]. To avoid this singularity, the kinematic equations of motion are defined in terms of quaternions by

$$\dot{\mathbf{q}} = \begin{bmatrix} \dot{q_1} \\ \dot{q_2} \\ \dot{q_3} \\ \dot{q_4} \end{bmatrix} = \frac{1}{2} \begin{bmatrix} q_4 & -q_3 & q_2 & q_1 \\ q_3 & q_4 & -q_1 & q_2 \\ -q_2 & q_1 & q_4 & q_3 \\ -q_1 & -q_2 & -q_3 & q_4 \end{bmatrix} \begin{bmatrix} \omega_1 \\ \omega_2 \\ \omega_3 \\ 0 \end{bmatrix} \tag{28}$$

which can be rewritten in terms of only $\mathbf{q}$ and $\vec{\omega}$ by

$$\dot{\bar{\mathbf{q}}} = \frac{1}{2} \begin{bmatrix} \mathbf{q}^{\times} + q_4 \mathbf{I_{3x3}} \\ -\mathbf{q}^T \end{bmatrix} \vec{\omega} = \mathbf{Q}(\bar{\mathbf{q}})\omega \tag{29}$$

where again, the skew symmetric 3 x 3 matrix $\mathbf{q}^{\times}$ is used and $\mathbf{I_{3x3}}$ is the identity matrix. In the case for a *strapdown inertial reference system*, the body rates $\omega_1$, $\omega_2$, and $\omega_3$ can be measured directly from rate gyroscopes [17] although these devices are very susceptible to rate drift [11]. Without a kinematic singularity, the quaternion-based EOMs are clearly more useful in satellite attitude control applications.

### 2.2.2 Spacecraft Kinetic Equations of Motion

The previous section focused on the kinematic EOMs, this section will derive the kinetic EOM otherwise known as Euler's equations. The kinetic EOM provide the relationship between the spacecraft's mass moment of inertia (MOI), torque, angular rate, and angular acceleration in order to control and change the spacecraft's attitude. The 3 x 3 MOI matrix is a second-order tensor with all nine values constant if the spacecraft is assumed to be a rigid body. However, in reality no spacecraft is truly a rigid body as liquid fuel tends to slosh, solar panels may flex, and objects may be expended or extended/retracted intentionally or unintentionally [19]. For this research, the MOI will be assumed constant and measured only after the CubeSat test bed is finalized. The 3 x 3 MOI matrix will be assumed to be about the principal

axis so it is a diagonal matrix of the form

$$\boldsymbol{J_b} = \begin{bmatrix} J_{11} & J_{12} & J_{13} \\ J_{21} & J_{22} & J_{23} \\ J_{31} & J_{32} & J_{33} \end{bmatrix} = \begin{bmatrix} J_{xx} & 0 & 0 \\ 0 & J_{yy} & 0 \\ 0 & 0 & J_{zz} \end{bmatrix} \tag{30}$$

where $J_{xx}$, $J_{yy}$, and $J_{zz}$ are known as the scalar moments of inertia. The off-diagonal terms are known as the products of inertia [16]. Once the MOI matrix is determined the angular momentum $\vec{H}_b$ in the body frame, is then given by [15]

$$\vec{H}_b = \boldsymbol{J_b}\vec{\omega} = \begin{bmatrix} J_{xx}\omega_1 \\ J_{yy}\omega_2 \\ J_{zz}\omega_3 \end{bmatrix} \tag{31}$$

where the right-hand side is greatly simplified for the case when the principal axis of the spacecraft is used. Next, the time derivative of $\vec{H}$must be computed with respect to an inertial frame of reference [20]. Since the MOI matrix $\boldsymbol{J_b}$ remains constant in the body frame, the transport theorem can be used to find the derivative in an inertial frame [11]. This time derivative of angular momentum happens to be equal to the external moment $\vec{M}_{ext}$ acting on the body about its center of mass [17]. After dropping subscripts and applying the transport theorem $\dot{\vec{H}}$is given by

$$\dot{\vec{H}} = \begin{bmatrix} \dot{H}_1 \\ \dot{H}_2 \\ \dot{H}_3 \end{bmatrix} = J_b\dot{\vec{\omega}} + \vec{\omega}^{\times} J_b\vec{\omega} = \vec{M}_{ext} \tag{32}$$

which is equal to the applied external torques. Expanding Eq. (32) leads to Euler's rotational equations of motion which are three coupled, nonlinear, ordinary differential equations [17]. The kinematic Eq. (29) and kinetic Eq. (32) EOMs are the governing equations when attempting to control a spacecraft's orientation.

### 2.2.3 Attitude Control using Reaction Wheels

One of the most common ways to control spacecraft orientation is through the use of a RWA. Reaction wheels are able to provide very accurate pointing ability through exchanging the total momentum between the flywheel rotor or wheel and the spacecraft which does not change the total angular momentum of the spacecraft [21]. The RWA momentum can be described for three orthogonal reaction wheels from

$$\vec{h}_{rw} = D_{RWA}\vec{\psi}_x + D_{RWA}\vec{\psi}_y + D_{RWA}\vec{\psi}_z \tag{33}$$

where $D_{RWA}$ is the MOI of the motor armature and reaction wheel about the spin axis while $\vec{\psi}_i$ is the angular velocity of each wheel. This form of the equation assumes each wheel is aligned with an axis of the spacecraft body frame and only three wheels are used. In order to control the RWA, a PID controller can be implemented to compute the necessary torque required to reorient the spacecraft into a commanded orientation. The selected PID control law to be implemented is of the form

$$\vec{u}_{torque} = -(K_p\vec{q}_e + K_i \int \vec{q}_e dt + K_d\dot{\vec{q}}_e) \tag{34}$$

where $K_p$, $K_i$, and $K_d$ are the PID gains respectively. From this control vector $\vec{u}_{torque}$, the ADCS control card then divides the MOI of each wheel $D_{RWA}$ and computes the torque required by a change in RPM to be applied to each wheel to minimize the quaternion error. The commanded RPM is then converted to a pulse-width-modulated (PWM) signal for use on the BLDC RWA. A method of calculating these gains based on a desired response will be presented later in Chapter III.

## 2.3 Spacecraft Attitude Estimation

One of the more commonly used sensors for attitude determination is the magnetometer [11]. In order to estimate the orientation, the sensor information is compared to external magnetic field models. Two of the most common models are the International Geomagnetic Reference Field (IGRF) and the World Magnetic Model (WMM). The IGRF model is discussed here as this model is readily available in C code. However, due the memory and processor limitations on the current 6U AFIT ADCS the full model could not be installed during this research, but can easily be added in future versions.

### 2.3.1 International Geomagnetic Reference Field

The IGRF is calculated using spherical harmonics based on tilted-Earth-centered magnetic dipole parameters [22]. The parameters are maintained and updated every five years with data collected by the International Association of Geomagnetism and Aeronomy (IAGA). The magnetic field $\vec{B}$ can be found by taking the negative gradient of the scalar potential $V(r, \theta, \phi)$ which can be written as

$$V(r, \theta, \phi) = R_E \sum_{n=1}^{\infty} \sum_{m=0}^{n} \left( \frac{R_E}{r} \right)^{n+1} \left( g_n^m \cos m\phi + h_n^m \sin m\phi \right) P_n^m (\cos \theta) \tag{35}$$

where $R_E$ is defined as the Earth's equatorial radius, $r$ is the radius from the center of the Earth to the position of interest, $\theta$ the longitude, and $\phi$ is the co-latitude [23]. The $g_n^m$ and $h_n^m$ coefficients are the time dependent parameters as calculated by the IAGA. The last variable $P_n^m (\cos \theta)$ is scalar formed from a Legrendre function where $n$ and $m$ are the degree and order of the coefficients, respectively. From the scalar potential $V$, the components in terms of spherical coordinates can be calculated by [23]

$$B_r = -\frac{\partial V}{\partial r} \tag{36}$$

$$B_\phi = -\frac{1}{r}\frac{\partial V}{\partial \phi} \tag{37}$$

$$B_\theta = -\frac{1}{r\sin\phi}\frac{\partial V}{\partial \theta} \tag{38}$$

where $(r, \theta, \phi)$ are the geocentric spherical coordinates. The magnitude of the Earth's magnetic field $B$ can calculated from

$$B = \sqrt{B_r^2 + B_\phi^2 + B_\theta^2}. \tag{39}$$

The magnitude $B$ is the total intensity of the magnetic field. The overall strength of Earth's magnetic field is weakest at the magnetic equator and increases exponentially toward the magnetic poles as seen in Fig. 7. The magnetic field strength also decreases as the distance from the Earth increases proportionally by $\frac{1}{r^3}$ [22]. For this reason, magnetometers on a spacecraft are typically only used for attitude measurements for orbits below 6,000 kilometers [11]. It is important to note that the IGRF is in a constant state of change. These continuous variations are due to local variations of iron ore content in the mantel of the Earth [23], irregularities in the liquid outer core which produce the dynamo process of the Earth [9] and can even be affected by solar flares via the interplanetary magnetic field caused by the Sun [10]. The latest $B$ field intensity contour plot is shown below and is representative of the current IGRF model until it expires December 31, 2019. In Fig. 7, it interesting to note the area of least intensity over the South Atlantic, which is also near the magnetic equator. As discussed above, the $B$ field intensity in this area is lowest. This phenomena is known as the South Atlantic Anomaly and allows radiation from the Van Allen Radiation Belts to penetrate lower than normal which may be of concern for spacecraft in LEO.

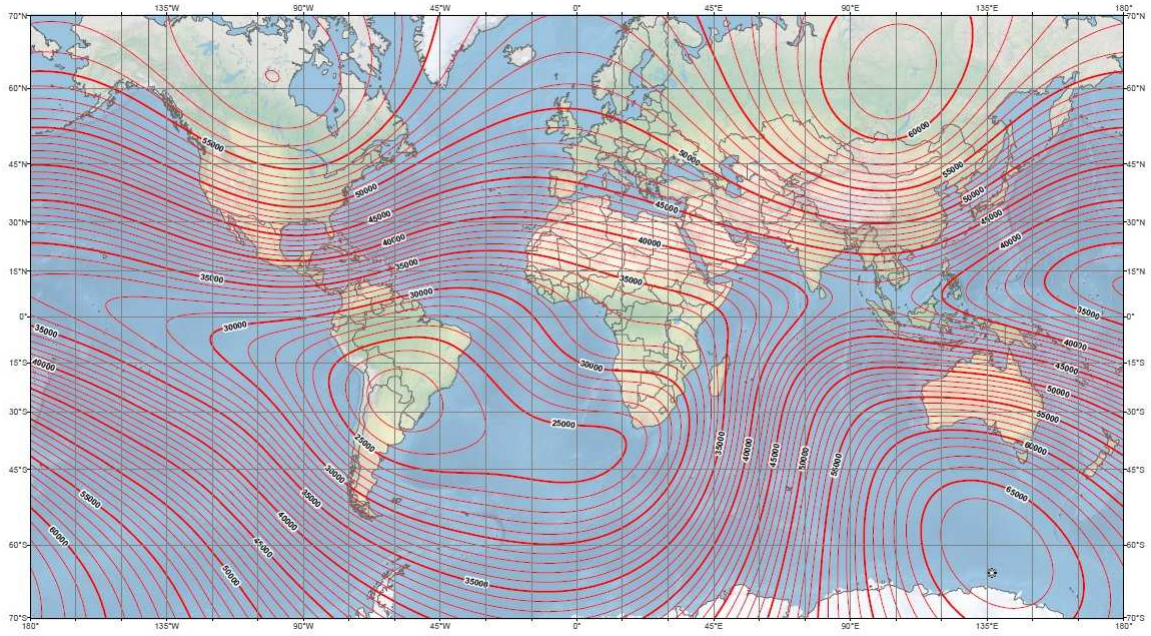

**Figure 7. 2015 IGRF Total Intensity Model at 600 km [5]**

In order to complete the IGRF coordinate frame system, a total of seven parameters are required. These parameters consist of three orthogonal components $(X, Y, Z)$, two field intensity components $(H, B)$, and two offset angles $(D, I)$ that relate true geographic north to magnetic north. The IGRF coordinate system is shown in Fig. 8., where $B$ is the total intensity, $H$ is the horizontal intensity, $D$ is the declination, and $I$ is the inclination. The declination $D$ is the angular difference between the magnetic north pole and true geographic north. Declination is positive east of true north and negative when west. The inclination parameter is the angle between the Earth's horizontal plane and the magnetic field lines which is positive in the down direction as depicted. The seven IGRF coordinates are calculated from Eqs. (41-47) [23].

$$X = H\cos(D) \tag{40}$$

$$Y = H\sin(D) \tag{41}$$

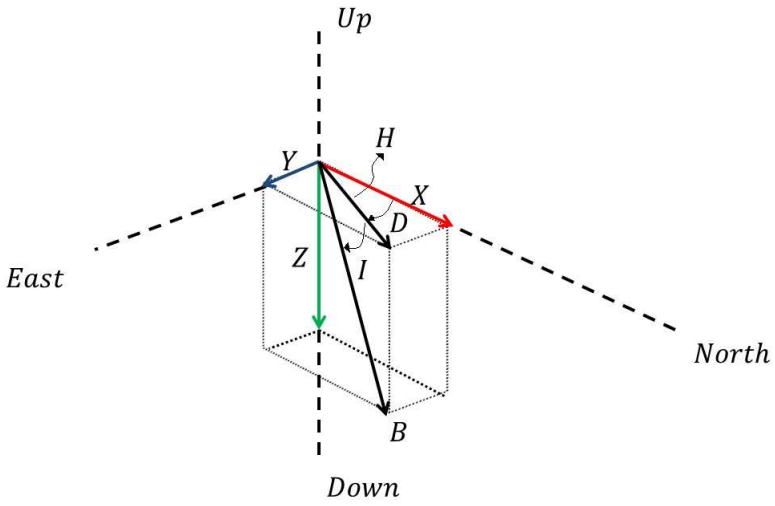


**Figure 8. The Seven Components of the IGRF Coordinate System**

$$Z = -B_r \tag{42}$$

$$H = \left(X^2 + Y^2\right)^{\frac{1}{2}} \tag{43}$$

$$B = \left(Z^2 + H^2\right)^{\frac{1}{2}} \tag{44}$$

$$D = \tan^{-1}\left(\frac{Y}{X}\right) \tag{45}$$

$$I = \tan^{-1}\left(\frac{Z}{H}\right) \tag{46}$$

As discussed earlier, the IRGF components are also typically transferred into yet another coordinate system for attitude determination. The IGRF parameters are

useful in the sense that they can be directly converted into or from the geographic latitude and longitude coordinate system with trigonometric functions [10]. This simple conversion is why many marine and aerospace navigation systems rely heavily on the accuracy of the IGRF model which is readily available in many formats [5].

### 2.3.2 Quaternion Estimation

Almost all quaternion estimation methods are originally based on a problem proposed by Grace Wahba in 1965 [24]. The goal is to find the rotation matrix $\boldsymbol{R}^{bi}$ that can accurately transform the sensor measurements $\vec{v}_{kb}$ from the spacecraft frame to an inertial frame $\vec{v}_{ki}$. For a satellite with $N$ sensor measurements, the loss function can be written as

$$J = \frac{1}{2}\sum_{k=1}^{N} w_k \left|\vec{v}_{kb} - \boldsymbol{R}^{bi}\vec{v}_{ki}\right|^2 \tag{47}$$

where $w_k$ is the sensor measurement weighting and $k$ is the counter for the $N$ sensors [11]. Many algorithms have been created to solve this cost function and have been studied extensively while many variations and methods exist [25]. The AFIT ADCS system currently utilizes the QUEST algorithm as it provides a computationally efficient method of solving the eigenvalue problem presented. This research will investigate and characterize just how accurate the quaternion estimate from QUEST is compared to an external truth measurement. Minimizing the cost function is identical to maximizing the gain function given from

$$g = \sum w_k \vec{v}_{kb}^{T} \boldsymbol{R}^{\boldsymbol{bi}} \vec{v}_{ki} \tag{48}$$

where $g$ is defined as the optimal eigenvalue $\lambda_{opt}$ [11]. Assuming the loss function $J$ is sufficiently small or zero presents a good approximation for calculation of the optimal

eigenvalue from

$$\lambda_{opt} = \sum w_k. \tag{49}$$

The current AFIT ADCS code only uses two sensors measurements from the Analog Devices IMU, the magnetometer and the accelerometer both with equal measurement weighting in QUEST. From this weighting scheme the Rodrigues parameters are then computed from

$$\boldsymbol{p} = \left[(\lambda_{opt} + \sigma)\mathbf{I_{3x3}} - S\right]^{-1} Z \tag{50}$$

where $\boldsymbol{S}$ and $\boldsymbol{Z}$ are sub-matrices that are made from normalized and weighted sensor measurements from the following equations.

$$\boldsymbol{F} = \sum_{k=1}^{N} w_k (v_{kb} v_{ki}^T) \tag{51}$$

where $v_{kb}$ and $v_{ki}$ are the vector measurements from the sensors. Next, $\boldsymbol{F}$ is used to obtain $\boldsymbol{S}$ by

$$\boldsymbol{S} = \boldsymbol{F} + \boldsymbol{F}^T \tag{52}$$

and $\boldsymbol{Z}$ is given from

$$\boldsymbol{Z} = \begin{bmatrix} F_{23} - F_{32} \\ F_{31} - F_{13} \\ F_{12} - F_{21} \end{bmatrix}. \tag{53}$$

The scalar variable $\sigma$ is the trace of $\boldsymbol{F}$. From the Rodrigues parameters the current quaternion is then calculated by

$$\bar{\mathbf{q}} = \frac{1}{\sqrt{1 + \mathbf{p^T p}}} \begin{bmatrix} \mathbf{p} \\ 1 \end{bmatrix} \tag{54}$$

which upon initialization of the system gives the current quaternion $[0, 0, 0, 1]^T$. This process is implemented on the AFIT ADCS controller card in approximately two hundred lines of C code. As Hall notes in [11], this approach does have a drawback in the fact that a singularity develops in the Rodrigues parameters when the rotation is at $\pi$ radians.

#### 2.3.2.1 System Noise

There are many sources of sensor noise that can affect the attitude estimation accuracy of the ADCS. Even if all external noise coupling could be eliminated from a circuit, a theoretical minimum noise level would still exist due to certain intrinsic or internal noise sources [26]. The most common source is thermal noise which is induced by thermal agitation and resistance of electrons in a circuit. Other sources exist through contact noise which is caused by imperfect connections between two conductors or shot noise which develops from manufacturing defects. The primary source of noise on the AFIT ADCS was determined by Tibbs [4] to be the proximity of the RWA to the IMU. Recent research conducted by the University of New Mexico with Sandia National Laboratories suggest that even the operating system (OS) can add unintentional noise into the system. The research shows that OS interference is the key limiter in many high performance systems [27]. Other research suggests that the timer interrupt rate and accuracy can add additional issues into the system [28]. For these reasons, an effort to minimize the number of OS interrupts on the AFIT ADCS will be implemented in the research herein.

### 2.3.3 Kalman Filtering

As more sensors and capabilities are added to the AFIT ADCS, more robust ways of collecting sensor data and managing sensor noise need to be implemented.

Past work at AFIT utilized a moving average filter to smooth the sensor data before performing QUEST [4]. However, there exist other options which may provide better results. One of the most versatile is the famous Kalman filter developed in the early 1960's by Rudolf E. Kalman. The Kalman filter estimates the state of a plant given a set of known inputs and a set of measurements [29]. The Kalman filter used in the predictor and corrector form is shown in Fig. 9 where $u(t)$ is a generic control input of

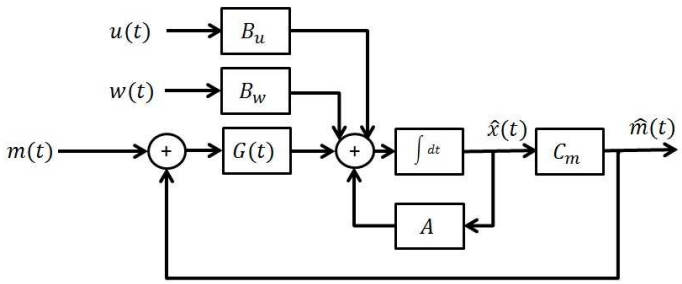


**Figure 9. Kalman Filter in Prediction/Correction Form**

the system and $m(t)$ is the measured output. The disturbance input or noise is $w(t)$, while $A$, $B_u$, $B_w$, $C_m$ and $G(t)$ represent the state matrix of the associated model. The estimated state of the system is defined by the variable $\hat{x}$. To incorporate a fully functioning Kalman filter on a spacecraft reference [6] estimates that approximately seven thousand lines of code are required. In many cases, the system model can be simplified and as Wiesel noted in [30] the Kalman filter becomes very tempting to use in the case where limited computational resources are available. As the AFIT ADCS uses discrete time to process all calculations a discrete-time Kalman filter could be implemented to smooth the sensor data. The background theory on the development and history of this filter is well documented in [31]. The discrete-time Kalman filter used in this research is given by

$$\hat{x}_{k+1}^{-} = Ax_k + \vec{w}_k \tag{55}$$

$$P_{k+1}^{-} = AP_kA^T + Q \tag{56}$$

where $\hat{x}_k$ is the sensor measurement and $\hat{x}_{k+1}^{-}$ is the previous sensor measurement estimate while $\vec{w}_k$ is the noise in the system. $P_{k+1}^{-}$ is the predicted estimate covariance and $A$ is the state transition model. $Q$ is the process or sensor noise inherent in the system. The Kalman gain is defined as

$$K_k = P_k^{-} H_k^T (H_k P_k^{-} H_k^T + R_k)^{-1} \tag{57}$$

where $H_k$ is the output transition matrix and $R_k$ is the measurement noise covariance matrix. The next step in the process is referred to as the measurement update or the innovation and is given by

$$\hat{x}_k = \hat{x}_k^{-} + K(\vec{z}_k - H_k \hat{x}_k^{-}) \tag{58}$$

$$P_k = (I - K_k H_k) P_k^{-} \tag{59}$$

where the $(\vec{z}_k - H_k \hat{x}_k^{-})$ term is the measurement noise residual and can be useful in monitoring the system by how much the filter is changing the measured value [31] from the real sensor output data collected. Although, this version of the Kalman filter is extremely simplified in this case; the mathematical process still provides efficient and powerful ways of smoothing and filtering data of single variables as detailed more in [30] with limited computational resources such as the current AFIT ADCS controller card.

## 2.4 Literature Review

This section begins by documenting related research from other universities and their efforts involving CubeSat testing and ends with a brief history of AFIT's CubeSat test bed. Much of the current small satellite research is focused around the implementation of a Helmholtz cage around an air bearing to utilize the onboard magnetometers and frictionless environment. Other systems like the larger satellite simulator at AFIT have builtin star fields for testing star trackers [4].

### 2.4.1 Rensselaer Polytechnic Institute

The Rensselaer Polytechnic Institute (RPI) in New York, has recently completed work that incorporated an ADCS utilizing COTS optical sensors to calculate the quaternion and validated the system with the PhaseSpace 3D motion capture system. RPI has developed a novel 6-degree-of-freedom (6-DOF) spacecraft simulator platform referred to as the Advanced Autonomous Multiple Spacecraft (ADAMUS) laboratory [32]. The ADAMUS spacecraft simulator includes a mass balancing system that provides counterbalancing, an integrated thrust vectoring system, and linear air bearings at the base to allow translation over an epoxy floor. The entire test platform is controlled through a ground station running real time application interface (RTAI) Linux and capturing data in real time through a series of IEEE 802.11 Wi-Fi networks capable of data acquisition at speeds up to 100 Hz. The RPI CubeSat test involving nano-optical vision chips can be seen in Fig. 10.

Although this testing was completed without active control the air bearing and mass balancing systems were in operation. The research incorporated the QUEST algorithm and programmed the spacecraft simulator to gather attitude data based on the unfiltered position of two light sources in the room at known locations. The test setup was then oriented through a series of test points by hand to compare the

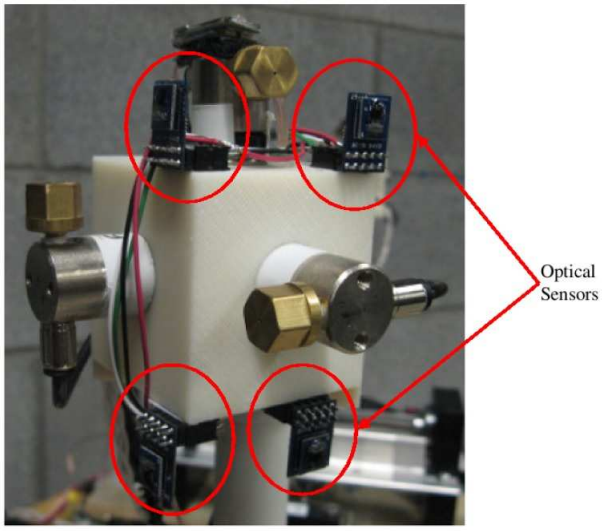


**Figure 10.**
Rensselaer Polytechnic Institute CubeSat ADS [32]

onboard quaternion value with the PhaseSpace system acting as the truth source. Testing results showed that the low-cost optical sensors could provide a mean error of $5.17^o$ and a max error of $24.59^o$ could be achieved using only four sensors [32]. The research was considered only as a proof of concept for future CubeSat research and notes that filtering of the data would significantly increase the accuracy from the sensors.

### 2.4.2 University of Surrey

The University of Surrey in the United Kingdom continues to be a state-of-the-art research institution providing academic advice and engineering consultation to over 39 different satellite launches [33]. The Surrey Space Center (SSC) at the University of Surrey has been pioneering small satellite research since 1979 and has made considerable advancements in control moment gyroscopes (CMG) for CubeSats and expandable sails for control and de-orbit [1]. The SSC research center offers numerous air bearing and kinetic motion capture systems. One of the more interesting air bearing test beds is known as the EAGLE, a granite table that allows for $x$- and

$y$-axis translation. The horizontal EAGLE air bearing table is shown in Fig. 11.

**Figure 11. University of Surrey Horizontal Air Bearing [1]**

The translation test bed allows for unique CubeSat testing opportunities that spherical air bearings cannot offer. A few examples of these unique tests include CubeSat proximity operations, propulsion system control testing, and a large open area for sail deployment during ADCS control testing. Along with the advanced ADCS capabilities and test platforms that the University of Surrey offers, they have made some significant gains in singularity avoidance with micro CMGs for CubeSats with the work of Prof. Lappas et al. [33].

### 2.4.3 Naval Postgraduate School

The Naval Postgraduate School (NPS) continues to remain in the forefront of CubeSat ADCS testing. The implementation of the first CubeSat auto mass balancing three-axis simulator named CubeTAS [34] and recent addition of a PhaseSpace motion capture system provides graduate students a unique opportunity to test and verify attitude determination algorithms and three-axis controllers. The NPS test platform with the PhaseSpace cameras can be seen in Fig. 12.

Notice in Fig. 12 that the motion capture cameras are extended away from the main frame of the Helmhotz cage. This is due to the fact that the PhaseSpace system requires a minimum capture volume to allow for accurate calibration and motion capture requirements. The NPS CubeTAS is equipped with flight-grade reaction wheels,

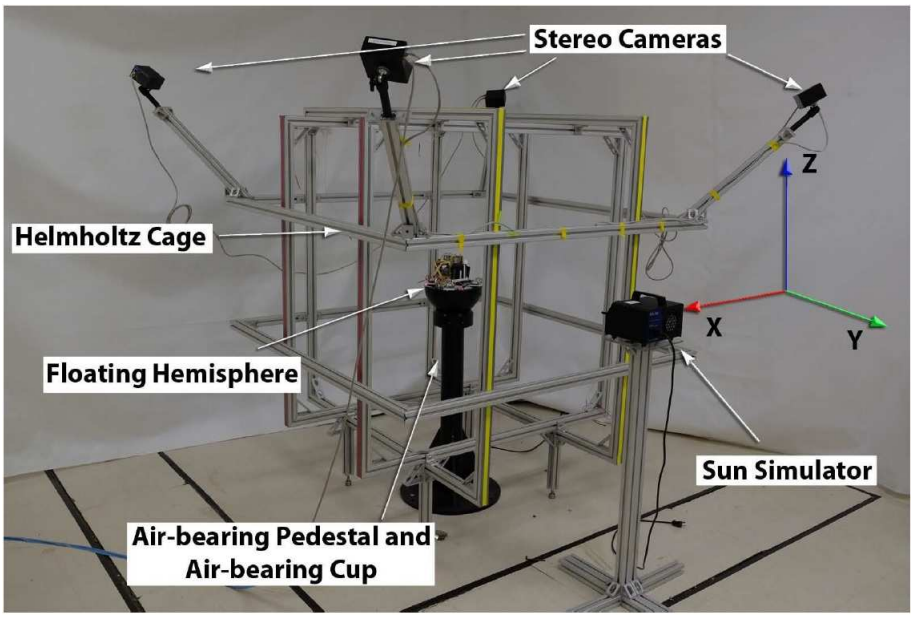


**Figure 12. Naval Postgraduate School CubeTAS Test Bed [2]**

custom torque coils, sun sensors, an IMU, and an onboard Wi-Fi that commands the ADCS test bed through MATLAB routines on a separate Linux-based computer. Furthermore, it should be noted that NPS students have provided AFIT with generous access to their PhaseSpace application program interface (API) toolbox which will help future development on the AFIT CubeSat test bed.

### 2.4.4 Stellenbosch University

The Stellenbosch University of South Africa has recently begun construction of their CubeSat ADCS test bed. A particular interesting approach to the affects of RWA interference on the magnetometer was completed by [35] in 2014. During the initial design of the ADCS the researchers at Stellenbosch performed magnetometer testing by applying Mu-metal, a material with a high magnetic permeability for shielding of the RWA. Results showed that the effects of shielding the motor were increased when the Mu-metal could be applied to all facets of the RWA shield both internally and externally. The RWA interference at low RPMs induced low frequency noise

into the system which couldn't be consistently filtered. The analysis and results documented in [35] confirm the results found recently at AFIT by [4] in which testing around 0 RPM produced the worst EMI. This result eventually led the researchers at Stellenbosch to an ADCS design that would utilize a deployable magnetometer as the affects of RWA interference could be minimized at a distance of approximately 12 cm.

### 2.4.5 University of Michigan

The University of Michigan has had multiple CubeSat programs successfully launched and currently operating on orbit. The Radio Aurora Explorer (RAX) is the first CubeSat spacecraft that was sponsored by the National Science Foundation to study space weather phenomena [36] while the GRIFEX satellite that was launched in early 2015 continues to provide telemetry to student groups at the university. The university offers two unique air bearing test facilities and high altitude balloon test support for CubeSat data links. The dynamically controllable Helmholtz cage was recently used to test a novel attitude-independent magnetometer calibration with time-varying bias [37]. This research is of interest to the author as it performed on orbit calibration without any prior knowledge of the altitude solely based on the IGRF model discussed earlier in the chapter. The biasing function was also able to remove magnetic variances onboard the spacecraft caused by other electronic subsystems which will be implemented on future university CubeSat launches after further testing.

### 2.4.6 Overview of CubeSat Research at AFIT

The development of the CubeSat test bed at AFIT began with the construction and characterization of the Helmholtz cage with the work performed by Brewer [9].

At the time AFIT was in collaboration with the University of Michigan and NPS who helped provide insight into construction and integration of the dynamic cage control with both MATLAB and Systems Tool Kit (STK) software packages. A National Instruments (NI) LABview graphical user interface (GUI) was implemented to control the solid state switches (controlling the polarity) of the power supplies for the Helmholtz cage.

The next research contributing to the test bed was through the work performed by Dannemyer [3] who developed a Simulink model to control the four-wheel ADCS shown in Fig. 13. Attempts were made to control the four-wheel ADCS version in

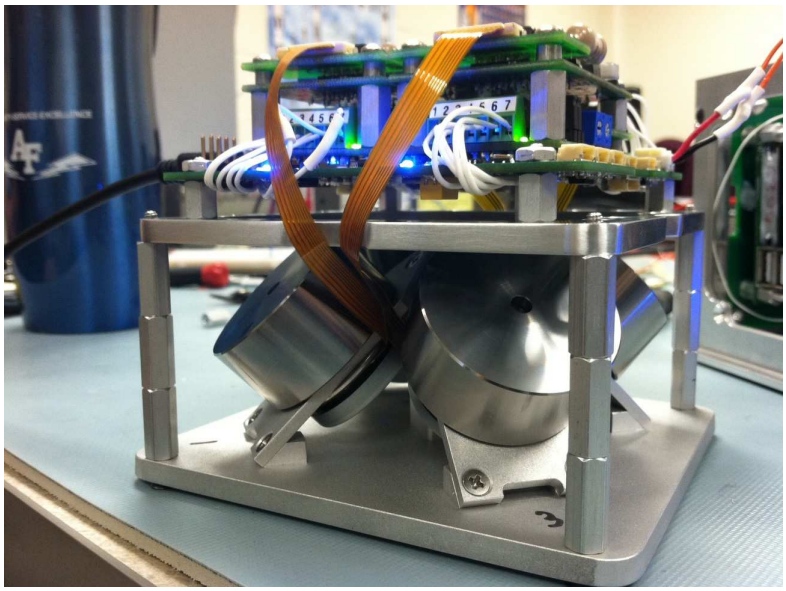

**Figure 13. AFIT 2013 Four Wheel Pyramid RWA [3]**

Fig. 13 using the Simulink conversion to C code compiler which was not completely compatible with the current ADCS controller board. Although these software issues did arise, code was compiled that allowed control of the AFIT ADCS test bed with a pointing errors approximately $\pm 20^o$ and attitude estimation accuracy $\pm 3^o$. Due to limitations in the software the ADCS control algorithm operated at only 1 Hz. Later, Lippert and Dicks were able to implement better task control of the ADCS algorithms

running at approximately 10 Hz.

More recently Tibbs was able to install magnetometer biasing that accounted for the RWA EMI. The code was still performing quaternion calculations, but the PID controller used required that the $z$-axis Euler angle be computed and filtered. After a thirty-seven second magnetometer biasing function the ADCS was capable of performing attitude estimation up to $\pm 0.1^o$ which improved control from $\pm 20^o$ to $\pm 0.07^o$ limited to a $\pm 25^o$ operational window in a 2000 mG magnetic field [4]. The ADCS testbed utilized a four-wheel RWA, however was limited to operating only three wheels at a time because of the motor driver daughter board used in the design. The CubeSat as used by Tibbs can be seen in Fig. 14. The CubeSat as configured

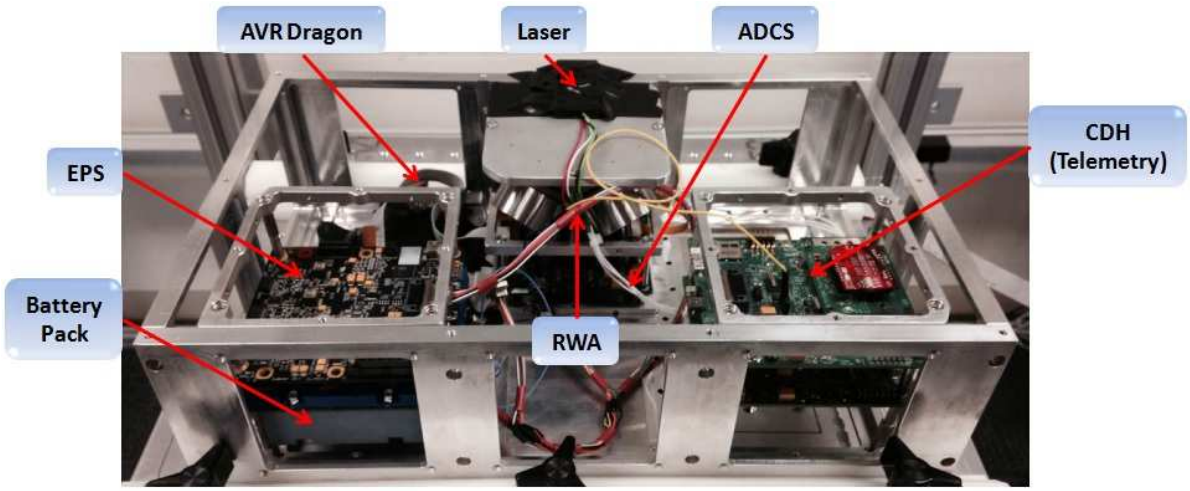


**Figure 14. AFIT 2015 FourWheel ADCS Test Bed [4]**

in Fig. 14 was then initially used for testing in AFIT's space vehicle design sequence during the summer of 2015. However, during the testing the control ribbon for one of the motors was damaged losing all functionality of the wheel. The first attempt to fix the ADCS test bed was made by plugging in the spare wheel of the four-wheel RWA. This attempt drastically changed the original magnetometer biasing and all control and estimation ability were lost on the ADCS test bed. A later attempt was made to replace the original wheel, but was averted after several issues arose. These issues are

summarized in the list below and have contributed to the author's main motivation for taking on this research.

- 6V Maxon BLDC motors were installed, however 8.4V was being applied by the ADCS controller card, during this process the correct 9V Maxon BLDC motors were ordered as 6V motors began to burn out and fail more frequently during high-speed testing
- Magnetometer bias was only valid in test conditions of [0, 2000, 0] mG
  - Eliminates possibility of dynamic Helmholtz cage settings for on orbit testing
  - Rolling average filter could be replaced with better filter to improve QUEST
  - The magnetometer biasing in C code lacked enough detail to be repeatable
- Speculation that the Hall sensor interrupt command which happened three times per revolution per wheel per second may be causing unknown real time operation system (RTOS) tasking and operator variable latency issues during operation
- The RTOS watchdog timer inhibited changing algorithm update rates
  - "*csvtime*" was a global variable and had hundreds of dependencies
  - The ATMEL ADCS C code project had numerous unused and repetitive library & header files which could be removed to increase $\mu$controller efficiency
- The four wheel RWA set is an older design. Using it with current CubeSat components made reassembly troublesome and time consuming, and in addition, it was known to fail vibration testing

At this point during the research there were also discussions at AFIT about the next generation AFIT ADCS card which would be based on the Beagle Bone Black $\mu$controller board. It seemed feasible to produce a rapidly prototyped 6U ADCS test bed within the time limitations of AFIT using many of the COTS components used in previous research to alleviate some of the design problems. The research problem became apparent that the issues listed above needed to be addressed and dealt with before the new AFIT ADCS card reached final production status. The development, configuration, and integration of the new hardware and software to tackle some of the issues listed in this section are documented in Chapter III.

## 2.5 Chapter Summary

Chapter II began by focusing on the background theory required in the design and implementation of a spacecraft ADCS. First, the chapter presents spacecraft attitude concepts to include an overview of the body frame, sensor frame, ECI, and ECEF frames. Next, the Euler angles were covered and a DCM was developed to perform rotations within different reference frames. Quaternions and Rodrigues parameters were also introduced and different methods of converting between them was presented. The kinetic and kinematic EOMs were given with the introduction of the quaternion error PID control law to be used. A section devoted to the IGRF and methods of attitude estimation was discussed leading up to the QUEST algorithm to obtain the current quaternion. Noise and filtering issues were addressed and concluded with the development of the discrete-time Kalman filter. The last section covered a literature review from other universities conducting CubeSat research and a brief history of the AFIT CubeSat ADCS test bed was explored. An overview of the hardware and software configuration along with the methodology for testing and truth source verification will be reviewed in Chapter III.

# III. Methodology

The purpose of Chapter III is to detail the development and modifications of the hardware and software used to test the AFIT 6U Cubesat ADCS. The first section covers the hardware setup of the test bed and CubeSat components used in this research. The second section covers the C code software development and modifications unique to this test. The third section details the MATLAB simulation model while the fourth section covers the PhaseSpace 3-D motion capture system to be used a truth source in the experiments. The last section covers the test methodology including the selection of test conditions and test points to be completed.

## 3.1 CubeSat Test Bed Overview

To experimentally verify attitude determination and control techniques that rely on magnetic field data a Helmholtz cage is required. In order to simulate the near frictionless environment on orbit an air bearing is employed. It is assumed that the reader understands the basic concepts of using a Helmholtz cage and air bearings for satellite testing in a terrestrial environment. The CubeSat test bed and ground station are located within the mechanical lab at AFIT. The hemi-spherical air bearing is centered within the Helmholtz cage in a region shown to produce a uniform magnetic field [9]. The ground station and test bed can be seen in Fig. 15. For more information concerning the Helmholtz cage or air bearing testing the reader can refer to Brewer [9], Dannemeyer [3], or Tibbs [4] which all cover the topics in greater detail. As shown in Fig. 15, the Helmholtz cage is powered by three separate power supplies that control the magnetic field strength inside the test area. An external truth magnetometer is fixed inside the cage on the test platform while the measurement is displayed on the milliGuass meter on the ground station used for tuning the magnetic field to the

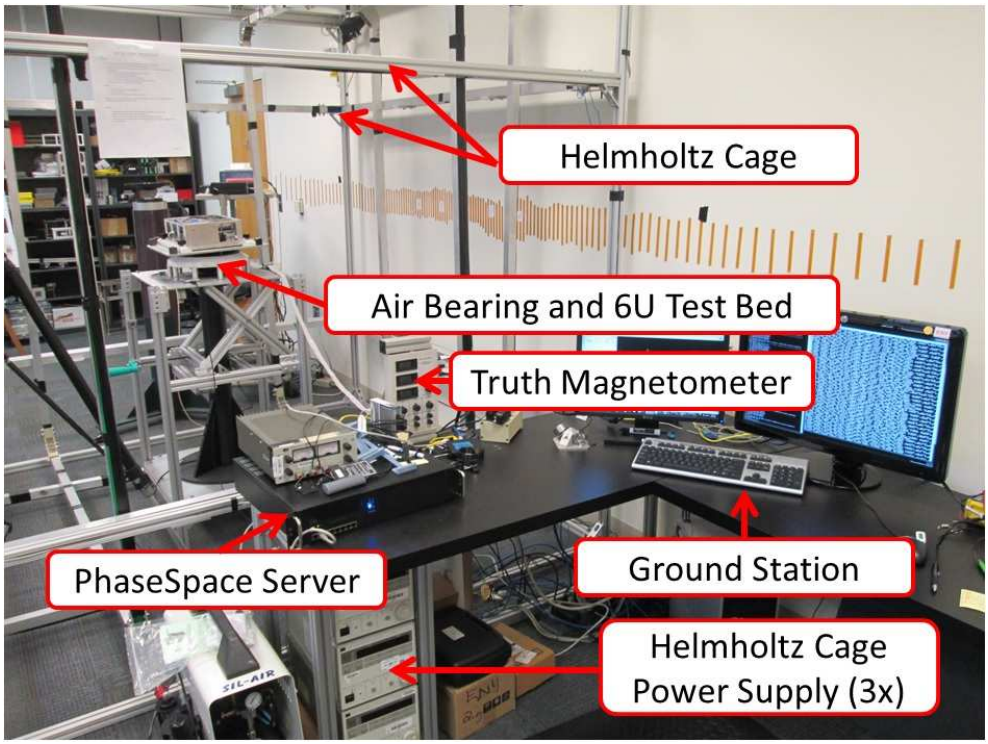


**Figure 15. 2016 AFIT CubeSat ADCS Test Bed Ground Station**

desired level. The ground station computer has the Atmel Studio suite to program the source code of the ADCS $\mu$controller and Tera-Term software which collects the telemetry from the test bed. The PhaseSpace Impulse X2E server runs proprietary data acquisition software and networks with the primary ground station computer through the PhaseSpace Owl server client.

### 3.1.1 6U CubeSat Hardware

The 6U CubeSat test bed hardware is loosely based on the current AFIT 6U CubeSat Interface Control Document (ICD). To perform testing the ADCS, EPS, and C&DH subsystems at minimum are required. This research only focuses on the ADCS so other systems and capabilities are not covered and can be found in the ICD [38]. The basic components of the 6U CubeSat at the beginning of this research can be seen in Fig. 16

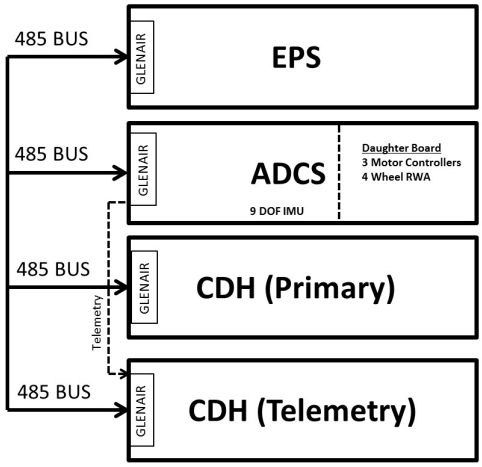


**Figure 16. 2015 ADCS Test Bed Overview**

Notice in Fig. 16 that there are two C&DH systems where one acts as the primary and the other only provides telemetry and ground station Wi-Fi capability. The 485 bus is a 15-wire harness that provides high-speed RS-485 serial data, battery power, and signals between the EPS, ADCS, C&DH, and PIB [38]. Although no payload is presently installed, one could simply be added to the 485 bus for future research. In order to accomplish this research and to mitigate the issues listed in Chapter II, the entire 6U test bed was disassembled and reconfigured. The primary goal was to move the RWA away from the IMU as far as possible to minimize EMI in the magnetometer. The secondary goal was to add a separate $\mu$controller to the RWA so the Hall sensor interrupt commands could be handled individually, freeing up computational resources on the ADCS board. For example, with a three-wheel RWA at speeds of 5,000 RPM on each motor the total number of interrupts per second would exceed 45,000. This isn't typically a problem for a $\mu$controller, but may lead to update latency issues in data storage [27]. A block diagram of this new test bed configuration can be seen in Fig. 17.

The current ADCS control board does have a secondary magnetometer on-board. This secondary magnetometer is the Honeywell HMC6343 sensor which provides $\pm 2^o$

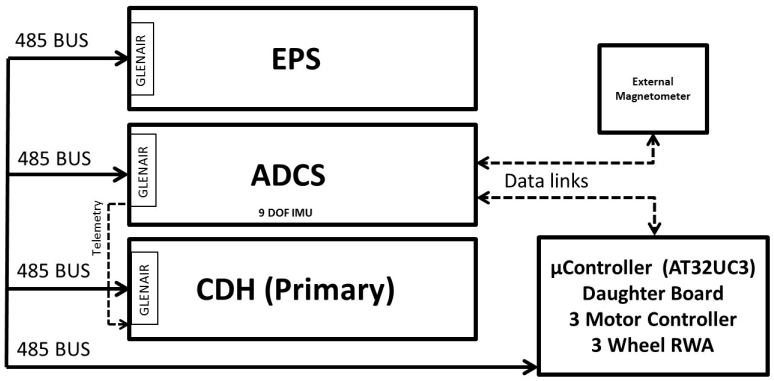


**Figure 17. 2016 Modified ADCS Test Bed**

of attitude accuracy [39]. However, in order to mitigate any stray EMI near the surface of the ADCS board an external magnetometer with better attitude accuracy was selected that could be displaced from the main electrical components. The chosen sensor was the HMC5883L 3-axis magnetometer on the Atmel ATAVRSBIN2 development board providing a attitude accuracy of $\pm 1^o$ and contains two other sensors; an accelerometer from Kionix (KXTF9) and a gyroscope from InvenSense (IMU-3000) [40] which could be used in future research. The $\mu$controller chosen to control the new three-wheel RWA was the same used on the current ADCS board. The 32-bit AVR flash $\mu$controller (AT32UC3) offers floating point units and was designed for various industrial and automotive control applications [40]. Using the same $\mu$controller greatly simplified the development to integration and test timeline as all that was needed was a second ADCS board. The second ADCS board required a data crossover cable to link the two controllers over the inter-integrated circuit (I2C) ports and additional software to properly handshake between the cards. Removing the RWA and motor-driver control daughter board away from the main ADCS allowed the C&DH and ADCS cards to be condensed into a 1U volume as shown in Fig. 18.

The reduction to only one C&DH card removed software/hardware support and real time control from the ground station GUI which wasn't considered a primary re-

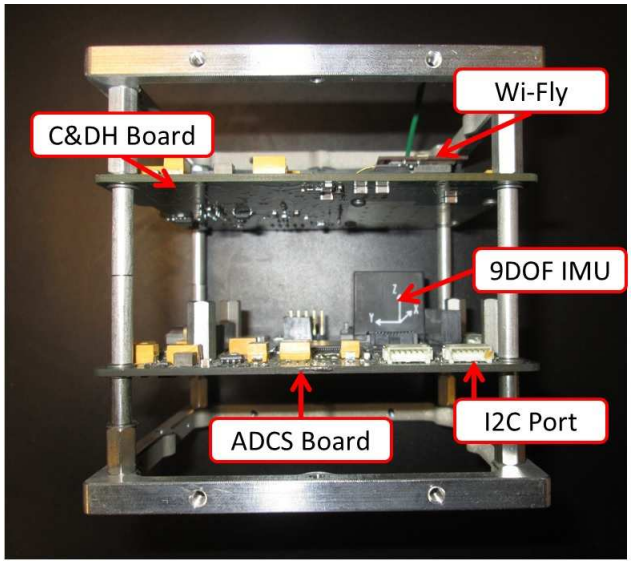


**Figure 18. 1U C&DH and ADCS Stack**

search requirement. A discussion on adding the ground station GUI back is discussed in Chapter V on the next generation AFIT ADCS card. Notice in Fig. 18 that the C&DH is on top of the ADCS, which is not the optimal setup as the Wi-Fly may cause additional EMI. However, it is more important during testing to be able to check the status LEDs on the C&DH as they were the only indication that telemetry was being sent and that Tera-Term could be activated to collect telemetry. The impacts of the placement of the Wi-Fly were not investigated and are left for future work in Chapter V. In addition to these changes a cross-hair laser pointer was installed as a visual reference for determining if nutation was removed by implementing the 3-axis control. Another feature added was a small switch that gives the operator a safer option to power the CubeSat test bed on and off. The next subsection will document the physical properties of the 6U CubeSat test bed for use in setting the gains of the PID control law.

### 3.1.2 Physical Properties

To account for the rearrangement of the IMU and the RWA, it was also necessary to redefine the sensor and spacecraft body frames. In order to simplify the coordinate system as much as possible to minimize additional rotation matrices in C code, the body frame was defined by the final placement of the IMU sensor frame shown earlier in Fig. 18. In an attempt to co-locate the CoR and CoM to exhibit 3-axis control, it was quickly realized the 6U test bed would become unstable on the air bearing if anything was added to the test bed unless it was placed at the CoR. The distance $d$ between the test bed platform and the surface of the air bearing male attachment along with the user defined coordinate system can be seen in Fig. 19.

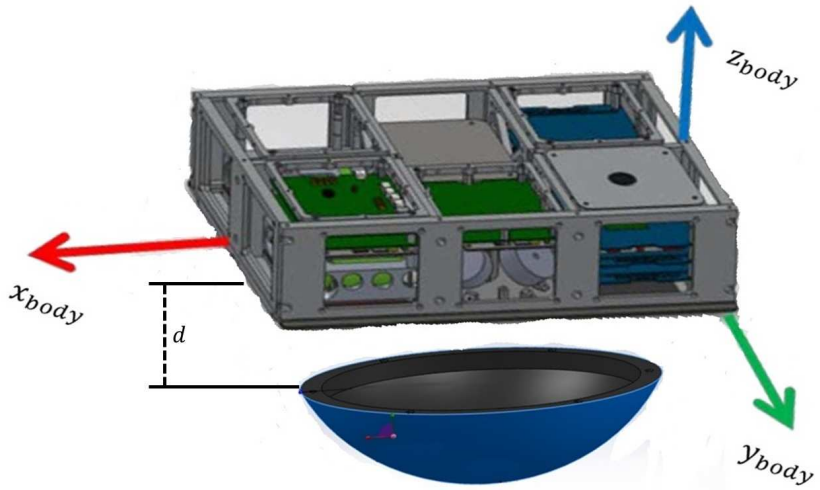


**Figure 19. 6U CubeSat Body Frame**

During initial setup, the distance $d$ was varied up to a distance of 27.0 mm away. It was found that stability could not be achieved on the air bearing with the loose wiring will low values of $d$. A final distance of approximately 24.0 mm was chosen in order to guarantee air bearing stability and continue testing, noting that the PhaseSpace components were not added until after this configuration was solidified. The final test bed with the CoR modification is shown in Fig. 20 where you can see the increase in $d$ was obtained by securing four longer bolts to the test platform. Although the

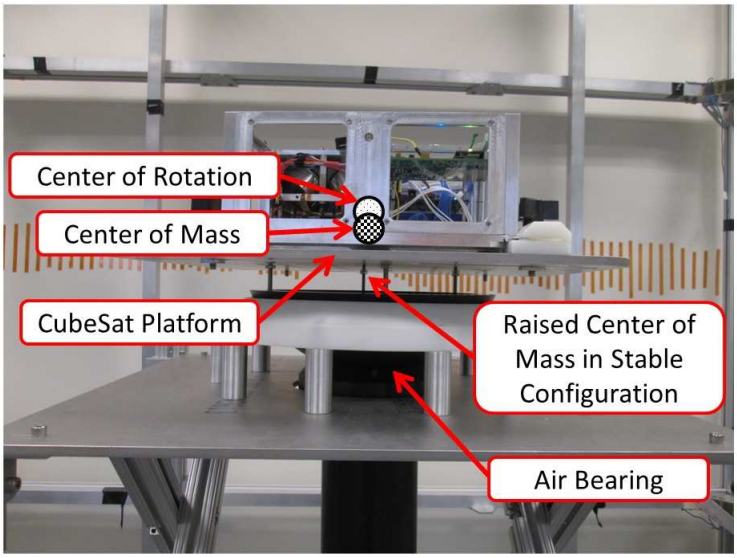


**Figure 20. Final Position of CoR in the ADCS Test Bed**

original air bearing had six bolt holes, it was discovered that if the extra two bolts were installed the CubeSat testbed would become position limited and could not be balanced correctly as the sliding attachment frame couldn't slide over the bolt-heads due to the predefined hole position between the platform and the air bearing. This issue could be easily solved by implementing socketed flat-head bolts. The moment that generated from the offset angle if there exists a difference in distance from the CoR and the CoM is given by

$$M_{d\neq 0} = mdg\sin\theta_{\text{offset}} \tag{60}$$

where $m$ is the mass of the CubeSat test bed, $g$ is the gravitational acceleration, and $\theta_{\text{offset}}$ is the angle between a vertical line and the line between the CoR and the CoM. Eq. (58) shows that even a small displacement between the CoR and CoM will generate a moment that can be many magnitudes higher than the torque limits that the RWA Maxon motors can achieve. An unloaded RWA motor can produce at maximum 8.71 mNm of torque [3], and after the wheel is added the loaded torque

is approximately 0.9 mNm. After taring the mass measurement device, the CubeSat test bed mass was found to 9.45 kg. For small angles, the moment caused by gravity is approximately 45.5 mNm per degree and cannot be controlled with the current BLDC motors on the ADCS test bed.

Next, the MOI of the CubeSat was obtained by placing the CubeSat test bed on the MOI measurement device shown in Fig. 21.

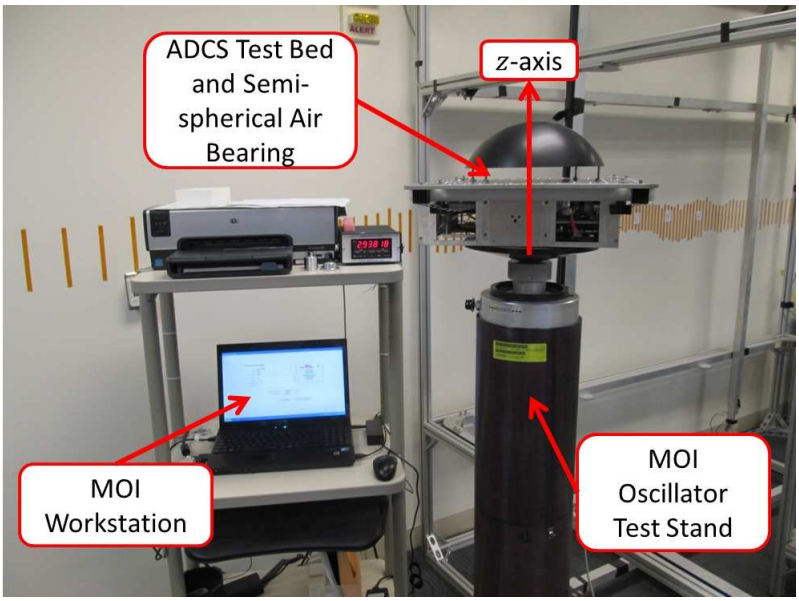


**Figure 21. ADCS Test Bed on Space Electronics XR 250 MOI Measurement Device**

The MOI around the $z$-axis was estimated using the MOI test stand measurement software. In order to gather the $x$- and $y$-axes measurements a mounting structure would have to be constructed to attach to the test bed directly through its CoR. Concerned that further measurements may damage the sensitive equipment on board the CubeSat, no further physical properties were collected and an estimate for the last two MOI would suffice. It was decided that the $x$- and $y$-axes could be no more than 120% and 130% of the $z$-axis based on a worst case MOI. These estimates come from the fact that the CubeSat is approximately 1U along the $z$-axis, 2U along the $x$-axis, and 3U along the $y$-axis while a 10% buffer for each 1U is added. Although

the three-axis control is functioning, the testing will only be done about the $z$-axis. The final values for the MOI of the CubeSat to be used in this research are shown in Table 1.

**Table 1. CubeSat ADCS Test Bed Moments of Inertia**

| Axis | Variable | Value (kg m$^2$) | Data Source |
|---|---|---|---|
| $z$ | $J_{zz}$ | 0.1853275 | Measured |
| $x$ | $J_{xx}$ | 0.2223930 | Estimate (120%) of $z$-axis |
| $y$ | $J_{yy}$ | 0.2409250 | Estimate (130%) of $z$-axis |

Once the MOI values are defined, the PID gain settings can be found and implemented into the software. The next subsection will cover how these gains are derived as discussed in Chapter II.

### 3.1.3 PID Controller Gain Settings

The PID control law was created to drive the difference between the quaternion and the quaternion error to zero. Wie presents a commonly used method in [17], which will be repeated here for completeness. In [17] a desired natural frequency $\omega_n$ and damping ratio $\zeta$, both equal to $\frac{\sqrt{2}}{2}$ are commonly used to find the PID gains through the following

$$K_p = J_i(\omega_n^2 + 2\zeta\omega_n/T) \tag{61}$$

$$K_i = J_i(\omega_n^2/T) \tag{62}$$

$$K_d = J_i(2\zeta\omega_n + 1/T) \tag{63}$$

where $T$ is the time constant of the integral control and is often selected to be $T \approx 10/\zeta\omega_n$ [17]. The PID controller gains are then calculated as listed in Table 2.

**Table 2. CubeSat ADCS PID Controller Gains**

| Axis | $K_p$ | $K_i$ | $K_d$ |
|---|---|---|---|
| $z$ | 0.1019 | 0.0046 | 0.2714 |
| $x$ | 0.1223 | 0.0056 | 0.3256 |
| $y$ | 0.1325 | 0.0060 | 0.3528 |

These values should give the CubeSat the desired response when commanded to change its attitude. It is interesting to note that Tibbs was able to determine values for the PID controller experimentally by adjusting each value and re-testing [4]; those values are quite similar to the values calculated above.

### 3.1.4 Rapid Prototype ADCS

For this research, a second rapid prototype 6U CubeSat ADCS was constructed using 3D printed parts for the frame. This secondary ADCS was used to test and troubleshoot the RWA cross link communication issues and to test sensors before integration on the primary ADCS and is shown in Fig. 22 where you can see the

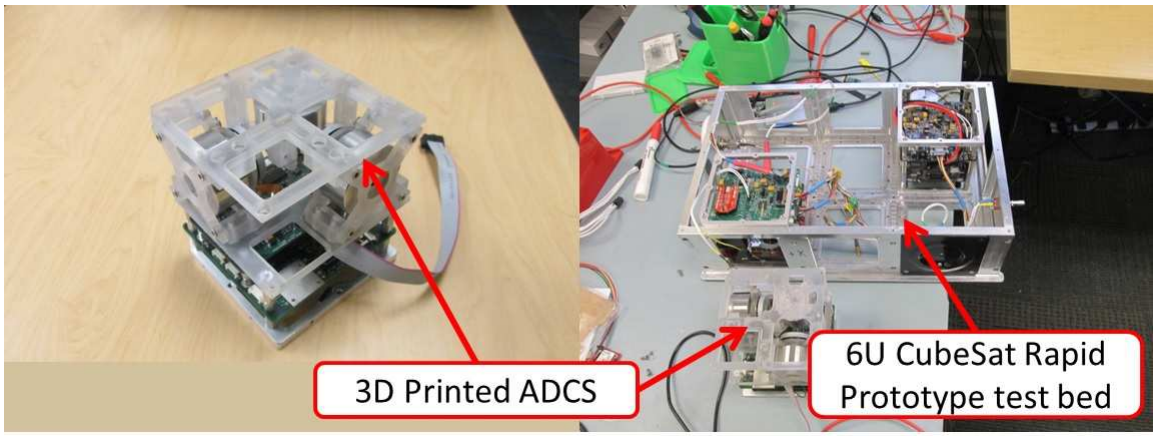


**Figure 22. AFIT 6U CubeSat Rapid Prototype Test Bed**

secondary ADCS is removed from the rapid prototyped 6U CubeSat. Many of the

systems in the prototype are not securely fixed as they are constantly being repaired, removed, calibrated, and tested. The rapid prototype workstation was an idea by Lippert and has led to the development of many novel CubeSat experiments and ground station developments. Many of the issues that developed on the primary CubeSat were overcome by having access to the prototype ADCS throughout the research.

## 3.2 Software Overview

A great software engineer once said *"The first 90 percent of the code accounts for the first 90 percent of the development time while the remaining 10 percent of the code accounts for the other 90 percent of the development time."* This section offers some insight into the C code currently used on the 6U ADCS test bed. The editor used for this research was the Atmel Studio version 6.2 which includes many of the required header files for the AVR $\mu$controllers used on the CubeSat. At the beginning of this research, the latest version of the ADCS project was checked out of AFIT's file sharing network. Many of the subroutines and other subsystems (mainly C&DH watchdog timers) were modified and customized to work properly solely for the ADCS test bed. The second subsection highlights the estimation and control algorithms, while the last section covers the MATLAB model used in this research.

### 3.2.1 6U CubeSat Software

To be utilized properly, any coding project involving physical hardware requires that each pinout, wire and sensor contact be known, installed, located, numbered and called within the software correctly. This was evident the first time the reconfigured 6U CubeSat was programmed. For these reasons it is important to know the architecture of the software. A diagram of how the 6U ADCS software is programmed

can be seen in Fig. 23. The code block with a "#" denotes the primary section

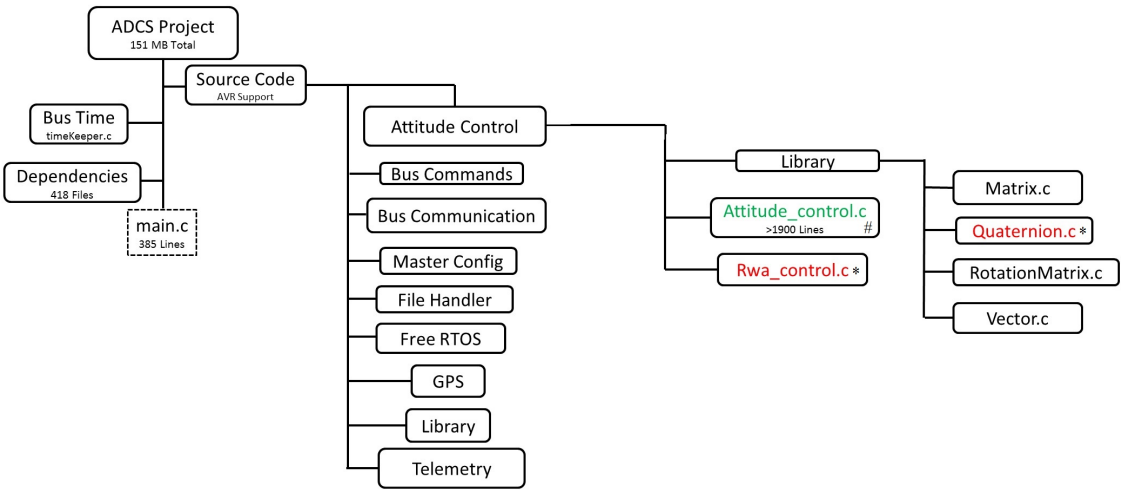


**Figure 23. Overview of ADCS Test Bed File Structure**

of the ADCS working directory. The block with a "∗" represents code that had to be reprogrammed to accommodate the replacement of the RWA and communication cross link. Notice that the "Dependencies" block is in the main ADCS structure, these are common header files that many of the AVR line of $\mu$controllers rely upon. Each and every sensor used must also have its related header and other dependent files such as *vector.c* or *math.c* which are common dependents. Much care must be taken while developing any future ADCS board on another $\mu$controller as these libraries are specific to the AVR family and may not work on future versions. The author estimates that there are over one hundred thousand lines of code compiled to the ADCS board with many functions being unnecessarily repeated multiple times. More discussion on this topic will be conveyed in Chapter V.

### 3.2.2 ADCS Algorithm

The ADCS algorithm includes both the control and estimation task running as one program at 10 Hz. To separate into different tasks, it would require replacement of the primary clock variable "*csv_time*" as it was used extensively throughout the entire

project folder with many hidden dependencies. Many solutions exist to solve this timing dependency problem, but were not implemented for the research presented. The main ADCS test bed estimation and control algorithm is shown in Fig. 24. Notice from Fig. 24 that the sensor inputs are gathered and stored on the primary

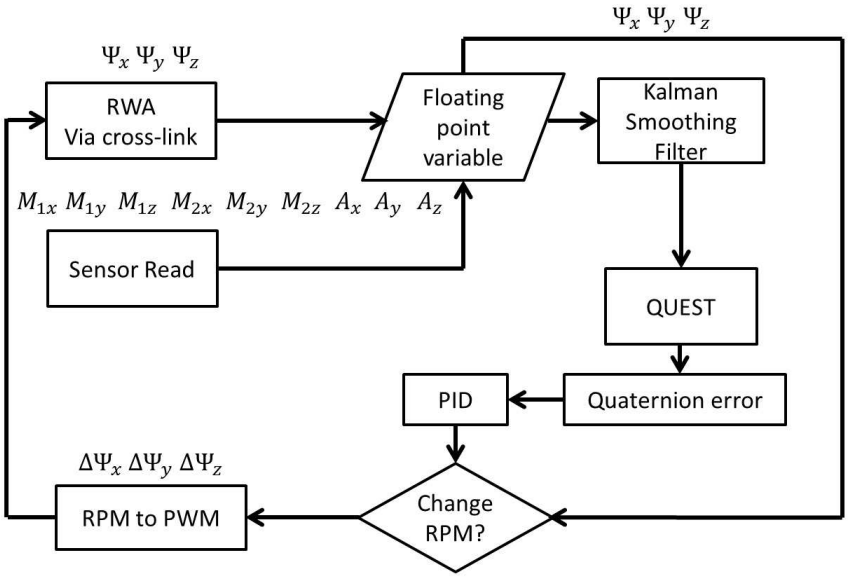


**Figure 24. ADCS Test Bed Estimation and Control Algorithm**

ADCS as floating point variables. Also note that the RWA speed variables bypass the Kalman filter block as the filter is currently only programmed on the primary ADCS $\mu$controller. $\Psi_x$, $\Psi_y$, and $\Psi_z$ are the current RWA RPM values sent from the secondary $\mu$controller via the cross link, where $M_{1x}$, $M_{1y}$, $M_{1z}$, $A_x$, $A_y$ and $A_z$ are the magnetometer and accelerometer values from the primary IMU respectively. The variables $M_{2x}$, $M_{2y}$, and $M_{2z}$ are from the additional external magnetometer. All sensor data is stored as a floating point variable. From there, the Kalman filter can be used to filter the data, if needed. Next, the $M_i$ and $A_i$ variables are sent through QUEST to obtain the current quaternion which is the last line of QUEST. After the current quaternion is updated, the quaternion error is then computed and fed into the PID controller. The PID control vector $\vec{u}$ from Eq. (35) is used to determine

how much the wheel speed must increase or decrease to produce a torque needed to drive the error to zero. This desired RPM is then sent via the cross link where the secondary $\mu$controller converts the desired RPM through a duty cycle conversion which calculates the new PWM command to be delivered to the motors.

### 3.2.3 MATLAB Simulation Model

Creating a working mathematical model of the 6U CubeSat ADCS is important as it can help expose design and process issues early in the development of a spacecraft. For this reason, this research utilized a MATLAB model to compare data with the experimental setup of the ADCS test bed. The model used was strictly a controller simulator as no estimation data will be used. It is primarily used to compare expected wheel speeds, control law settings, accelerations, and quaternion values. Simulations do have some drawbacks as the physical nature of the real system adds many unknown unknowns to account for. For example the cross products of inertia of the CubeSat are unknown and will affect the amount of cross coupling during a maneuver. Other aspects such as air drag are not currently taken into account in the simulation. The difference from the CoM to the CoR using Eq. (58) is incorporated, but has some uncertainty as the CoM of the CubeSat changes as the wires are not secured as the ADCS test bed is constantly being fixed. Next, the truth external truth source will be discussed.

## 3.3 PhaseSpace 3D Motion Capture System

Comparing the 6U ADCS attitude estimate to an external truth source is an excellent way to investigate how well the system is performing. To do this, a PhaseSpace Impulse X2E motion capture system is employed. Motion capture systems are a very accurate method of recording in real time the displacement and movement of a target

object within the test environment. The PhaseSpace motion capture device is an active system that uses tracker LEDs to individually blink at predefined frequencies. Four cameras each with two high-speed, high-resolution linear charge-coupled devices (CCD) use the identity of the tracker to triangulate the position of the object within a calibrated test environment. The system can either be used as a point tracker or a rigid-body tracker. Point trackers are typically used in human gait analysis. The rigid-body tracking feature is useful in this research as it can be used to generate a quaternion estimate from the orientation of the CubeSat during testing. The next few subsections will detail the hardware and software of the PhaseSpace Impulse X2E system.

### 3.3.1 PhaseSpace Hardware Setup

The PhaseSpace cameras are attached to the Helmholtz cage while the supporting power and data cables are secured within the frame. The computer that controls the cameras and processes the data is the PhaseSpace Owl server shown in Fig. 15 at the end of Chapter II. Much of the programming on the server is unknown as it is a proprietary COTS system. The server is networked to the main ADCS ground station computer. Fig. 25 shows the attachment location of one of the PhaseSpace camera systems.

In order for the system to track an object, a minimum of two cameras must have the line of sight to the LEDs on the target. Also, to use the system for rigid body tracking a minimum of three LEDs must remain in view during testing. To minimize the body blockage from the target itself and increase the overall line of sight eight LEDs were attached to the CubeSat platform. 3D printed holding blocks where made and bolted to the platform to secure the LEDs on the test bed.

The LED and the support device bolted to the CubeSat platform can be seen in

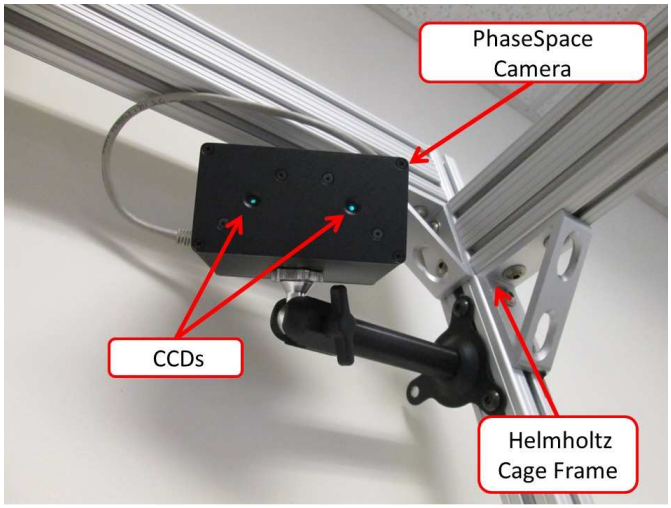


**Figure 25. PhaseSpace Camera Attached to Helmholtz Cage**

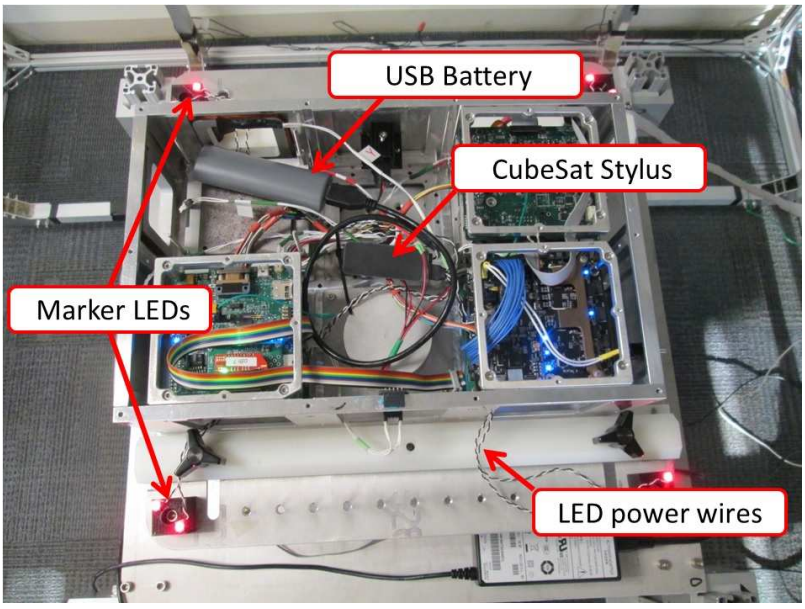


**Figure 26. PhaseSpace LED Placement on ADCS Test Bed**

Fig. 26. Notice that the wires and control device are not secured to the test bed. The control device is the CubeSat stylus which provides the LED drivers and links with the Owl sever for operation. The control device does contain a small battery which was determined to have an unacceptable discharge time and a COTS USB lithium ion rechargeable battery was incorporated and can also be seen in Fig. 26.

### 3.3.2 PhaseSpace Software Overview

The primary interface with the PhaseSpace system is through a GUI called Master Client which networks with the Owl server to collect and record LED position data. Once the system hardware is installed, the system requires an initial calibration with the wand. The calibration wand contains eight LEDs and is a known rigid-body on the Owl server system. The user must begin the calibration with the wand approximately in the center of the test area which is approximately the top of the air bearing. After initializing the calibration the wand must be moved throughout the field of view of all the cameras. Once all the volume bins in the test area have been filled by each camera the calibration settings are saved and another calibration isn't required unless the cameras are moved from the original locations. The test area after calibration with the software is now ready to collect motion data, the camera view cones are shown in Fig. 27.

Notice in Fig. 27 that the entire volume of the Helmholtz cage isn't totally covered. This coverage area is limited to the view area of each camera and should be noted for future use if those areas are required for test. The next step is to define the orientation of the camera view coordinate system and align it with the desired body frame so that the quaternions during testing will match. The alignment process is typically done after calibration, but can be performed anytime even after tracker data is collected [41].

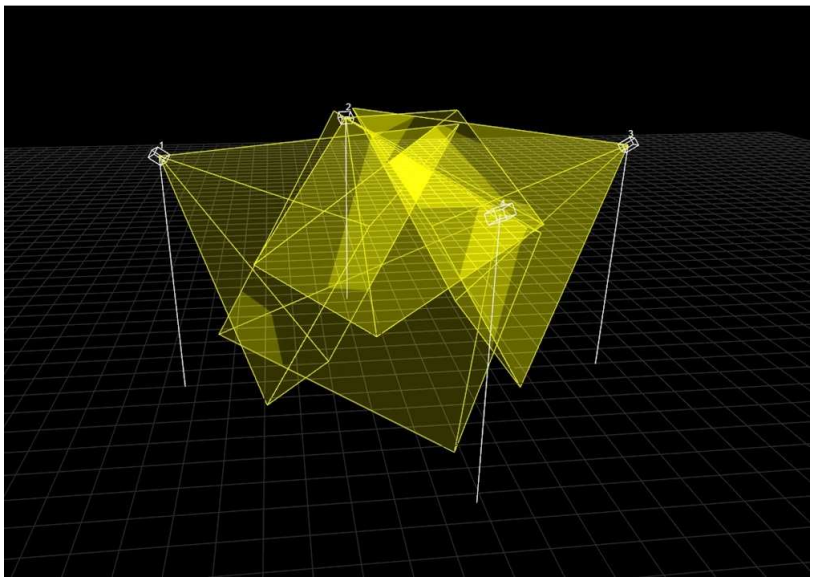

**Figure 27. PhaseSpace Camera Coverage Cones**

#### 3.3.2.1 Rigid-Body Configuration

Once the test bed is completed and the CubeSat stylus is turned on, a rigid-body configuration must be defined in order to estimate quaternions. The markers of the CubeSat test bed can be seen in Fig. 28. Notice in Fig. 28 that all eight markers are present with a numbering scheme from zero to seven. If some markers are not present, it's typically due to the power settings on the Master Client homepage which allows the LED power to be increased or decreased. The process of applying a rigid-body frame to the markerIDs in PhaseSpace is done by highlighting all the active markers and by right clicking the viewer window applying a rigid-body frame to the current markers. This process is shown in Fig. 29. The left side of Fig. 29 shows the rigid body editor where the coordinate frame of the rigid-body are edited to match the 6U CubeSat ADCS test bed.

To ensure the angles are defined properly in the software the inclination of the CubeSat test bed platform can be measured using an inclinometer. This process can be seen in Fig. 30.

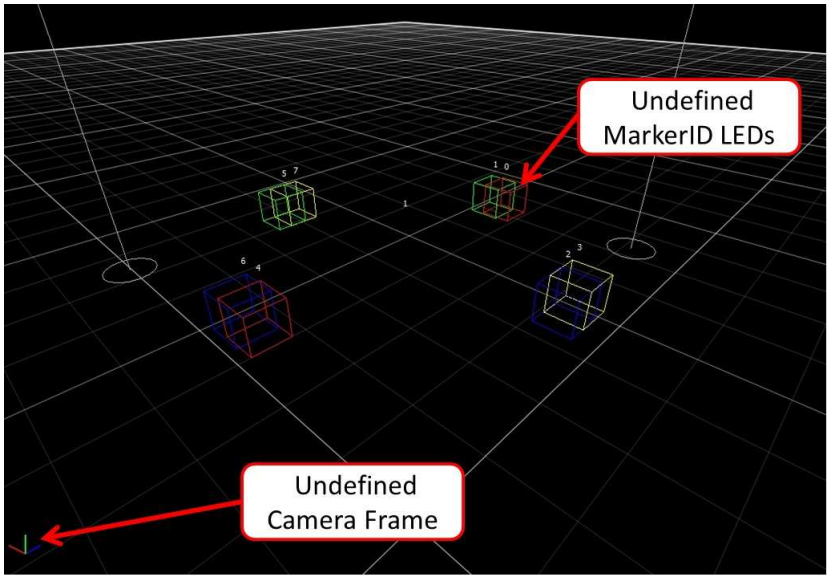


**Figure 28. Undefined Camera Frame and MarkerIDs in MasterClient**

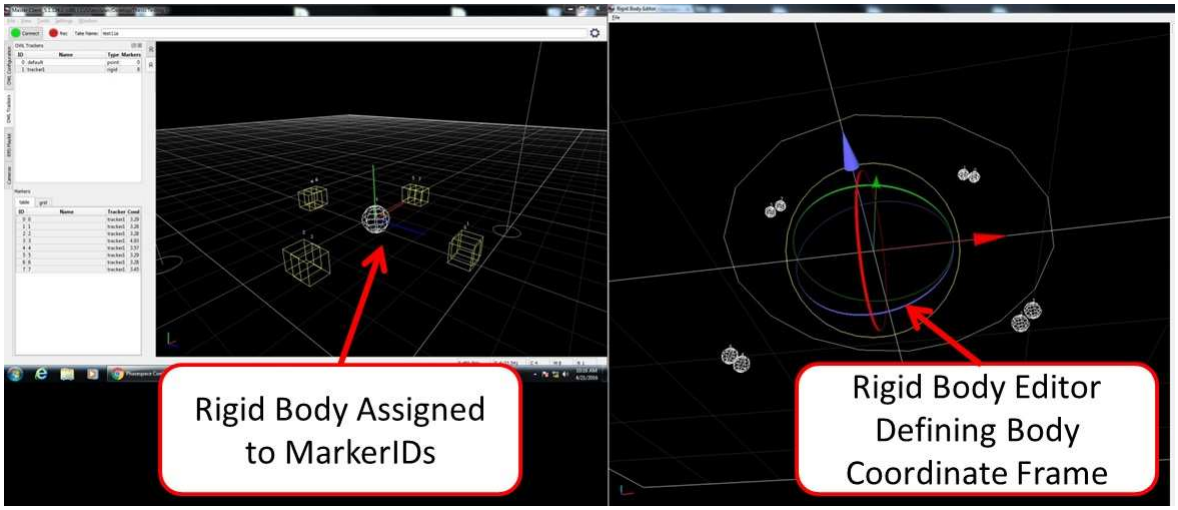


**Figure 29. Defining PhaseSpace Rigid-Body Coordinate Frame**

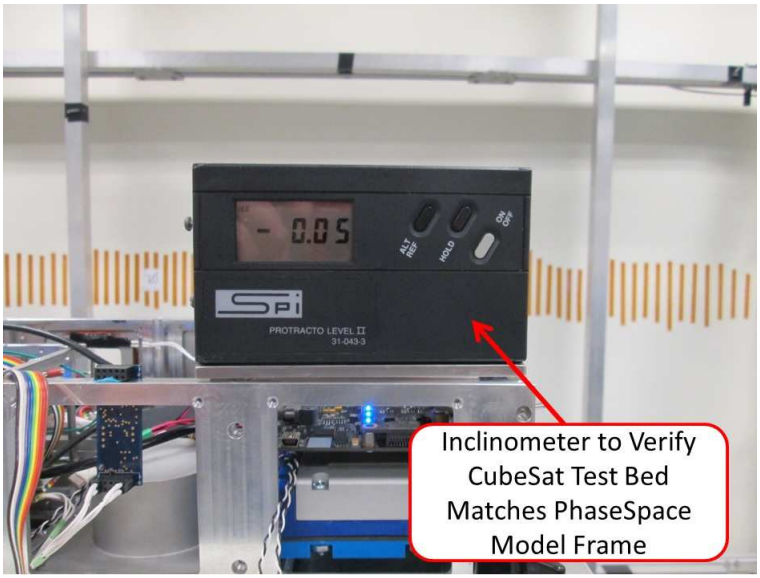


**Figure 30. Matching ADCS Test Bed to PhaseSpace Model**

Fig. 30 shows the $y$-axis to be approximately -0.05$^o$ off level which is within the tolerance of $\pm 0.7^o$ for the device. The $x$-axis was also within this tolerance and assumed to be negligible in relation to the rigid body defined in the software.

#### 3.3.2.2 Data Post Processing

After a test is conducted and data recorded, the file is saved as a Rapidfire Database file (RPD). To get the quaternion out of the RPD file, it can be post processed using a program written in C++ called an Application Program Interface (API). The API must be run from a command window and given the interet protocol (IP) address of the Owl Server. In the Master Client GUI, the RPD file must be loaded and replayed defined as rigid body. It was shown that if the quaternion is displayed directly to the screen the post processing time is approximately fifteen times the length of the test data collected. For this reason the API used for the research has the screen output suppressed so that the quaternion and the marker time are stored directly to a comma separated value (CSV) file.

## 3.4 Data Collection and Test Planning Methods

This section documents the methodology and procedures used to the test the performance of the 6U ADCS test bed. It begins with a subsection introducing the data collection process from the telemetry on the 6U CubeSat and the data to be post processed from the PhaseSpace system. Next, the magnetic field strength settings for the Helmholtz cage will be discussed. The following two subsections will then cover the two types of testing to be employed, static tests and dynamic testing. The fifth subsection overviews the methods used to conduct wheel speed control authority of the RWA. The sixth subsection covers methods used to estimate the CubeSat body rate by using quaternions. The last two subsections describe how the CubeSat will be tested for a singularity in QUEST and the error metrics that will be used in this research.

### 3.4.1 Data Collection

Data collection is crucial for experimental testing and performance analysis. After the 6U CubeSat test article is complete and all systems are installed, no future physical changes will be made to the CubeSat. This is a process used in the test community called freezing the system design which helps keep performance metrics and data collection processes repeatable in future testing [42]. There are certain limitations however; the battery for the PhaseSpace system will need recharging and the wire may move somewhat during each test. To minimize the effects of these items the wire harness and battery will be left in approximately the same position for the final balancing of the CubeSat on the air bearing. From this point forward, only the ADCS C code will change. The data to be post processed from the PhaseSpace system is somewhat limited currently at AFIT due to the time the system arrived and the amount of troubleshooting required to get the system operational. Currently, the

API used to post process data only includes the following data points list in Table 3.

**Table 3. PhaseSpace Data Collection**

| Parameter | Description | Units | C++ Code Variable |
|---|---|---|---|
| Marker Number | Time of Data Point | Positive Integer | MarkerID Counter |
| Position $x$ | Position in Camera Frame | mm | pose(1) |
| Position $y$ | ” | ” | pose(2) |
| Position $z$ | ” | ” | pose(3) |
| $q_4$ | Quaternion | none | pose(4) |
| $q_1$ | ” | ” | pose(5) |
| $q_2$ | ” | ” | pose(6) |
| $q_3$ | ” | ” | pose(7) |

As shown in Table 3, the markerID counter will be used to time stamp the data. This is obviously less than ideal for data collection, but due to compiler issues with the API on the CubeSat ground station it wasn't noticed until after testing data was recorded. Since the speed of the operating system can be defined by the user, the marker data can be simply converted into a time stamp. The camera detection and post processing update rates were both conducted at 480 Hz. Each data point can then be moved back into the time domain using

$$t_{sec} = MarkerID\frac{1}{480\text{Hz}}. \tag{64}$$

To collect the data from the 6U ADCS testbed, an open source, free, software implemented, and terminal emulator program called Tera Term is used. Term Term connects to the ADCS via the Wi-Fly card through a default IP address connection and can both display the data to the ground station and log it into a CSV file in real time. The telemetry send rate is currently set to the estimation and control algorithms rate of 10 Hz. The following variables in order to be collected from the 6U ADCS during testing are listed in Table 4.

**Table 4. Primary 6U CubeSat ADCS Data Collection Set**

| Parameter | Description | Units | C code Variable |
|---|---|---|---|
| Clock time | $\mu$controller time | sec | csv_time |
| $q_1$ | Current Quaternion | none | quaternion_current.x |
| $q_2$ | ” | ” | quaternion_current.y |
| $q_3$ | ” | ” | quaternion_current.z |
| $q_4$ | ” | ” | quaternion_current.w |
| $M_{1x}$ | Rolling Average IMU Mag | mG | MX |
| $M_{1y}$ | ” | ” | MY |
| $M_{1z}$ | ” | ” | MZ |
| $KM_{1x}$ | Kalman Filtered IMU Mag | mG | K_MX |
| $KM_{1y}$ | ” | ” | K_MY |
| $KM_{1z}$ | ” | ” | K_MZ |
| $M_{1xraw}$ | Raw Primary IMU Mag | mG | mxx |
| $M_{1yraw}$ | ” | ” | myy |
| $M_{1zraw}$ | ” | ” | mzz |
| $M_{2x}$ | Rolling Average External Mag | mG | EXT_MX |
| $M_{2y}$ | ” | ” | EXT_MY |
| $M_{2z}$ | ” | ” | EXT_MZ |

In order to conduct more analysis on the performance of the ADCS the additional variables in Table 5 will also be collected via telemetry from the ADCS test bed.

**Table 5. Secondary 6U CubeSat ADCS Data Collection**

| Parameter | Description | Units | C code Variable |
|---|---|---|---|
| $q_{e1}$ | Quaternion Error | none | quaternion_error.x |
| $q_{e2}$ | ” | ” | quaternion_error.y |
| $q_{e3}$ | ” | ” | quaternion_error.z |
| $q_{e4}$ | ” | ” | quaternion_error.w |
| $\omega_{x-est}$ | Rate Estimate from Quaternion | rad/sec | pp |
| $\omega_{y-est}$ | ” | ” | qq |
| $\omega_{z-est}$ | ” | ” | rr |
| $\omega_x$ | Rate from Gyro | rad/sec | omega.x |
| $\omega_y$ | ” | ” | omega.y |
| $\omega_z$ | ” | ” | omega.z |
| $t_x$ | Control Torque from PID Law | mNm | torque.x |
| $t_y$ | ” | ” | torque.y |
| $t_z$ | ” | ” | torque.z |
| $\dot{\Psi}_x$ | Angular Velocity Rate of Change | rad/sec | psi_dot[0] |
| $\dot{\Psi}_y$ | ” | ” | psi_dot[1] |
| $\dot{\Psi}_z$ | ” | ” | psi_dot[2] |
| $rpm_{cx}$ | Current RPM Command | RPM | tru_commanded_rpm |
| $rpm_{cy}$ | ” | ” | tru_commanded_rpm2 |
| $rpm_{cz}$ | ” | ” | tru_commanded_rpm3 |
| $rpm_x$ | Tachometer Reading | RPM | adcs_mtr1_tacho |
| $rpm_y$ | ” | ” | adcs_mtr2_tacho |
| $rpm_z$ | ” | ” | adcs_mtr3_tacho |
| $p_1$ | Rodrigues Parameter | none | p[0] |
| $p_2$ | ” | ” | p[1] |
| $p_3$ | ” | ” | p[2] |
| $l$ | Dummy Variable | as needed | $l$ |

In total there are forty-three different variables in the telemetry stream from the ADCS test bed. All of the variables use floating point definitions except for the current RPM command variable which uses the *double* type variable. The dummy variable is useful as any other variable can be replace by an $l$ in the code rather quickly for troubleshooting and testing. At 10 Hz the number of variables in the telemetry has shown to be the approximate limitation that Tera Term can record accurately in real time as addition variables in the telemetry stream will cause significant dropouts and further loss of data. Data loss and correction will be discussed in further detail

in Chapter IV. Most of these variables were defined in Chapter II, however the rate estimation from a quaternion variable $\omega_{i\_ext}$ will be defined in the next subsection.

### 3.4.2 Body Rate Estimation

As lower quality and inherently cheaper gyroscopes are becoming better at drift rate estimation and detection it is important to characterize the CubeSat body rate $\omega_i$. This variable is calculated on-board the ADCS test bed and uses the gyroscope bias factors and the accelerometers to calculate an estimate for the current spacecraft body angular acceleration. To compare, we can compute a body-rate estimation without rate sensors by using equations presented by Sidi [18]. These body-rate estimation parameters are shown in Table 8 and are calculated from

$$\omega_{x-est} = 2(q_4\dot{q}_1 + q_3\dot{q}_2 - q_2\dot{q}_3 - q_1\dot{q}_4) \tag{65}$$

$$\omega_{y-est} = 2(q_3\dot{q}_1 + q_4\dot{q}_2 + q_1\dot{q}_3 - q_2\dot{q}_4) \tag{66}$$

$$\omega_{z-est} = 2(q_{c2}\dot{q}_1 - q_1\dot{q}_2 + q_4\dot{q}_4 - q_3\dot{q}_4) \tag{67}$$

where all other variables are previously defined in Chapter II. In the case that these estimates are more accurate than the on-board ADCS computed $\omega_i$ values they can simply be switched in the C code to alleviate gyroscope drift issues. For this reason the body rate estimates from the quaternion were programmed directly into the ADCS test bed control algorithm and are analyzed in Chapter IV.

### 3.4.3 Magnetic Field Test Conditions

The prior ADCS research at AFIT utilizing the Helmholtz cage [4] typically used an artificially strong magnetic field. This field was defined by [4] to be $[0, 2000, 0]$ mG which appears to be the limit of the magnetometer sensors in the IMU and of the external magnetometer used. A typical reading from the truth magnetometer inside the ADCS test bed is approximately $[153.2, 132.0, 450.9] \pm 5$ mG which gives a total magnetic field intensity of approximately $B = 494.2$ mG in the test bed at ambient Earth conditions. This does not include any effects from power lines in the walls nor the proximity of the ground station computer. Similar measurements have been observed frequently over the last year and are in a state of constant change. This research will attempt to lower the overall magnetic field down to a more realistic strength that a CubeSat might experience on orbit. To maintain the twenty-five year mission life de-orbit time-line a CubeSat should have an orbit perigee limited to approximately 500 km which will be the basis for selecting the strength of magnetic field. Using the WMM online calculator [5] the magnetic field intensity at this altitude is approximately $B = 471.2$ mG. If attitude estimation accuracy is achieved at the on orbit field strength, then the Helmholtz cage will be used to lower the field strength further. Two testing conditions are proposed if attitude estimation accuracy can be achieved at the on orbit field strength, the first is $[100.0, 100.0, 100.0]$ mG and the second is $[50.0, 50.0, 50.0]$ mG. The first provides a magnetic field intensity of $B = 173.2$ mG and the second $B = 86.6$ mG, which simulate orbit altitudes of approximately 2500 km and 5000 km respectively.

### 3.4.4 Static Testing

Typically, the PhaseSpace system and air bearing are not in operation as the main goal during a static test is to determine if the magnetometers are working

correctly or characterizing the RWA wheel responses. Static testing is useful for troubleshooting anomalies and calibrating the CubeSat ADCS software. Static testing was used extensively in this research to integrate the external magnetometer and to tune the RWA controller after it was moved away from the primary ADCS and IMU.

### 3.4.5 Dynamic Testing

Dynamic testing is conducted with the air bearing, Helmholtz Cage, PhaseSpace system, and all supporting software running on both the Owl Server and ground Station. The process of getting all of these systems working together at the same time can be rather time consuming. Dynamic testing typically includes reorientation maneuvers around the $z$-axis on the air bearing to characterize the performance of the PID controller in the ADCS test bed. The list below presents the actions required and the typical order to conduct a dynamic test on the ADCS test bed with full data collection. The purpose of this list is to document the process and best practices as there are safety concerns when working with high voltage and pressure vessels.

1. The ATMEL Studio file is programmed for the test and compiled onto the primary ADCS $\mu$controller. After compiling is finished, the CubeSat test bed is turned off, and the 485 bus line to the EPS is unplugged and the EPS is charged.

2. The PhaseSpace Owl Server and the CubeSat stylus in the test bed are turned on. Then the ground station Master Client GUI is connected to the Owl server. LED power level settings are adjusted until all eight markers can be seen in the Master Client GUI. The rigid-body tracker file is then assigned to the active markers.

3. If the Helmholtz cage is needed, the NI LABview software is activated to control

the polarity switches of the power supplies. Once the software is started, the three Helmholtz cage power supplies can be turned on and the power limits for the cage are set and the desired magnetic field is obtained.

4. The air compressor is turned on and brought to a pressure of 80 psi then the valve to the air bearing is opened.

5. The charger is removed from CubeSat ADCS test bed and the 485 bus line is reconnected. The air bearing stand is then lowered so the base of the semi-sphere is approximately 2 mm from the surface of the air bearing. The CubeSat is then turned on to reorient the laser pointer at the known balancing location marked on the wall. The system is then turned off and back on to reset the quaternion to $[0,0,0,1]^T$ in the new orientation.

6. Tera Term software is then opened and connected to the CubeSat Wi-Fi telemetry. The data must be saved manually by initiating the *Log* command and defining the directory to store the file. The *Record Data* button is then selected in the PhaseSpace Master client to record position data of the trackers.

7. A small perturbation about the $x$-axis is performed to aid in data synchronization during analysis. The CubeSat ADCS air bearing stand is then lowered onto the air bearing to conduct the test.

8. After test completion, both data loggers are stopped and the air bearing test bed is raised. The air bearing can only run for 15 minutes and is typically the first system to be shut off to avoid overheating of the air filtration system. All power supplies are brought to zero power and the software which controls them is terminated.

Step 1 in the list above can be performed hours before the test, but is dependent on the charge status of the EPS. Steps 2 and 3 are interchangeable, but connection issues with the PhaseSpace system are common and it is desirable to minimize the time high power is running through the Helmholtz cage. For dynamic testing the ADCS C code is programmed to hold at the initialized quaternion $[0,0,0,1]^T$ until the clock time reaches 60 sec as connecting Tera Term and lowering the air bearing test stand take about 10 sec. A better process for automated data collection is presented in Chapter V. Most of the testing in this research will focus on large angle slews (typically $\pm 90°$) about the $z$-axis. From large angle slews the data from the PhaseSpace can be compared to the ADCS test bed QUEST estimation with different Helmholtz settings.

### 3.4.6 Wheel Speed Control Authority Testing

To ensure the modifications made to the ADCS test bed are not adversely affecting the control authority, wheel speed testing will be conducted. Use of the dummy variable $l$ will aid in this testing as it can be used to replace the current RPM command variable $rpm_{ci}$. Plotting the dummy variable is helpful as well to investigate the RWA tachometer readings and wheel delay from the commanded speed. The output from the telemetry stream can also be compared to an external laser tachometer device which is the same used by Tibbs [4] A typical wheel speed control test example for a single wheel is shown in Table 6.

**Table 6. Example of Typical Static Wheel Speed Control Test**

| Wheel | Command (RPM) | Time into test (sec) |
|---|---|---|
| $x$ | $l = 0$ | $< 15$ |
| $x$ | $l = 1000$ | $> 30$ |
| $x$ | $l = 2000$ | $> 45$ |
| $x$ | $l = 3000$ | $> 60$ |
| $z$ | $l_2 = l + 1$ | $> 0$ |

The last line of Table 6 shows the use of a second dummy variable $l_2$ used for maximum motor RPM testing. These variables are very versatile as they update at 10 Hz which can be used in many ways such as magnetometer interference testing or calibrating the RWA PWM settings. Many of these speed control tests will be useful in determining whether or not the RWA is still introducing EMI into the IMU and external magnetometer which will be presented next.

### 3.4.7 Magnetometer Testing

The addition of the second magnetometer needs to be characterized throughout the different magnetic field strengths to see if it can be added into the QUEST algorithm. Additionally, the QUEST weighting of the second magnetometer needs to be investigated and defined. Initial testing will commence with the original configuration as used by Tibbs [4], where only the primary magnetometer and accelerometer sensors from the IMU are used while the weights in QUEST are both defined to be one. Initially the secondary magnetometer data will bypass the QUEST algorithm by setting the number of sensors $N$ to two and defining its weight to be zero. After initial testing is complete, $N$ in QUEST will be set to three and the second magnetometer will be set to one for further testing. If control cannot be achieved the weighting value of the second magnetometer will be lowered until control is achieved.

### 3.4.8 ADCS Controller Performance in Variable Magnetic Fields

To reduce the number of total test points the magnetometer testing documented in the preceding subsection will be conducted simultaneously during the ADCS controller performance testing. In order to characterize the controller performance a series of large angle slew tests were designed that would allow both research goals to be accomplished. The test will start with control about the origin of the ADCS ini-

tialization point $[0,0,0,1]^T$, then after sixty seconds the CubeSat will be commanded a -90$^o$ rotation about the $z$-axis. These test points are listed in Table 7.

**Table 7. Large Angle Slew Testing in Variable Magnetic Fields ($z$-axis)**

| Test | Maneuver | Time(sec) | Magnetic Field |
|---|---|---|---|
| 1 | No Maneuver | $< 60$ | N/A (Ambient Earth) |
| | $-90^o$ | $> 60$ | |
| 2 | No Maneuver | $< 60$ | [0,2000,0] mG |
| | $-90^o$ | $> 60$ | |
| 3 | No Maneuver | $< 60$ | [0,471,0] mG |
| | $-90^o$ | $> 60$ | |
| 4 | No Maneuver | $< 60$ | [100,100,100] mG |
| | $-90^o$ | $> 60$ | |
| 5 | No Maneuver | $< 60$ | [50,50,50] mG |
| | $-90^o$ | $> 60$ | |

Although the Euler angle is shown in Table 7 it is not used by the ADCS controller. For a -90$^o$ rotation about the $z$-axis the commanded quaternion $\bar{\mathbf{q}}_\mathbf{c}$ is $[0,0,-0.7071,0.7071]^T$ and is the same for all test cases listed in Table 7. After these tests are completed the second magnetometer will be activated in QUEST and these tests will be repeated to determine the sensor weighting of the second magnetometer.

### 3.4.9 Singularity Testing

It was easily discoverable early in the research during initial testing of the ADCS controller that the version of QUEST in the C code was the same as documented by Hall in [11]. This version of QUEST as mentioned in Chapter II has a singularity at $\pi$ radians or 180$^o$ about every axis as one of the three Rodrigues parameters will have a divide by zero error which can be seen in the respective quaternion. As the ADCS test bed is limited to control about the $z$-axis this singularity develops when the system is commanded to the quaternion $[0,0,\pm1,0]^T$. The $\pm1$ defines which

direction the controller will take, and $-1$ will be used as the initial rotation to $-90^o$ is used in the code. Two tests will be conducted to investigate the control authority around the singularity. The first test will start with control about the origin of the ADCS test bed initialization point $[0,0,0,1]^T$, then after sixty seconds the CubeSat will be commanded a -90$^o$ rotation about the $z$-axis. After another sixty seconds the CubeSat will be commanded a -80$^o$ rotation about $z$-axis for a total rotation of -170$^o$. The second test will command a rotation at the same time interval, but the second rotation will be -90$^o$ so that the CubeSat will end at 180$^o$ from the starting point. These two test are shown in Table 8 and will conducted first in the ambient Earth magnetic field and then the stronger [0,2000,0] mG field.

**Table 8. Singularity Testing (Rotation about $z$-axis)**

| **Test** | **Total Rotation** | **Time (sec)** | $\bar{\mathbf{q}}_\mathbf{c}$ **Command** |
|---|---|---|---|
| 1 | No Maneuver | $< 60$ | $[0,0,0,1]^T$ |
| | $-90^o$ | $> 60$ | $[0,0,-0.7071,0.7071]^T$ |
| | $-170^o$ | $> 120$ | $[0,0,-0.9962,0.0872]^T$ |
| 2 | No Maneuver | $< 60$ | $[0,0,0,1]^T$ |
| | $-90^o$ | $> 60$ | $[0,0,-0.7071,0.7071]^T$ |
| | $-180^o$ | $> 120$ | $[0,0,-1,0]^T$ |

Notice in Table 8 that the $\bar{\mathbf{q}}_\mathbf{c}$ command is listed because the C code doesn't calculate the Euler angle shown and is listed only to give the reader a quick reference. When the variable *cvs_time* is below sixty seconds after initialization the ADCS test bed is commanded to stay in the same location. This process helps the test operator start the data collection and recording systems. Since the PID control law uses the the error from this quaternion command, the control vector $\vec{u}$ should be considerably lower until *cvs_time* reaches sixty seconds and subsequently during the second rotation in the test.

If the singularity can be avoided or managed, further testing will be performed to investigate the range of control the 6U Cubesat ADCS offers. A four rotation test

will be commanded to investigate if the ADCS test bed can complete a $360^o$ rotation and return to the origin.

**Table 9. Four Corner $360^o$ Test (4 Rotations about $z$-axis)**

| Test | Total Rotation | Time (sec) | $\bar{\mathbf{q}}_\mathbf{c}$ Command |
|---|---|---|---|
| 3 | No Maneuver | $< 60$ | $[0,0,0,1]^T$ |
| | $-90^o$ | $> 60$ | $[0,0,-0.7071,0.7071]^T$ |
| | $-180^o$ | $> 120$ | $[0,0,-1,0]^T$ |
| | $-270^o$ | $> 180$ | $[0,0,0.7071,0.7071]^T$ |
| | $-360^o$ | $> 240$ | $[0,0,0,-1]^T$ |

The test outlined in Table 9 will only be conducted in the ambient magnetic field and the stronger [0,2000,0] mG field if the second magnetometer is found to change attitude estimation accuracy performance of the ADCS test bed with a any weighting less than $\frac{1}{2}$.

### 3.4.10 Error Metrics

The PhaseSpace system will be used to record an estimate of the true attitude of the CubeSat ADCS test bed throughout all dynamic testing presented in this thesis. The primary error metric to be used in analysis is the difference between the ADCS controller estimate calculated by the QUEST estimate of $\bar{q}_i$ and the truth measurement obtained by the PhaseSpace system which will be introduced now as $\bar{q}_{PSi}$. To better characterize this error the quaternions from both the ADCS test bed and the PhaseSpace system will be converted back into Euler angles in MATLAB as Euler angles are more commonly used to specify the control performance of an ADCS system [11]. The Euler angle representations offer more opportunity for analysis and characterization of the error at different commanded angles around the $z$-axis and can be compared directly with the results obtained and documented by Tibbs [4] through a process of interpolation described in detail later in Chapter IV. The quaternion

error that drives the PID controller is also an important metric as the PID control law should drive the error to zero about the $z$-axis. For this reason the quaternion error metric will also be characterized and converted to an Euler angle in this research using the same data interpolation approach.

## 3.5 Chapter Summary

Chapter III began by presenting an overview of the 6U CubeSat test bed. This overview covered the hardware used in the research and documented the physical properties both measured and estimated. These properties were then used to describe how the PID controller gains were selected followed by a brief introduction to the AFIT prototype ADCS. The second section provided an overview of the 6U CubeSat Software, ADCS algorithm and briefly discussed the MATLAB model used in the research. The chapter continued with overview of the PhaseSpace Impulse X2E motion capture system, including the hardware and software setup. The subsection was concluded by discussing how to edit the rigid-body data recorded how the data is post processed to return a quaternion. The last section in the chapter described which data would be collected and presented a way to estimate the body rate by using the quaternion. The section continued by describing the various test cases to be investigated which included magnetic field variations and the static and dynamic processes for testing a CubeSat. The next subsection described an example wheel speed test by using dummy variables to command the RPM in the RWA. Following the RWA testing the chapter continued by described ways to test the magnetometer, ADCS controller performance, and ways to investigate the presence of a singularity in the QUEST algorithm. The last section concluded with a brief overview of the error metrics that will be tracked and presented in Chapter IV.

# IV. Results and Analysis

Chapter IV presents the results and analysis from the data collected during testing, of the ADCS test bed. The first section details how the data will be manipulated to correct for telemetry dropouts and corrupted data points. Next the results of the simulation are discussed followed by the wheel speed control authority test results. The next two sections cover the characterization of the magnetometer and analysis of the ADCS test bed in the proximity of the singularity. The final two sections present the estimation and control accuracy of the ADCS test bed and error analysis.

## 4.1 Data Manipulation

To conduct any formal analysis from experimental testing it is important to document how and why the data collected is manipulated. Data manipulation is required in this research for three main reasons. The first is that the PhaseSpace data is post-processed and each data point is given a marker identifier in the CSV file, not an actual time stamp, which must be adjusted to match data from the ADCS test bed. The second reason is the MATLAB simulation begins a slew maneuver at time zero, while the ADCS test bed begins slewing at sixty seconds into the test. The ADCS test bed time must then be shifted to match the simulation time. This shift in time results in some of the ADCS parameters having negative time values. For this reason it is important to understand the data presented in this chapter has been adjusted to match the starting point in the maneuver. For the simulation analysis the data will be adjusted to begin at time zero, the simulation start time. For the analysis of the ADCS test bed with the PhaseSpace truth data, the truth data will be shifted to match the ADCS test bed time. The third and final reason for data manipulation is that collection rates and various forms of data corruption occur during data capture.

The following two subsections will cover how corrupted data is corrected and how some parameters were interpolated for later analysis in this research.

### 4.1.1 Corrupted Data Corrections

Data corruption can occur during any attempt to read, store, or process data on a computer system or during transmission of the data over a Wi-Fi device. The most common type of data corruption experienced in this research was degradation of the *csv_time* variable during collection with Tera Term which produced erroneous data plots until the corrupted data can be corrected. An example of data corruption in the *csv_time* variable is shown in Fig. 31.

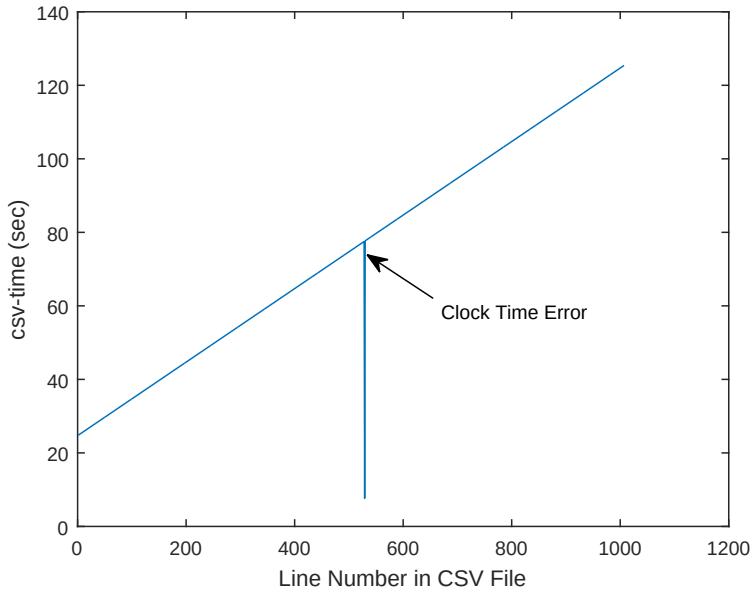


**Figure 31. Data Corruption in the Clock Timer Variable**

Fig. 31 shows that the *csv_time* variable recorded via Tera Term is missing the correct clock time for all the variables in that row of the CSV file. This issue can be easily fixed by replacing the collected value with an average of the data points before and after the corrupted data point. However, for the case presented in Fig. 31 the *csv_time* variable collected on Tera Term failed to record the first digit of the time

stamp. Further analysis of the CVS file shows that the rest of the telemetry values are recorded and only the first digit of the variable *csv_time* was corrupted. If this data is not corrected it results in erroneous data as shown when plotting any of the variables. Fortunately, this type of data error happened only a few times during the primary research test and was easily corrected. Other types of data corruption occur when the ADCS or C&DH perform an un-commanded time value reset. When this happens during a dynamic test the quaternion is initialized back to [0,0,0,1] and the data cannot be recovered easily without considerable time editing the CSV. This is unfortunate because only the PhaseSpace data is available for analysis. Most of the unrecoverable data corruptions arose during the static wheel speed test which will be covered in section 4.3.

### 4.1.2 Interpolation Methods used on ADCS Telemetry Data

In order to compare the ADCS test bed data to that collected from the PhaseSpace system, it is helpful to have the same number of data points for analysis in MATLAB. Since the data from the ADCS test bed is collected at 10 Hz while the PhaseSpace system is collected at 480 Hz, interpolation can be useful to compare two data sets. Also note that under sampling the truth source data is undesirable. This research uses the MATLAB *interp1* command utilizing the *pchip* method. This function is a shape-preserving piecewise cubic interpolation and can be seen used on the $q_3$ parameter collected from the ADCS test bed in Fig. 32. As shown in Fig. 32, the PhaseSpace system provides significantly more data points than the ADCS telemetry provides. Notice that the interpolated values preserve the original shape of the original trend of data points from the ADCS test bed telemetry. Fig. 32 also shows an important discovery that the PhaseSpace truth data is different than the ADCS test bed data. Data processed with the *interp1* function will be given an $i$ subscript as shown in Fig

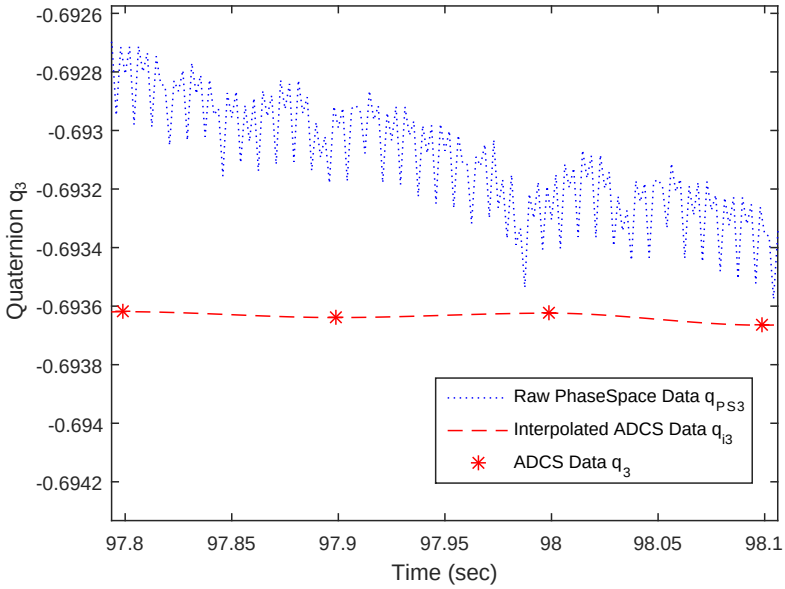


**Figure 32. Shape-Preserving Piecewise Cubic Interpolation on $q_3$**

32. This process of interpolation will only be used on the ADCS test bed quaternions when computing the Euler angles for use in performance analysis when comparing to the PhaseSpace truth data.

## 4.2 Simulated Results

This section presents the results from the simulated MATLAB model of the ADCS test bed and compares the results to one of the actual dynamic tests performed. The dynamic test case chosen for comparison to the MATLAB model was the $-90°$ large angle slew with the Helmholtz cage set at [0,2000,0] mG, without using the external magnetometer in QUEST. This case was chosen because the PhaseSpace truth data showed this was the most accurate test point and consistently maneuvered to the commanded $-90°$.

The MATLAB simulation model was used often in the research process to debug the ADCS test bed. It is interesting to note that the ADCS test bed was computing quaternions that made logical sense, but the quaternion error values didn't match

the MATLAB model. After the discovery of errors in the C code the performance of the ADCS test bed was improved. For this reason the quaternions of the model were compared to the most accurate large angle slew test of the ADCS test bed. Fig. 33 shows the attitude estimate from QUEST from the ADCS test bed and the PhaseSpace generated quaternions compared to the simulation results. As

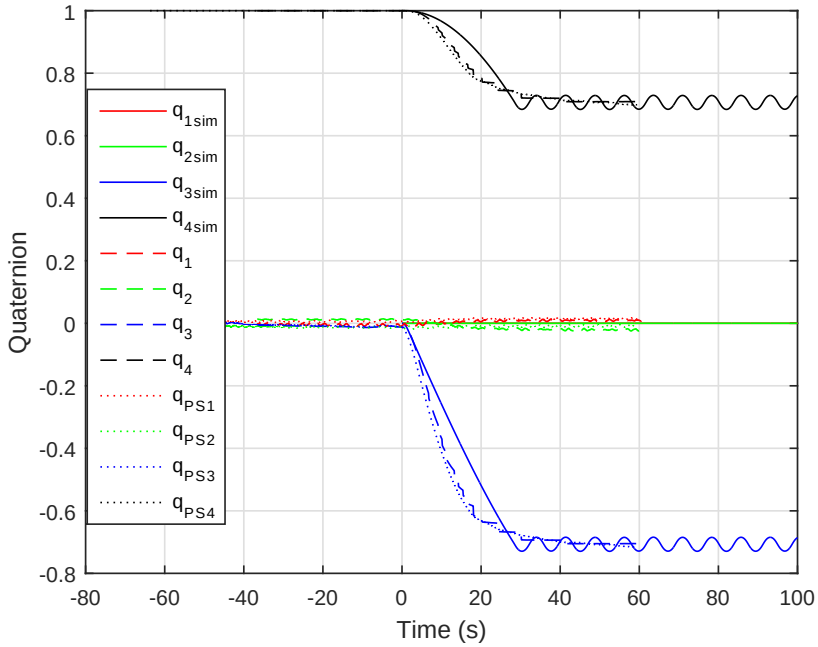


**Figure 33. MATLAB Simulation** ($q_{isim}$) **vs. ADCS Test Bed** ($q_i$) **and PhasePhase Data** ($q_{PSi}$)

shown in Fig. 33 the simulated response shows oscillatory behavior after the slew, while the ADCS test bed does not. After experimenting with the simulation in MATLAB it was determined that the oscillation in the model is due to errors in the estimated MOI matrix determined in Chapter III. Also notice that the PhaseSpace data and the ADCS test bed $q_3$ terms are closely correlated in this Helmholtz cage setting. Although both the simulation and the ADCS test bed are utilizing the same PID control law there are many unknown unknowns. For example the MATLAB model uses a constant wheel acceleration value by dividing a fixed torque by the MOI

of the reaction wheel $D_{RWA}$. Although this is an accurate way to calculate wheel acceleration, these two values are not exactly known. Even if $D_{RWA}$ is known to some degree of accuracy the MOI of the shaft and stator housing of the motor must be considered because they also rotate. Furthermore, when a BLDC motor is loaded, the torque range is not constant throughout the operating range of the motor. This is most noticeable at high RPM when the motor is reaching the maximum RPM which offers no additional torque. It also important to note that the MOI of the CubeSat $\boldsymbol{J_b}$ in the MATLAB model do not contain the off-axis cross products of inertia as they were not obtained during this research. As stated earlier the most useful data the model provided was the quaternion error $\bar{q}_e$. The simulated quaternion error is compared to the ADCS test bed as shown in Fig. 34, where you can see that the

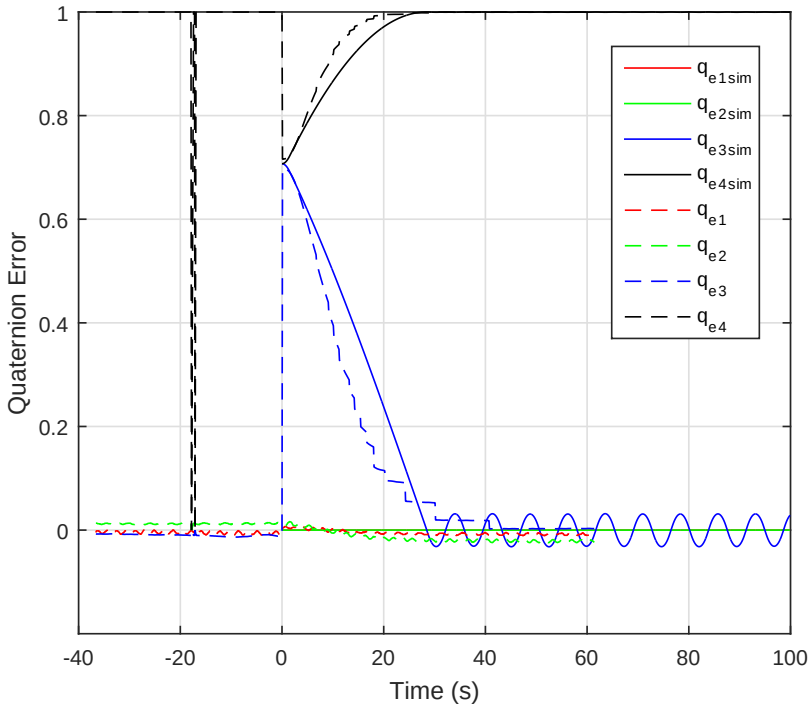


**Figure 34. MATLAB Simulation Quaternion Error vs. ADCS Test Bed**

quaternion error $q_{e3}$ and $q_{e3sim}$ are being driven near the vicinity of zero by the PID controller. This is the desired response although the simulation clearly shows the

undesired oscillatory behavior.

To further investigate the oscillations exhibited by the model the PID controller torque values from the ADCS test bed and the simulation are shown in Fig. 35. Fig. 35 shows that the $z$-axis responses of the simulation and the ADCS test bed

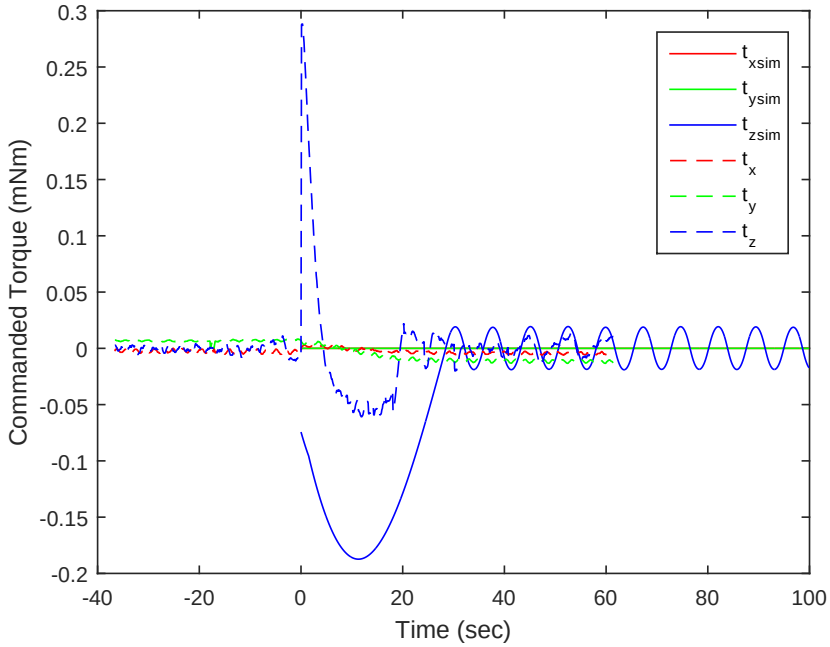


**Figure 35. Simulation Torque vs. ADCS Test Bed Torque Command**

are clearly different. The ADCS test bed at time zero shows an immediate spike to 0.2885 mNm while the simulation begins with a smooth commanded torque down to -0.1873 mNm. Approximately four and a half seconds into the test the ADCS test bed begins to follow the torque commands of the MATLAB model. A zoomed in view of the torque commands is shown in Fig. 36, which shows that the torque commands are similar in magnitude after the slew maneuver. The difference in commanded torque is because the MATLAB simulation propagates Euler's rotational EOM with the function $ODE45$, which is more accurate than the updated torque commands calculated on the ADCS $\mu$controller at only 10 Hz. This means that the resolution of the data in the simulation is not representative of how the ADCS test bed actually

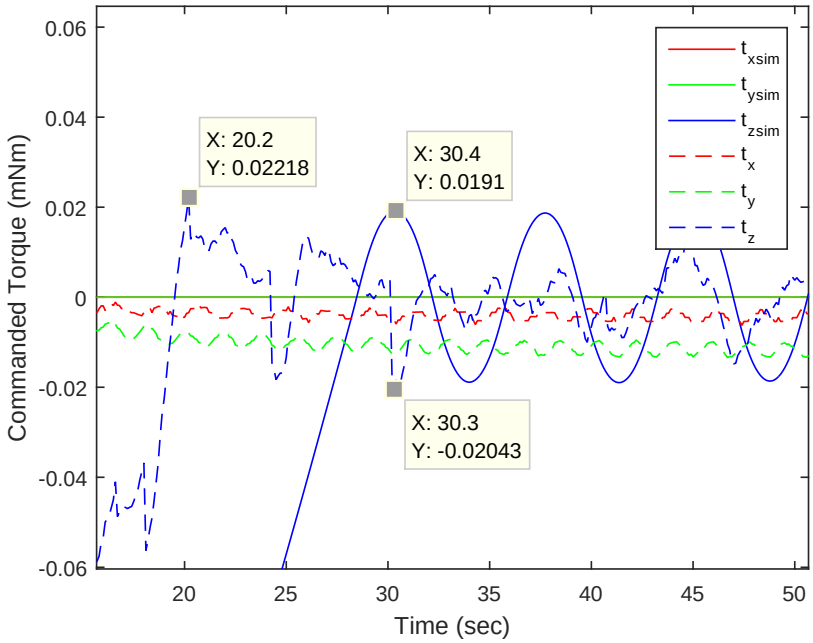


**Figure 36. Simulation Torque vs. ADCS Test Bed Torque (Zoomed in)**

performs calculations. The statistician George Box is quoted for saying *"All models are wrong, but some are useful,"* [15] which is particularly applicable to the simulation model used in this research. The MATLAB model aided in the discovery of coding errors on the ADCS test bed which ultimately led to the successful integration of a quaternion error PID controller.

## 4.3 Wheel Speed Control Authority Analysis

The ADCS test bed used in this research was reconfigured to move the RWA away from the IMU to reduce EMI with the magnetometer. Because it was moved, it is important to characterize the performance of the primary ADCS control card and its ability to command the secondary $\mu$controller used to control the RWA. There was concern that the motors would become damaged during testing as many motors were replaced during previous testing. The decision was made to hard code a RPM limiter to command the RPM variables $rpm_x$, $rpm_y$, and $rpm_z$ to stay below an operational

speed of 6500 RPM. The first test presented is the RWA maximum speed test to ensure that this C coded RPM limiter was working correctly. The Monarch laser tachometer was used to observe the maximum RPM during testing. Although the exact time stamp of the tachometer measurement isn't known with exact certainty the telemetry from the ground station was used as an estimate. The dummy variable $l$ was used as the commanded RPM input in the form of $l = l + 1$ as shown in Table 9 in Chapter III. Since the algorithm updates at 10 Hz, the RPM will increase at the rate of 10 RPM per second. The zoomed in results from the maximum speed test and the Hall sensor tachometer variables $rpm_x$, $rpm_y$, and $rpm_z$ from the second $\mu$controller on the RWA are shown in Fig. 37.

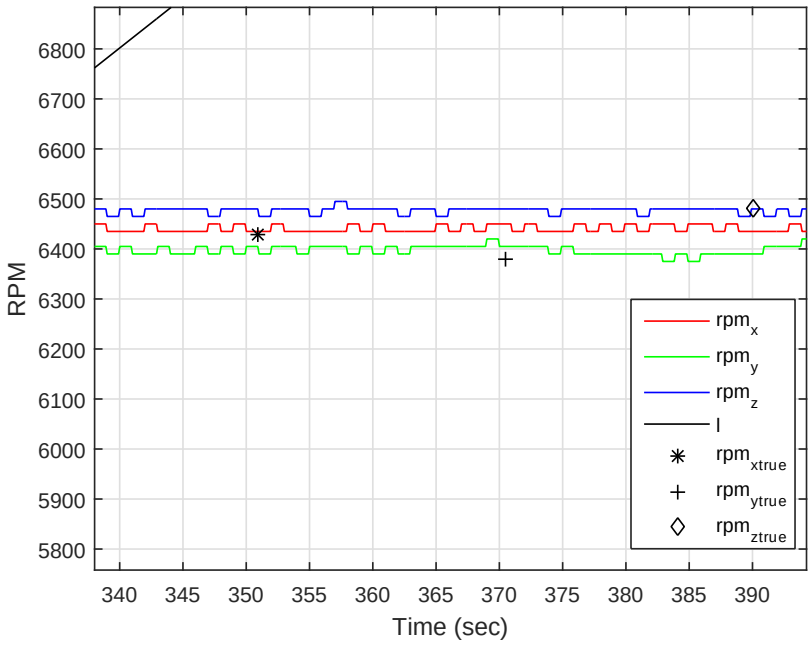


**Figure 37. Maximum RPM with Truth Data Points**

Fig. 37 shows that the RPM limiter command in the C code was working effectively by keeping the RPM of each wheel below 6500 RPM. Also notice that the external laser tachometer values are in the vicinity of the current tachometer reading from the Hall sensors. The commanded $l$ variable can be seen in the upper left corner

of Fig. 37. In comparison, the current RPM commanded variable $rpm_{cx}$, $rpm_{cy}$, and $rpm_{cz}$ is plotted with the same truth measurements in Fig. 38.

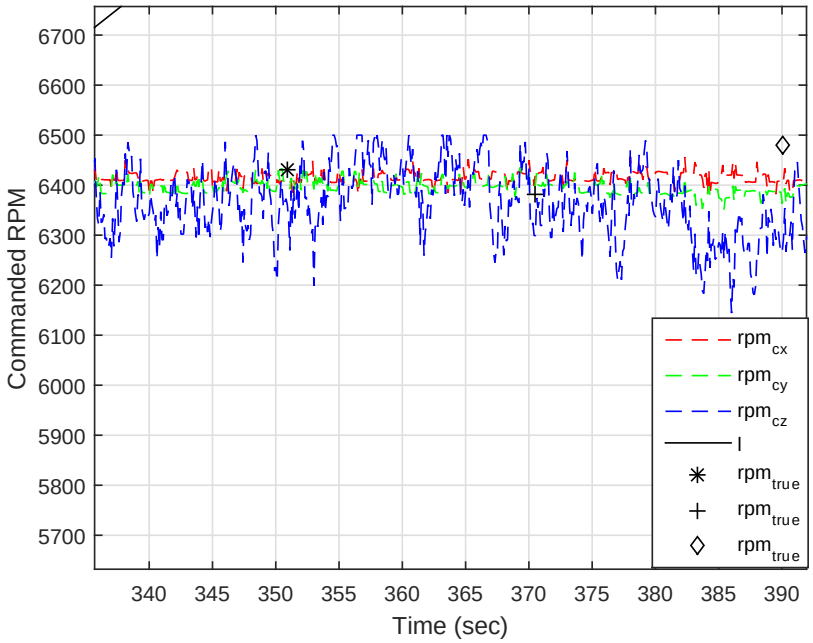


**Figure 38. ADCS Test Bed RPM Command**

Fig. 38 shows that the RPM commanded variables calculated by the primary ADCS $\mu$controller contains significantly more noise in the signal. It is theorized that the difference in noise found between the $rpm_i$ and $rpm_{ci}$ variables is due to the number of interrupts on the primary ADCS $\mu$controller. The second $\mu$controller on the RWA has significantly less interrupts commands than the primary $\mu$controller. The second $\mu$controller's sole function is to read the commanded RPM from the primary ADCS $\mu$controller, control the wheels, and then send the current RPM reading back to the primary ADCS $\mu$controller via the cross link cable. Even with the noise level of the commanded RPM variable the RPM limiter function worked well in this test as evident in Fig. 39.

Fig. 39 shows a zoomed out view of Fig. 38, but additionally shows the current commanded RPM variables $rpm_{cx}$, $rpm_{cy}$, and $rpm_{cz}$. Notice that the noise level

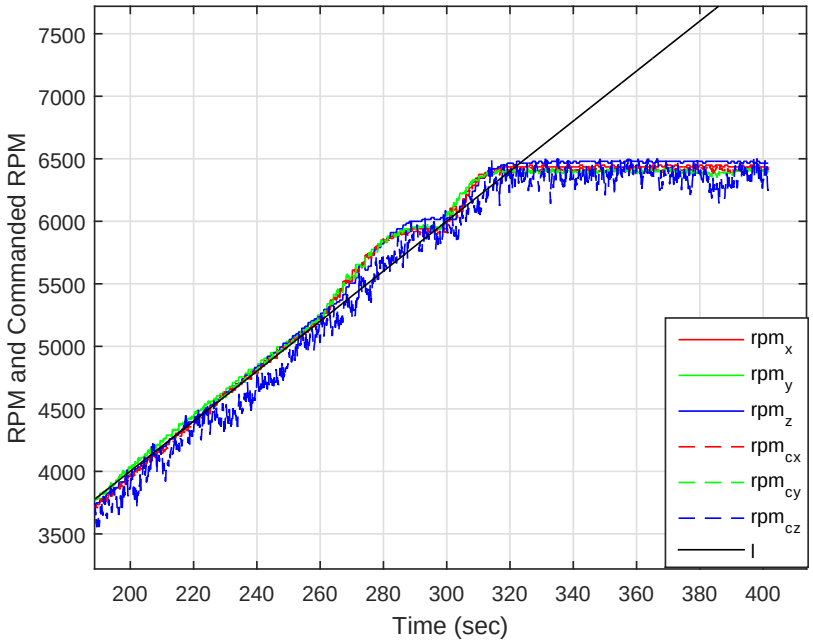


**Figure 39. RPM Limiter Test**

follows the dummy command $l$, until the limit of 6500 RPM is reached. The next test uses the dummy variable $l$ to perform a series of stepped RPM commands. The RPM values and the corresponding time of the commands are shown in Table 10 while the results are shown in Fig. 40.

Notice that the commanded $RPM_{cz}$ variable spikes to -20,000 RPM upon initialization. Also notice that the $RPM_{cx}$ and $RPM_{cy}$ variables deviate from the commanded $l$. This is a cause for concern as these variables should be tracking the commanded $l$. At approximated 475 seconds into the test the $x$-axis wheel failed to follow the commanded RPM and immediately maxed out at approximately -4800 RPM before it is commanded again. The $z$- and $y$-axes wheels continued to follow the commanded RPM found in Table 13. Closer inspection of Fig. 40 showed small deviations occurring whenever the $l$ variable jumped from one command to the next. This was evident in the larger deviations of $RPM_{cz}$ in Fig. 40, but is shown in greater detail in Fig. 41.

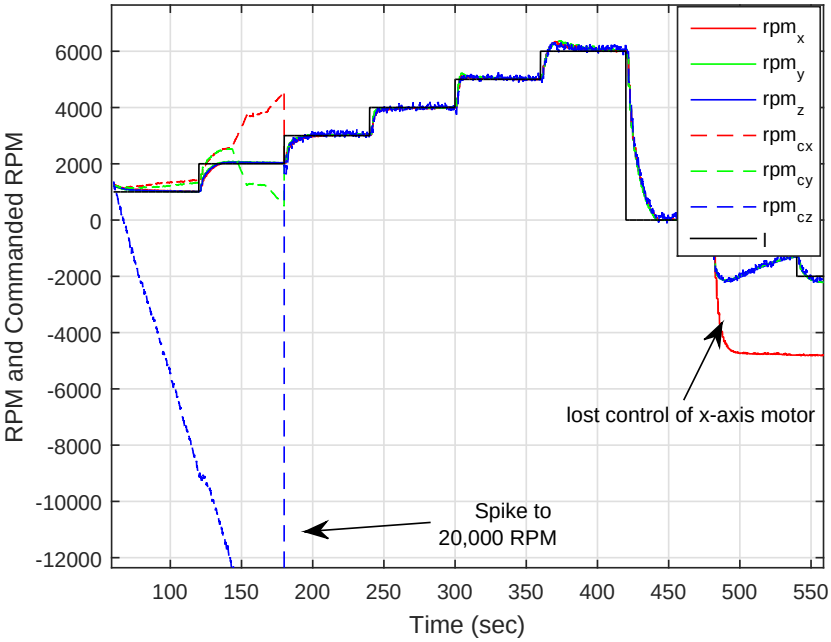


**Figure 40. Stepped High Speed Control Test**

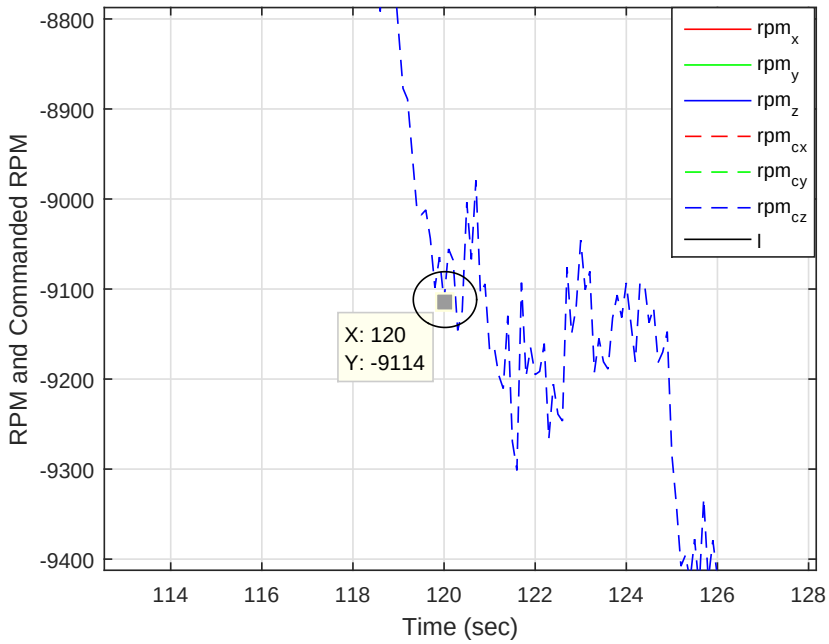


**Figure 41. Zoom View of RPM Command Noise**

**Table 10. Stepped High Speed Control Test (Static)**

| Command (RPM) | Time into test (sec) |
|---|---|
| $l = 1000$ | $< 60$ |
| $l = 2000$ | $> 120$ |
| $l = 3000$ | $> 180$ |
| $l = 4000$ | $> 240$ |
| $l = 5000$ | $> 300$ |
| $l = 6000$ | $> 360$ |
| $l = 0$ | $> 420$ |
| $l = -1000$ | $> 480$ |
| $l = -2000$ | $> 540$ |
| $l = -3000$ | $> 600$ |
| $l = -4000$ | $> 660$ |
| $l = -5000$ | $> 720$ |
| $l = -6000$ | $> 780$ |

Comparing Fig. 40 to Fig. 41, notice the $RPM_{cz}$ deviation appears negligible in Fig. 40. However Fig. 41 shows a much closer view of the variable and further analysis showed this was occurring every sixty seconds when $l$ changed. The variable $l$ is a system variable and is not based on any external sensors or physical properties of the ADCS test bed. As discussed in Chapter II, current research is investigating sources of OS noise in high performance systems [27]. Before the final static test is presented, it is important to understand how the $l$ variable is defined in the ADCS test bed algorithm. Upon initialization, $l$ is defined in the main attitude control directory as a floating point value set to zero. After QUEST is called in the algorithm, the main control loop is activated. In the loop, the variable $l$ is then given an integer value for the desired test, but is still a *float* type variable in C code. Also, recall from Chapter III that the only *double* type C code variable in the telemetry list was the current RPM command $RPM_{ci}$. It is the author's theory that the conversion of the *double* type values to *float* value format in C code is causing noticeable OS noise. This noise develops because the precision of the *double* variable is lost during each conversion to a *float* type. This can become a problem if all the calculations are done

in double type variables beforehand and then converted to a *float* before it is used in the C code. A final test was devised to test this theory and investigate what would happen if the $l$ variable changed type during the test. The last static test employing the use of variable mismatch is shown in Table 11.

**Table 11. Two Step Low Speed Control Test (Static) Variable Type Mismatch**

| Command (RPM) | Time into test (sec) |
|---|---|
| *float* $l = 200$ | $< 60$ |
| *double* $l = 0$ | $= 60$ |
| *float* $l = -200$ | $> 60$ |

As Table 11 shows the variable $l$ will be converted a *double* type and set to zero when the clock time reaches sixty seconds. The next update will convert $l$ back to a *float* value. The results of test are shown in Fig. 42.

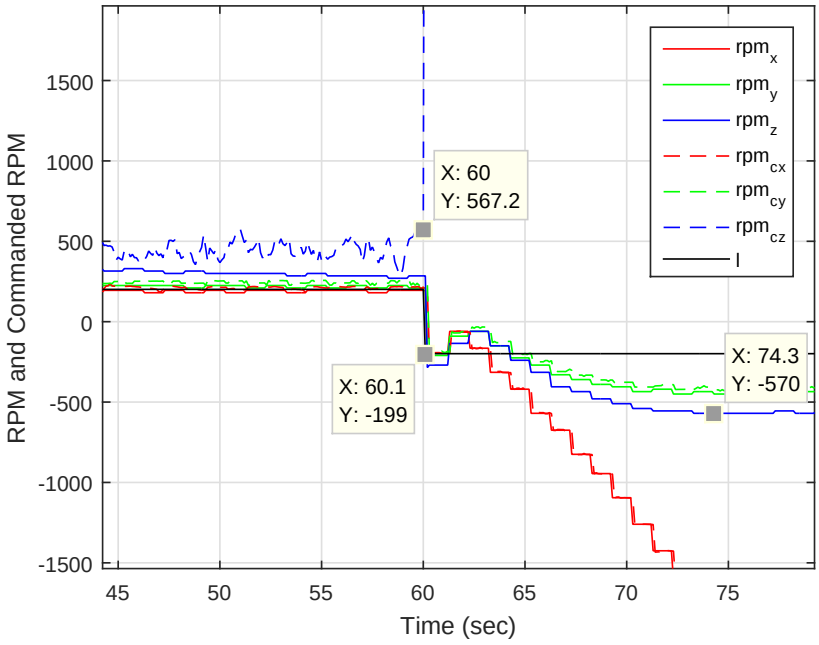


**Figure 42. C Code Variable Type Mismatch Effects on $RPM_{ci}$**

Notice in Fig. 42 that when the clock time reaches sixty seconds the $RPM_{cz}$ variable goes vertical. Also note that at 60.1 seconds the value of $l$ is -199. Shortly

after this transition the $x$-axis wheel failed to follow the commanded RPM and begins following the now erroneous $RPM_{cz}$ value. However the $z$- and $y$-axes wheels continue to track on the desired RPM. This highlights the importance of proper variable definitions in C code when performing calculations. As alluded to in the simulation results, the torque command $t_z$ on the ADCS did not match the simulation model. Investigation of the code showed that there were numerous mismatches of variable type. The most notable was the discovery that the torque command in the ADCS test bed is defined to be a *float* type. This value is converted to a RPM speed and stored in the *double* type variable $RPM_{ci}$ which should not present a problem in C code. The issues develops when a *double* type is stored in a *float* type value in C as some precision is lost [43]. It is also important to note that this conversion goes through at least three operations before it is later converted to a PWM command and sent to the RWA. To analyze this potential issue further, the commanded RPM $RPM_{ci}$, current RPM $RPM_i$, and controller torque $t_i$ variables are plotted from the dynamic four corner 360° test shown in Table 12 in Chapter III. The test data was conducted with the Helmholtz cage set to [0,2000,0] mG. The RPM variables for the four corner 360° test can be seen in Fig. 43, noting that only the first two maneuvers from 0° to 90° along with the first portion of the 90° to 180° are shown. Notice in Fig. 43 that only the $y$- and $z$-axes wheels are tracking their respective RPM commands. The $x$-axis wheel command is off by approximately 500 RPM. Also note from Fig. 43 that the $x$-axis stopped tracking its commanded value at sixty seconds into the test which is the same time the maneuver command is given. To further show that the $RPM_{cx}$ is erroneous within the OS of the ADCS test bed a plot of the commanded torque is shown in Fig. 44. As shown in Fig. 44, the $x$-axis torque command computed by the PID control law is approximately 0.00254 mNm, but the wheel begins to increase its RPM as shown earlier in Fig. 43. It should be noted that the $x$-axis continued to

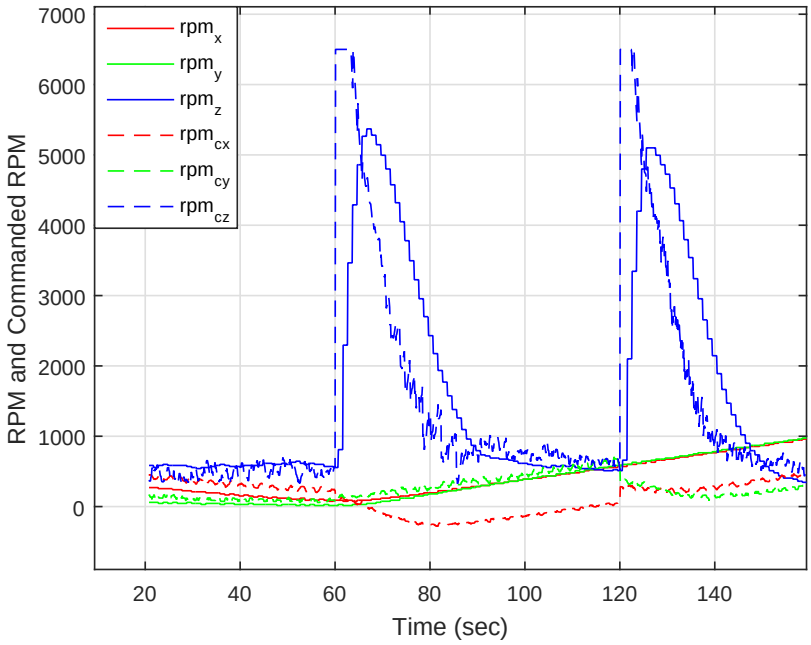


**Figure 43. RPM Command Faults during Dynamic Testing**

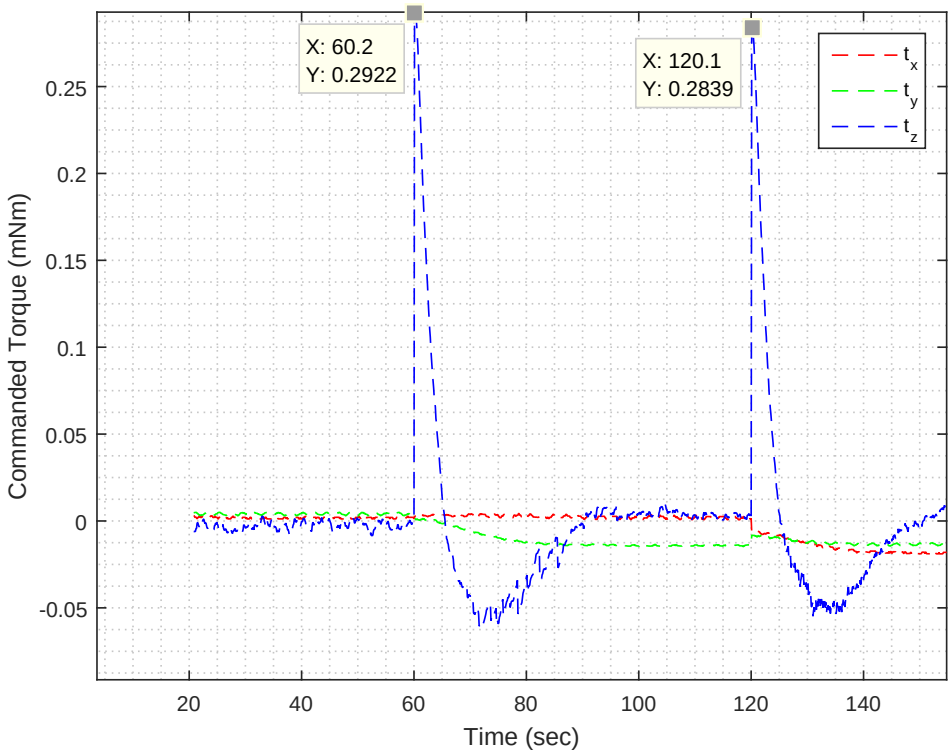


**Figure 44. Commanded Torque during Dynamic Testing**

exhibit erratic behavior in other wheel speed testing not presented in this research and throughout the dynamic control experiments presented later in the chapter.

## 4.4 Magnetometer Characterization

With the addition of a second external magnetometer to the ADCS test bed it's important to characterize the EMI and accuracy of the two sensors after the displacement of the RWA. This section discusses the steps leading up to the addition of the second magnetometer measurement in QUEST and presents the data collected from static and dynamic testing in various magnetic fields. An easy way to compare the quality of two magnetometers is to check the magnitude $B$ using Eq. (46) as seen on page 25 in Chapter II. The magnitude $B$ shows if the magnetometers are calibrated correctly and can be used to determine if the magnetometer values are being influenced by EMI. Note that the plots in the next two subsections are using a five variable rolling average of the magnetometer values from the telemetry. The primary magnetometer variable is $M_{1i}$, while the second external magnetometer variable is $M_{2i}$. The primary magnetometer raw sensor data $M_{1iraw}$ along with the Kalman filtered primary magnetometer data $KM_{1i}$ are listed in the subsection on filtering analysis. The last subsection presents the results of adding the external magnetometer into QUEST.

### 4.4.1 EMI Static Test Results in Ambient Earth Field

In order to see if the RWA is still inducing EMI into the magnetometer sensors the data during the telemetry from the static RWA tests were analyzed. To check the accuracy of the sensor measurement, the magnitude of the truth magnetometer from the ground station is compared to the magnitude of each of the two magnetometers in the ADCS test bed. The magnetometer readings from the stepped high-speed control

test of the RWA shown in Table 13 are plotted in Fig 45. In Fig. 45, $B_1$ and $B_2$

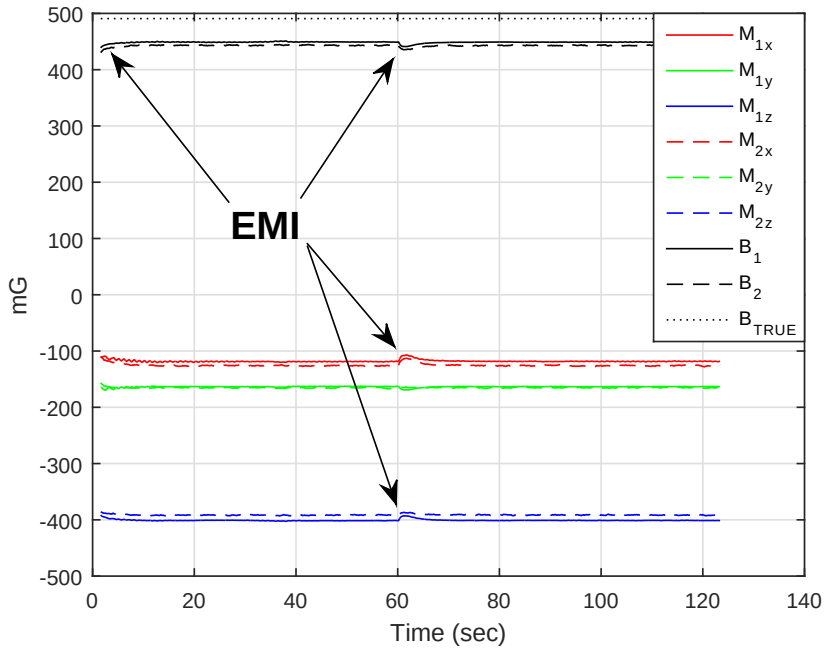


**Figure 45. EMI During Static High Wheel Speed Test**

are the magnitudes of the primary and secondary magnetometer, respectively. The true magnitude $B_{TRUE}$ is also plotted for comparison. Notice in Fig 45. that EMI is only present during the start of the test when the RWA wheels begin to spin and at sixty seconds when the RWA wheels change direction. The EMI caused by the RWA changes the magnitude of both $B_1$ and $B_2$ by approximately 10 mG during the direction change at sixty seconds. Note also that the magnitude of both sensors is different than the true magnitude. The primary magnetometer is different than the true magnitude by 41.8 mG throughout the test while the external magnetometer reads a difference of 47.6 mG. Although the magnitudes of the two sensors are different the individual $x$-, $y$-, and $z$-axes readings remained consistent during the static tests. An attempt was made to further calibrate and bias both of the sensors with the Helmholtz cage off, but better accuracy could not be achieved.

The magnetometer readings from both the maximum speed test and the two-step

low-speed control test showed no observable EMI. It appears that the displacement of the RWA from the IMU magnetometer was successful in reducing the amount of EMI in the ambient magnetic field with the Helmholtz cage off. Next, the two magnetometers are compared in a dynamic environment.

### 4.4.2 Magnetometer Performance during Dynamic Tests

To characterize the magnetometers in a dynamic environment, the telemetry data from the large angle slew testing from Table 10 in Chapter III are discussed. These five test conditions provide a variable range of Helmholtz cage settings that will help characterize the two magnetometers in the ADCS test bed. The first test in Table 10 was a 0° to -90° maneuver in a ambient Earth magnetic field with the Helmholtz cage off. The magnetometer results from the test are shown in Fig. 46 which shows

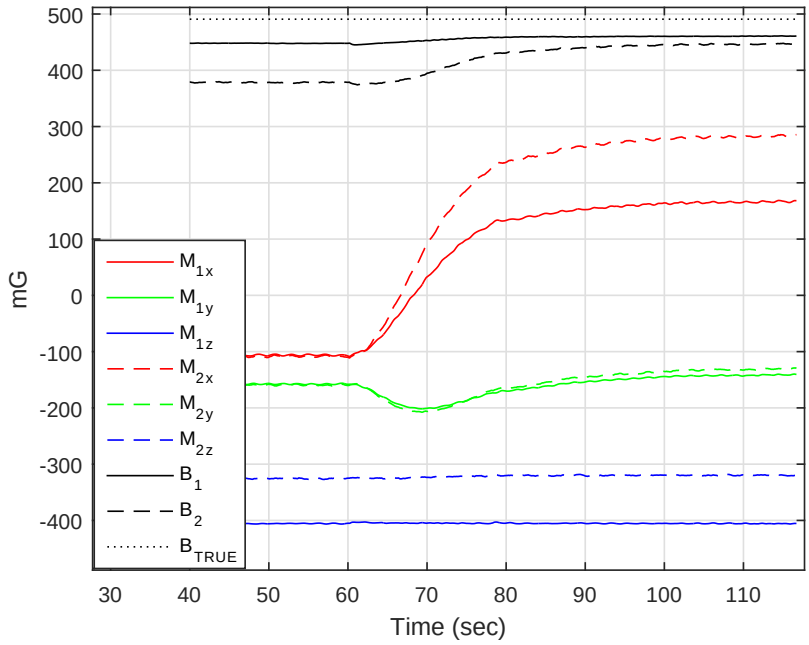


**Figure 46. Magnetometer During 90° Slew (Helmholtz Cage Off)**

the magnitude $B_2$ of the second external magnetometer increases during the slew maneuver. Notice that the increase in magnitude is primarily from the $M_{2x}$ reading.

The total increase in $B_2$ of the external magnetometer is 68.4 mG. This is cause for concern because the change in magnitude shows that the second magnetometer is not producing reliable sensor measurements in a dynamic environment. This means that the sensor is not calibrated correctly and may perform poorly in variable magnetic fields. Also notice that the $B_1$ does change slightly during the maneuver as well. The difference in magnitude for the primary magnetometer in the IMU was determined to be 12.8 mG.

The second test utilized the Helmholtz cage with a setting of [0,2000,0] mG and performed the same 0° to -90° maneuver. The magnetometer readings from both sensors along with their magnitudes are shown in Fig. 47. Notice in Fig. 47 that

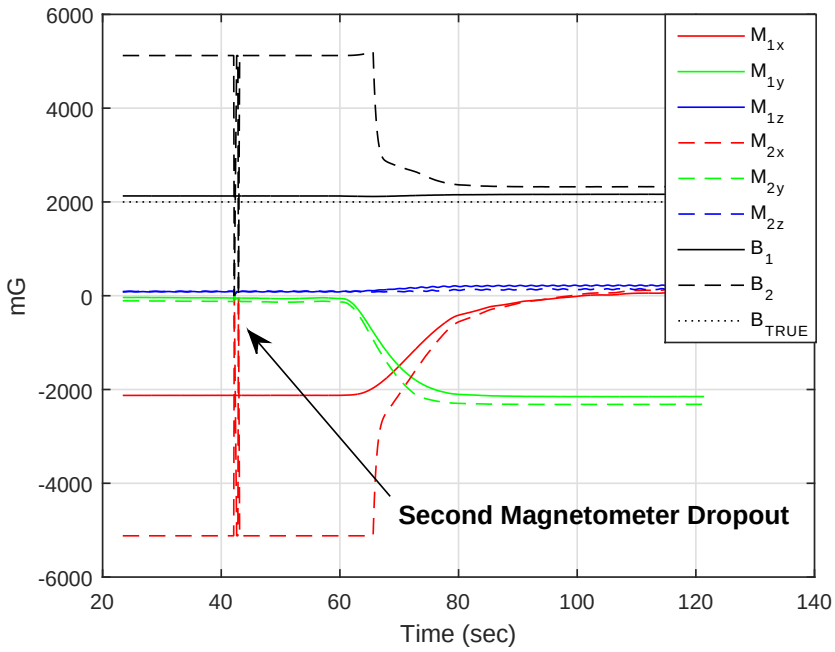


**Figure 47. Magnetometers in 90° Slew Test 2**

the second magnetometer shows a magnitude several times higher than the true magnitude $B_{TRUE}$ that was produced by the Helmholtz cage. The second magnetometer produced a steady magnitude $B_2$ of approximately 5122 mG until sixty seconds into the test. When the ADCS test bed was commanded to move the second magnetome-

ter reading began to drop reaching a final value of 2324 mG in the -90° orientation. Also note that the primary magnetometer magnitude $B_1$ is greater than $B_{TRUE}$. At the beginning of the test, the primary magnetometer magnitude $B_1$ was 2128 mG and increased to approximately 2163 mG towards the end of the maneuver. This increase of 35 mG is due to the limitations of the primary magnetometer sensor, because each axis has a different tolerance and accuracy. The third test uses a Helmholtz cage setting of [0,471,0] mG which depicts the magnetic field magnitude of a typical 500km orbit and the results are shown in Fig. 48. Notice that the second magnetometer

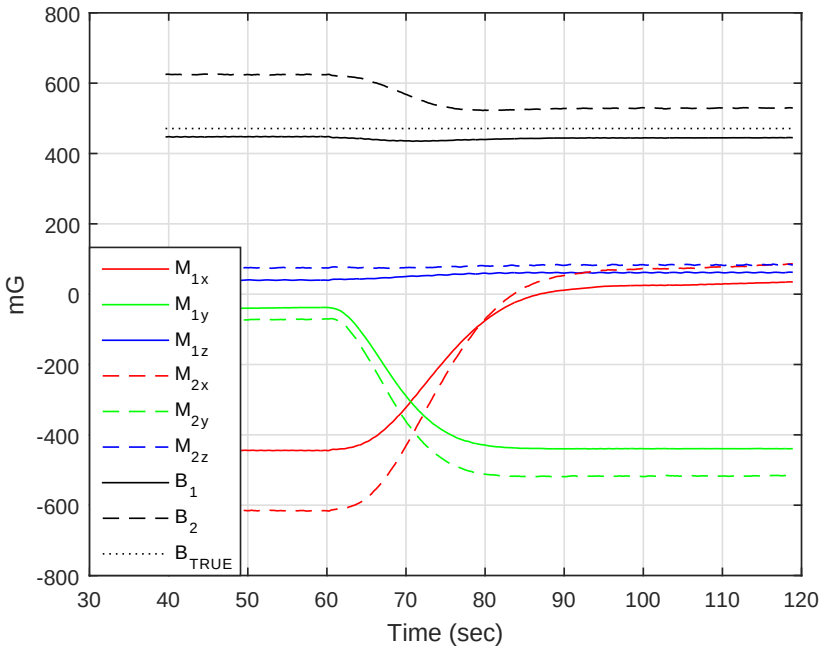


**Figure 48. Magnetometers in 90° Slew Test 3**

magnitude $B_2$ is still changing throughout the maneuver. The total change for $B_2$ is 95.5 mG while the primary magnetometer only changed 2.4 mG during the test. It is now clear that the second magnetometer would require extensive biasing and calibration if it were to be used on a CubeSat mission. The deviation in magnitude $B_2$ during the dynamic test would cause degradation of the QUEST quaternion estimate. The magnetometer results from the fourth and fifth test show similar results of Fig.

48 and is summarized in Table 12.

**Table 12. Dynamic Magnetometer Results (0° to -90° Slew)**

| Test | Magnetometer | $\Delta B$ | Helmhotz Cage Setting | $B_{TRUE}$ |
|---|---|---|---|---|
| 4 | $M_1$ | 8.1 mG | [100,100,100] mG | 173.2 mG |
| | $M_2$ | 51.9 mG | | |
| 5 | $M_1$ | 4.8 mG | [50,50,50] mG | 86.6 mG |
| | $M_2$ | 47.2 mG | | |

The previous test results and the data in Table 12 show that the second magnetometer cannot provide consistent magnetic field magnitude data for QUEST. This means that the Atmel ATAVRSBIN2 used as the second external magnetometer on the ADCS test bed was not properly calibrated in the ADCS C code for this research. Achieving the manufacturer's listed accuracy of ±1° would require further calibration and biasing and is discussed in greater detail in Chapter V.

### 4.4.3 Filtering Analysis

The previous subsection showed that the displacement of the RWA away from the primary magnetometer removed the main source of EMI on the magnetometers experienced in Tibbs' research [4]. His implementation of a rolling average filter is compared to a discrete time Kalman filter used on the ADCS test bed. The results of the Kalman filtered magnetometer data $KM_{1i}$ compared to the moving average filter $M_{1i}$ along with the raw data from the Analog Devices IMU $M_{1iraw}$ are shown in Fig. 49

The data in Fig. 49 is from the 0° to -90° test maneuver in a ambient Earth magnetic field with the Helmholtz cage off. Fig. 49 is a close up view of the $x$ and $y$-axes magnetometers near the time the maneuver was commanded. The $z$-axis data stayed constant throughout the test and doesn't compare how the filters are operating and is not shown. Fig. 49 shows the Kalman filter lags the raw data

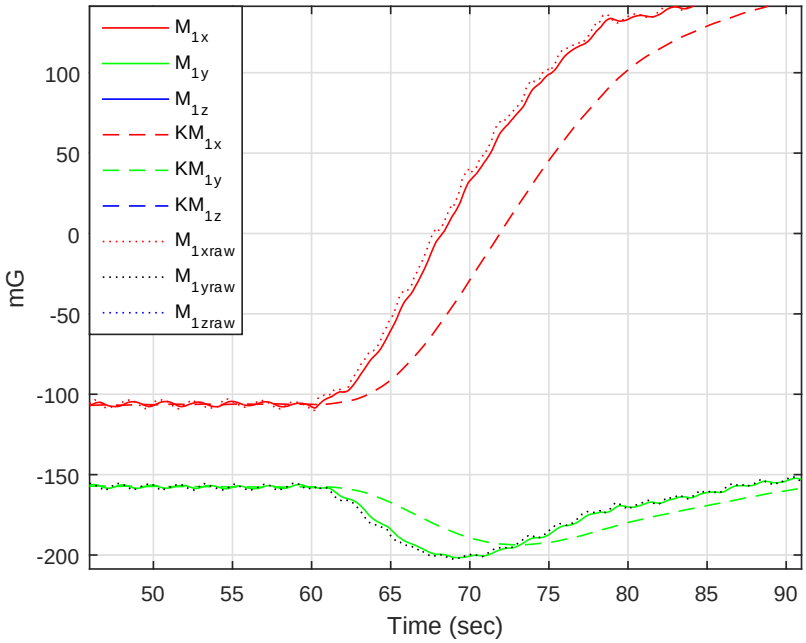


**Figure 49. Primary Magnetometer Filtering vs. Raw Data** $M_{1iraw}$

approximately three seconds during the maneuver. This time delay is undesirable, but could be manageable if the rotation rate of the ADCS test bed were reduced. The rolling average filter delayed the raw sensor data from the primary magnetometer by approximately $\frac{1}{3}$ of a second. The lag from the Kalman filter was expected and is more evident if the initial estimate is unknown. The Kalman filter used in the research takes the first estimate to be zero and then receives new measurements from the sensor data. The delay is significant upon initialization of the ADCS as shown in Fig. 50. Notice in Fig. 50 the Kalman filter estimate requires approximately eighteen seconds before it's within the vicinity of the raw magnetometer data. The issues discovered during the magnetometer testing highlighted the utility of the moving average filter used by Tibbs [4]. The filter is used on both the primary and secondary external magnetometers for all remaining test points. It should be noted that the Kalman filter programmed in the ADCS test bed was originally tuned to filter the RWA's RPM measurements and was not correctly tuned for the magnetometers before testing. To

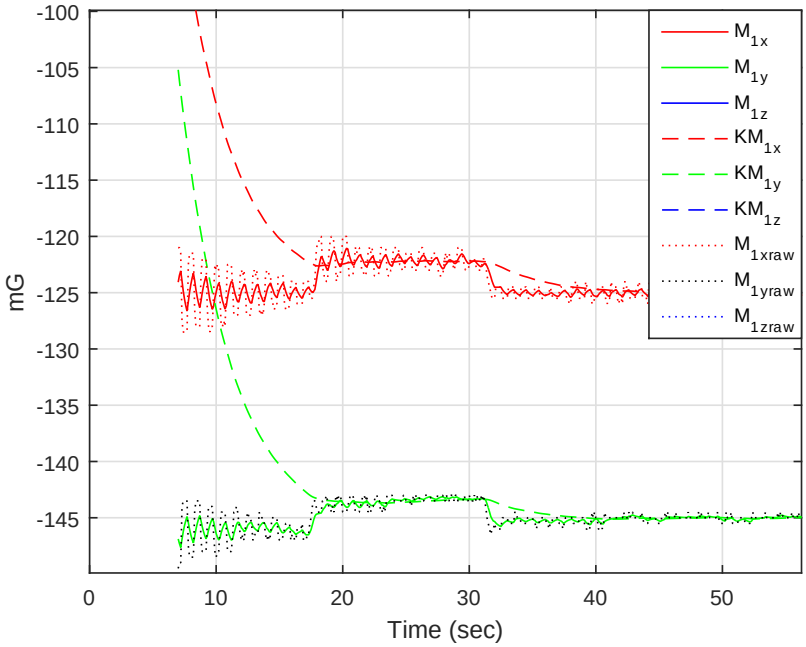


**Figure 50. Filtered Delay On ADCS Test Bed Initialization**

decrease the lag time upon initialization the first sensor measurement could be used for the initial estimate and would provide better results. Zero was a logical choice for the RPM filter as the wheels should not be moving upon start-up of the ADCS test bed. It was also discovered that the Analog Devices IMU has four finite impulse response (FIR) filtering options already installed on the inertial sensor. Unfortunately, the ADCS C code was using the fifth "default" option during testing which provides no filtering. More discussion on implementing the FIR filters and tuning the discrete-time Kalman filter can be found in Chapter V. The next subsection presents the addition of the external magnetometer sensor measurement into QUEST.

### 4.4.4 Addition of External Magnetometer into QUEST

As expected the external magnetometer would require further calibration and biasing to improve the sensor accuracy. One of the secondary goals of the author's research was to investigate the effects of adding a degraded measurement vector into

QUEST. Table 13 lists the corresponding QUEST parameters and Helmholtz cage settings used in this research.

**Table 13. Experimental QUEST Testing (0° to -90° Slew)**

| Test | $M_2$ Weight ($w_k$) | $\lambda_{opt}$ | Helmhotz Cage Setting |
|---|---|---|---|
| 1 | 1 | 3 | Helmholtz Off |
| 2 | 0.5 | 2.5 | Helmholtz Off |
| 3 | 1 | 3 | [0,2000,0] mG |
| 4 | 0.5 | 2.5 | [0,2000,0] mG |
| 5 | 0.1 | 2.1 | [0,2000,0] mG |

As seen in Table 13 the second external magnetometer weight begins at one. This weight is equal to the weight of the other two QUEST sensor measurements from the Analog Devices magnetometer and accelerometer. Fig 51 shows the quaternion from the QUEST calculation on the ADCS test bed and compares it to the truth source quaternion from PhaseSpace during Test 1. Notice from Fig. 51, that even before the

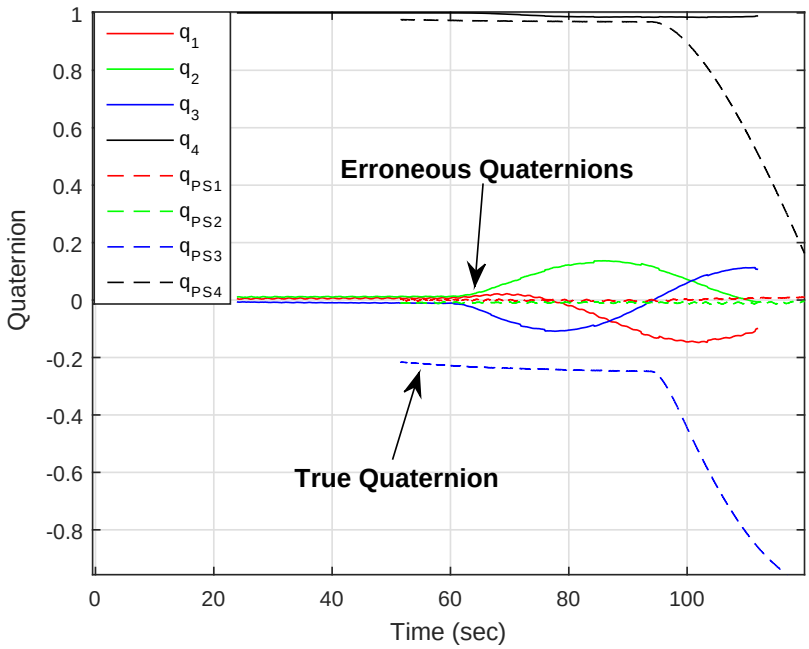


**Figure 51. External Magnetometer $\omega_k = 1$ QUEST Test 1**

commanded maneuver at sixty seconds the truth data from PhaseSpace is different

than the quaternion from the ADCS test bed. This was observed during the test during the initial sixty seconds of the maneuver as the ADCS test bed did not stay at 0° as commanded. The ADCS test bed started to drift and as Fig. 51. shows the quaternion from QUEST was still $[0,0,0,1]^T$ until sixty seconds. At sixty seconds, the commanded quaternion $[0,0,-0.7071,0.7071]^T$ caused significant error in all quaternion values. Notice the PhaseSpace data in Fig. 51 shows that the ADCS test bed overshot the commanded orientation. The data recording was stopped shortly before the ADCS test bed rotated 180° as it was clear that the ADCS test bed was uncontrollable with the current QUEST settings. The results of lowering the weighting of the external magnetometer in QUEST to 0.5 from Test 2 are presented in Fig. 52. Notice in Fig.

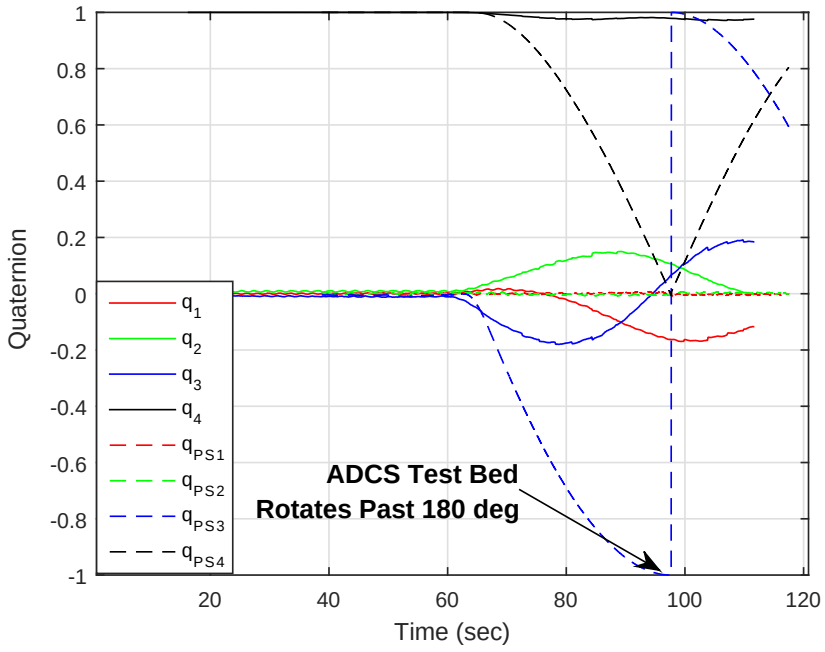


**Figure 52. External Magnetometer $\omega_k = 0.5$ QUEST Test 2**

52 that the quaternion from the ADCS test bed again shows erroneous results. Also note that the PhaseSpace truth data shows the ADCS test bed rotated past 180° while the ADCS test bed calculated erroneous quaternions similar to Test 1. The results of increasing the magnetic field strength to [0,2000,0] mG and resetting the second

magnetometer weighting to one for Test 3 are shown in Fig. 53. Fig. 53 shows

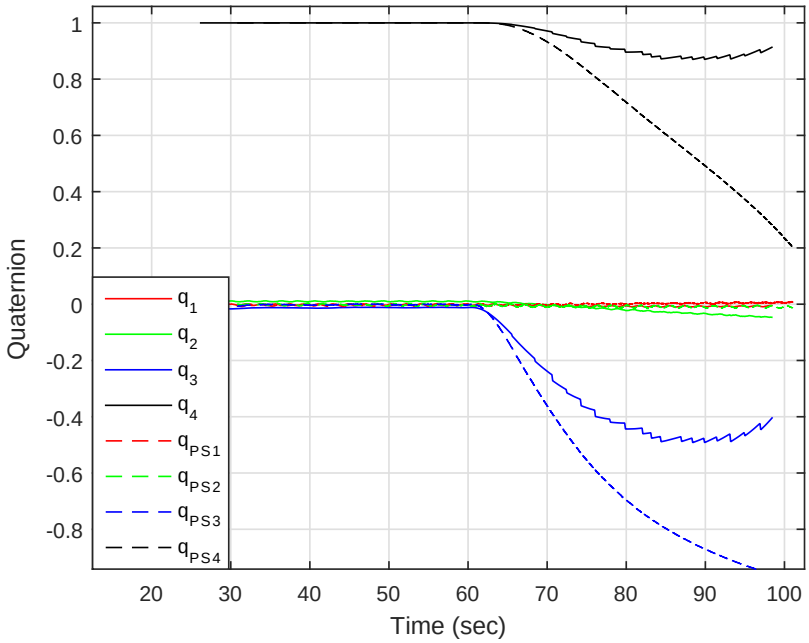


**Figure 53. External Magnetometer $\omega_k = 1$ QUEST Test 3**

that increasing the Helmholtz cage to the maximum setting of [0,2000,0] mG the quaternion estimate from QUEST shows improvement over the results found during Test 1 and Test 2 in an ambient Earth magnetic field. Although the quaternion from the ADCS test bed in Fig. 53 appears to reverse back towards the original orientation of $[0,0,0,1]^T$, the data from the truth source shows the opposite is true. During test 3 the ADCS test bed continued to rotation past the 180° position and demonstrated no control over its orientation. The results of lowering the secondary magnetometers weighting in QUEST to 0.5 in Test 4 are presented in Fig. 54. Notice in Fig. 54. the ADCS test bed calculations are showing the QUEST quaternion to be in the vicinity of the commanded quaternion $[0,0,-0.7071,0.7071]^T$. However, no control was exhibited as shown by the truth data from the PhaseSpace system. Lowering the weighting of the external magnetometer in QUEST to 0.1 during Test 5 allowed the ADCS test bed to achieved control in the vicinity of the commanded orientation. Unfortunately

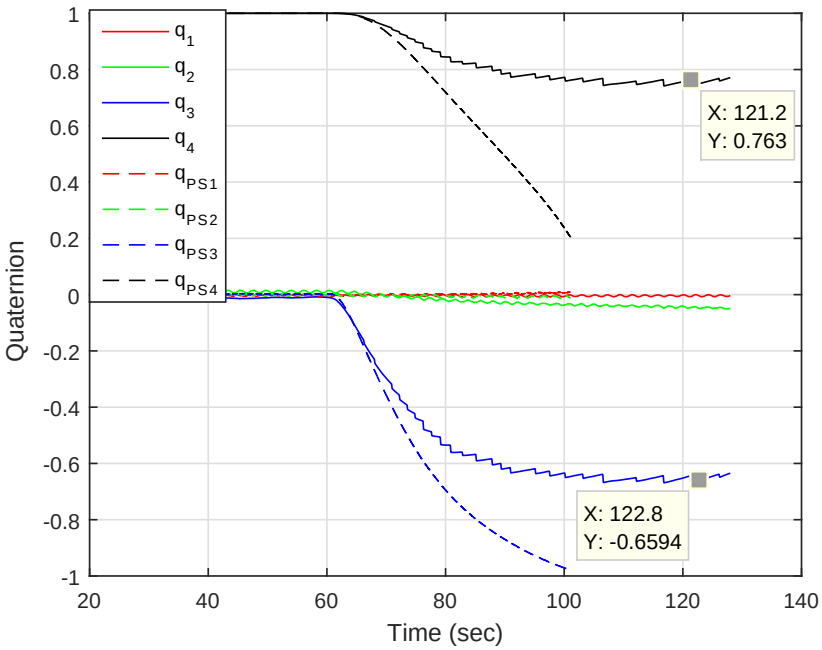


**Figure 54. External Magnetometer $\omega_k = 0.5$ QUEST Test 4**

Tera Term lost connection with the ADCS test bed Wi-Fly 74.3 seconds into the test. The results from Test 5 are shown in Fig. 55.

Note from Fig. 55 that the ADCS test bed telemetry data ends abruptly around 14 seconds into the maneuver. Notice also that the PhaseSpace data shows the $q_{PS3}$ and $q_{PS4}$ values stabilize approximately 95 seconds into the test. Converting the last few data points from the PhaseSpace quaternion back into Euler angles gives an orientation of -94.05°, which is different from the commanded orientation by 4.05°. This shows that reducing the weighting of the second magnetometer would improve accuracy. This means the sensor data from the secondary magnetometer measurement holds significantly less weight in the final quaternion estimate.

This section presented analysis and results that show the external magnetometer requires further biasing and calibration to achieve the ±1° of accuracy it should provide. Its use in QUEST showed significant degradation of the quaternion estimate. For this reason the external magnetometer measurements are not used in QUEST for

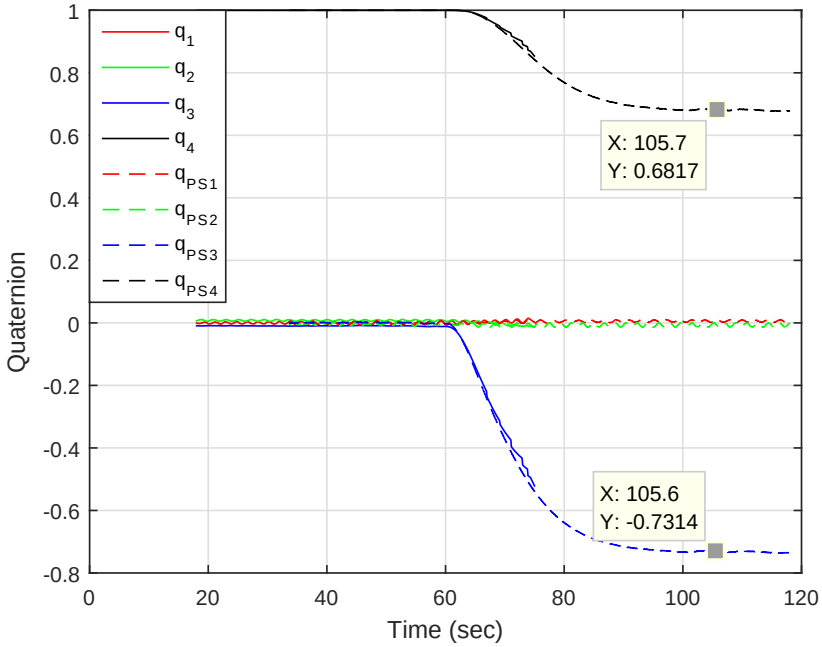


**Figure 55. External Magnetometer $\omega_k = 0.1$ QUEST Test 5**

further testing and are not presented in the analysis for the remainder of this chapter due to the undesirable affects on the quaternion estimate.

## 4.5 Singularity Analysis

As discussed in Chapter III the QUEST algorithm currently used on the ADCS test bed develops a singularity when a 180° rotation occurs around any axis. Recalling from Chapter II that the singularity develops in the Rodrigues parameters during the QUEST calculation at a rotation of $\pi$ radians. It is important to characterize the singularity for this research as it may cause undesirable control authority near the singularity. MATLAB is used to show a maneuver without a singularity. Fig. 56 presents a rotation of simulated spacecraft from $[0,0,0,1]^T$ to $[0,0,1,0]^T$.

Notice in Fig. 56 that after the 180° rotation the quaternions stay at the commanded values. The simulation however does not use the same method as the ADCS test bed. In the QUEST algorithm, the Rodrigues parameters are used in the de-

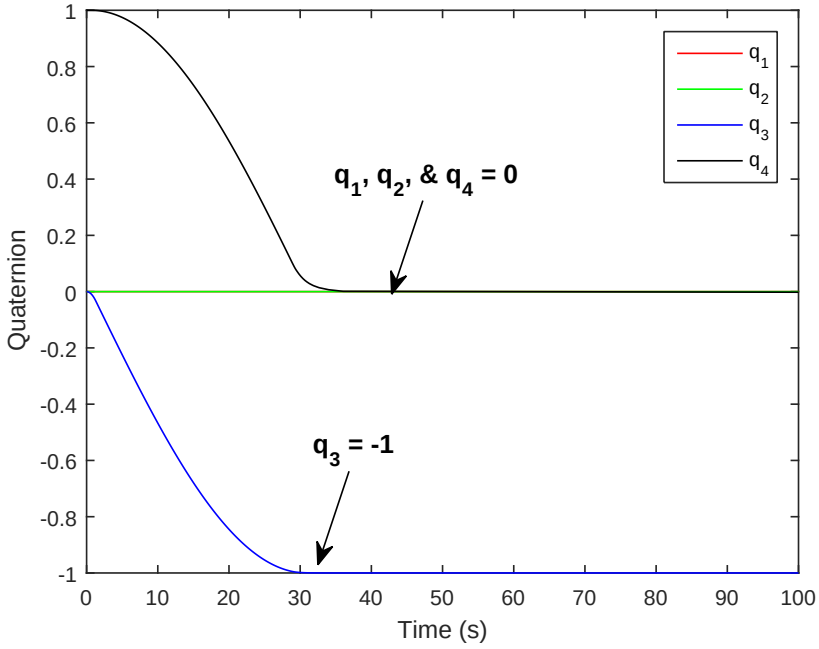


**Figure 56. Simulated Quaternions of 180° Slew**

nominator of Eq. (52) in Chapter II to obtain the current quaternion. The following subsections present the results discovered in this research.

### 4.5.1 Maneuvering to 170° Helmholtz Cage Off

To research the effects of the singularity on the QUEST algorithm it is first prudent to characterize the algorithm behavior in the vicinity close to the singularity. Table 8 in Chapter III shows the full test sequence, but is briefly repeated here. Test 1 is conducted in an ambient Earth magnetic field and is commanded to stay at the origin until sixty seconds. After sixty seconds the ADCS test bed is commanded a -90° rotation. After another sixty seconds it is commanded an another -80°, making the total rotation 170°. The quaternions from QUEST resulting from Test 1 are shown in Fig. 57 Notice in Fig. 57 that the PhaseSpace truth measurement $q_{PS4}$ begins a steep dive towards zero at approximately 150 seconds into the test. At the same time, the ADCS test bed QUEST estimate of $q_4$ begins to rapidly increase.

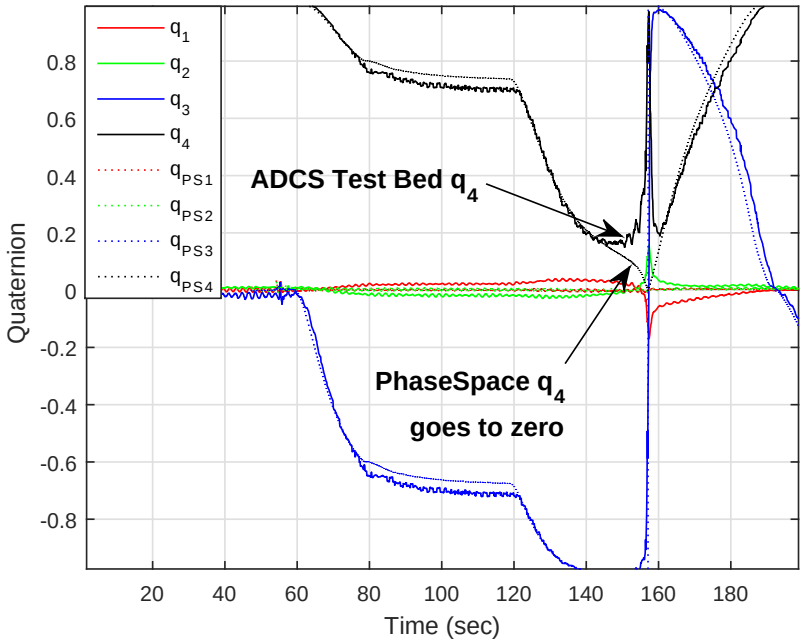


**Figure 57. Singularity Test 1 (Helmholtz Cage Off)**

The rapid decrease of the true $q_{PS4}$ is a result of the PID controller responding to an increase in the quaternion error as shown in Fig. 58. Notice in Fig. 58 that the quaternion error $q_{e3}$ at the -90° location is being driven to zero by the PID control law. Also note that at approximately 150 seconds the same $q_{e3}$ begins to increase rapidly. This rapid increase of $q_{e3}$ causes the PID controller to command larger wheel speeds as shown in Fig. 59, and as the singularity nears, the ADCS test bed continues to increase the commanded RPM. The singularity occurs at approximately 157.3 seconds into the test. After the singularity is passed, the quaternion estimate and error become more accurate and the PID control law unsuccessfully attempts to reverse its course by changing the output torque. The PID torque commands during the test and through the singularity are shown in Fig. 60 where you can see after the singularity is passed the torque command immediately spikes to -0.37 mNm. The ADCS test bed body passes the commanded orientation and completes a 360° maneuver, and the same process repeats continuing to increase the body rate

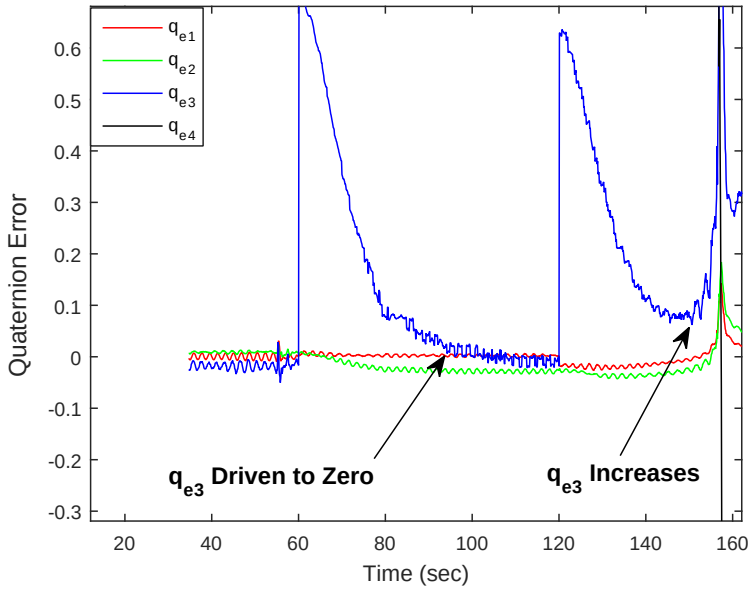


**Figure 58. Quaternion Error in Singularity Test 1**

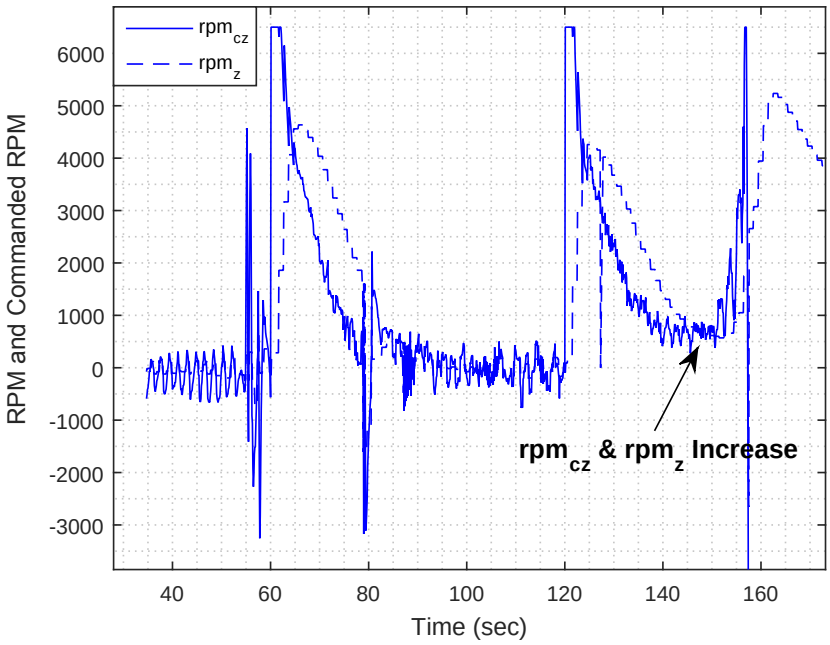


**Figure 59. RPM Response to Quaternion Error Test 1**

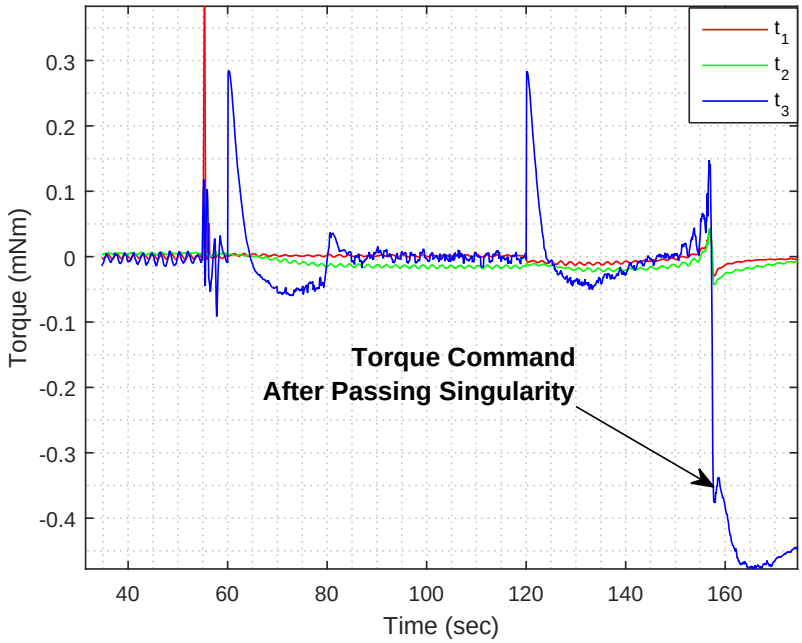


**Figure 60. Commanded Torque During Test 1**

until the RWA reaches saturation. The singularity is clearly problematic for the QUEST quaternion estimated in an ambient Earth magnetic field. Next, the effects of increasing the magnetic field strength are discussed.

### 4.5.2 Maneuvering to 170° [0,2000,0] mG

Increasing the magnetic field strength to [0,2000,0] mG clearly shows that QUEST is estimating an accurate quaternion. This is evident by comparing the truth data from PhaseSpace to the ADCS test bed quaternion estimate shown is Fig. 61. As Fig. 61 shows the two quaternion sets are identical and control at -170° is achieved at approximately 155 seconds into the test. Increasing the magnetic field strength clearly produces a better quaternion estimate from QUEST. This is also evident in the quaternion error as shown in Fig. 62. Notice that the quaternion error is much less than that shown in Fig. 58 during the ambient Earth magnetic field test. The quaternion error is the key input in to the PID control law as the RPM of the $z$-axis

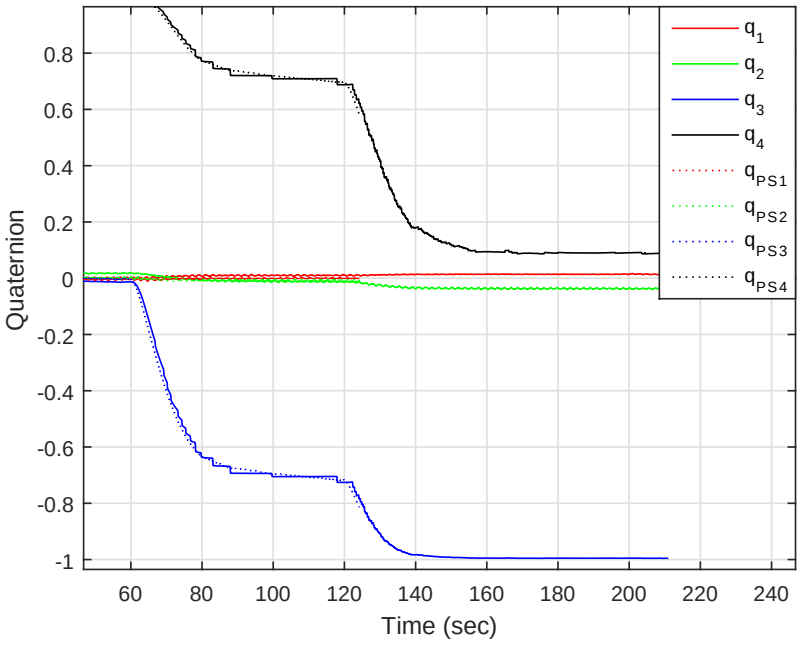


**Figure 61. Quaternions of 170° Slew**

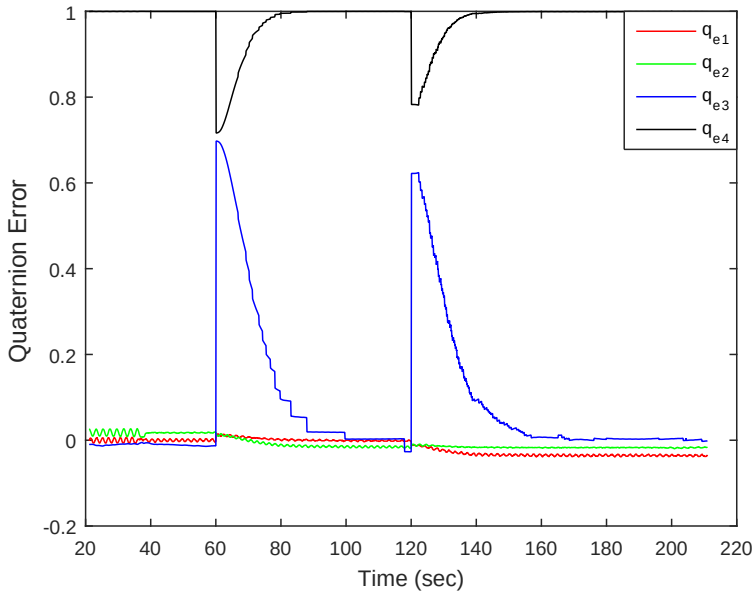


**Figure 62. Quaternion Error in Singularity Test 2**

wheel is more stable as shown in Fig. 63. Comparing Figs. 63 and 59, the RPM of

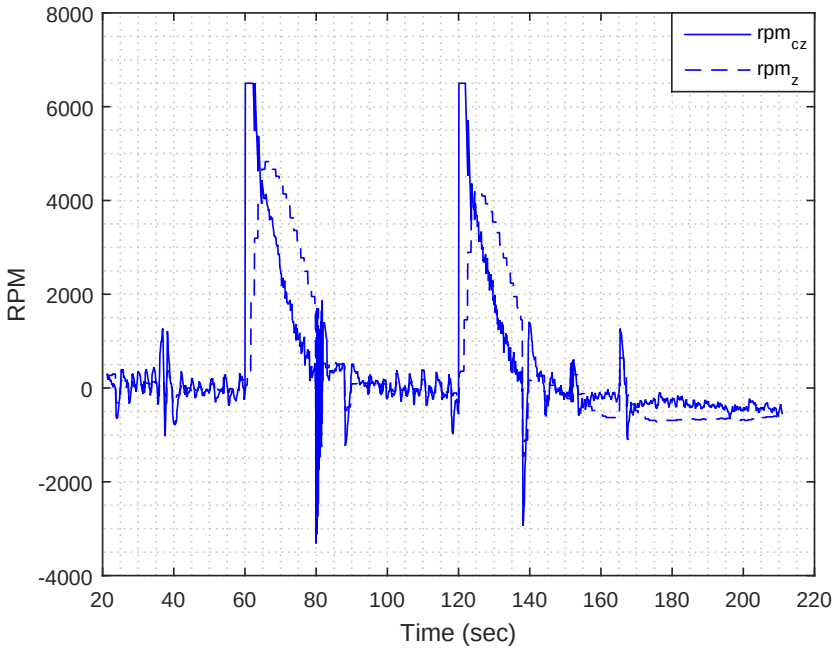


**Figure 63. RPM Response to Quaternion Error Test 2**

the $z$-axis wheel doesn't increase as the singularity near 180° is approached. This is also evident by inspecting the output torque of the PID controller in Fig. 64 where you can see the commanded torque does not spike down like that in Fig. 60 during the ambient magnetic field test. This is because the ADCS test bed does not pass through the singularity and maintains control at the commanded -170° orientation. Next the ADCS test bed is commanded to the singularity point at 180° along the $z$-axis.

### 4.5.3 Maneuvering to 180° [0,2000,0] mG

As noted in Table 8 of Chapter III, the ADCS test bed was commanded to -180° in an ambient Earth magnetic field with the Helmholtz cage off. The results are identical to those obtained in the -170° test and are not presented in this research. This subsection presents the results of commanding the ADCS test bed to the singu-

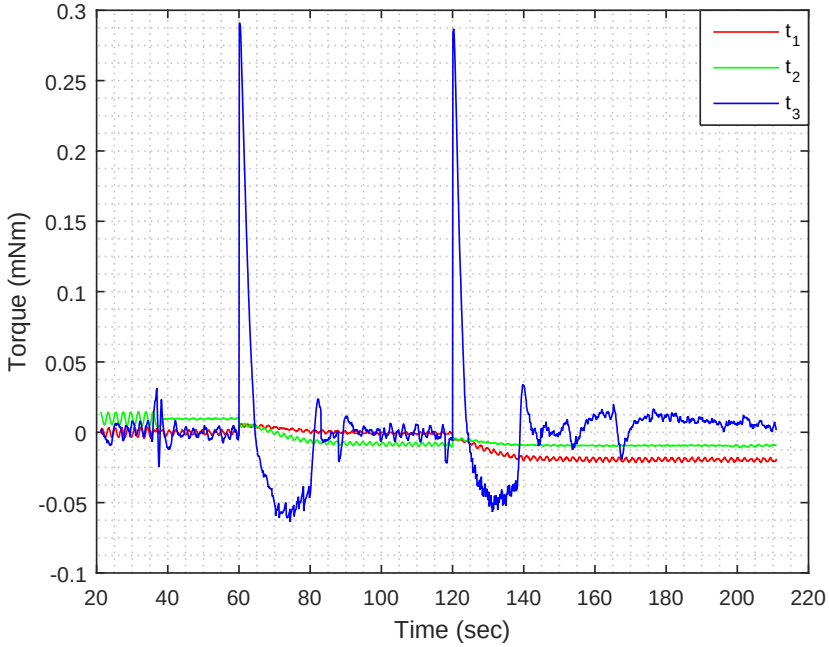


**Figure 64. Commanded Torque During Test 2**

larity point at 180° in the [0,2000,0] mG magnetic field. The quaternions from the PhaseSpace and the ADCS test bed for this test are shown in Fig. 65. Notice in Fig. 65 that the PhaseSpace quaternion $q_{PSi}$ and the ADCS test bed quaternion $q_i$ values are indistinguishable. This is again due to the significantly improved QUEST estimate in the artificially strong magnetic field created by the Helmholtz cage. However, during this test the ADCS test bed was observed to be "bouncing" around the commanded 180° orientation. Upon closer inspection of the RPM and the body rate estimate $\omega_z$ in the telemetry data it was confirmed that the ADCS test bed was oscillating about the 180° position. The RPM and body rates can be seen in Figs. 66 and 67, respectively. Notice in Fig. 66 that the RPM during the 90° orientation is more consistent than during the 180° orientation. Also note from Fig. 67 that the body rate about the $z$-axis at 180° is constantly crossing zero. This means that the singularity is still affecting the control authority of the ADCS test bed at exactly 180°. This testing shows that the increased magnetic field allows the QUEST

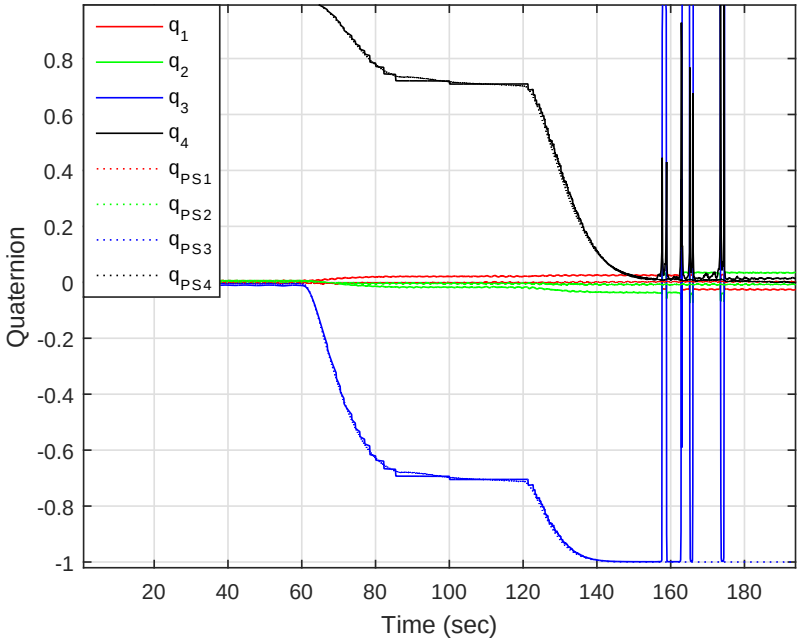


**Figure 65. Quaternions During Singularity Test 3**

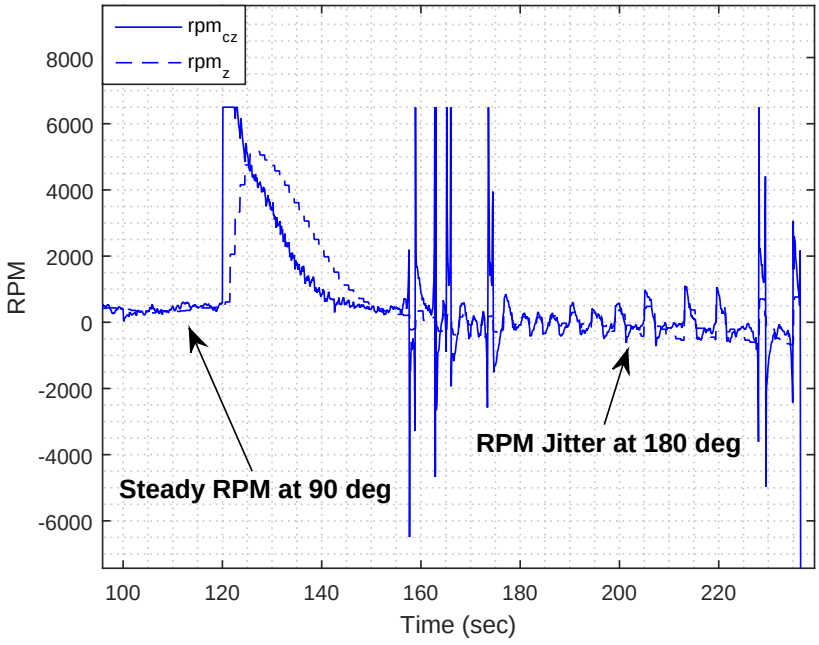


**Figure 66. RPM Commands at the Singularity**

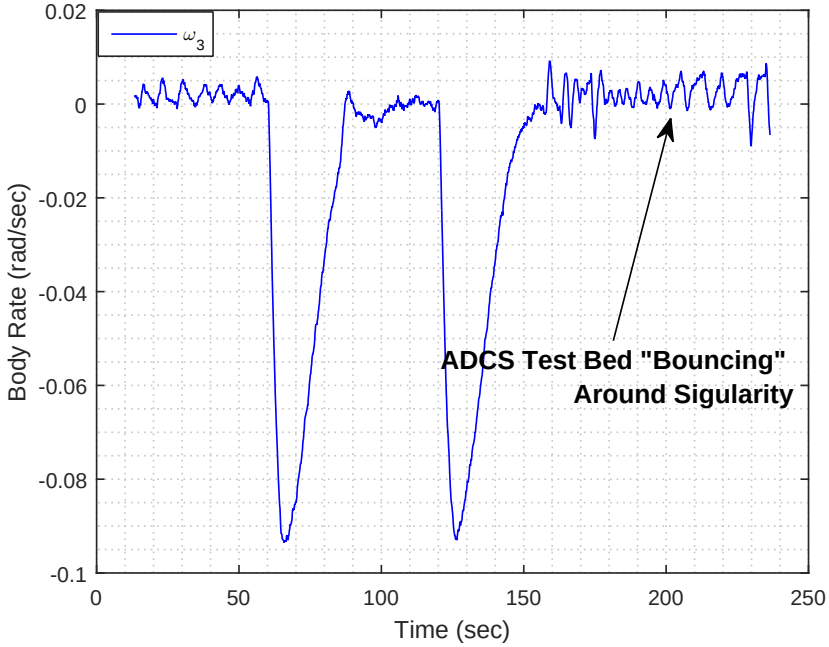


**Figure 67. ADCS Test Bed Body Rate at Singularity**

estimate to provide a significantly improved quaternion value. From this improved quaternion and quaternion error, the PID control authority in the proximity of the singularity is greatly increased. Since control was achieved around the singularity the next subsection presents the results of the four corner 360° rotation test.

### 4.5.4 Results of the Four Corner 360° Rotation Maneuver

As noted in the research objectives section of Chapter I, a primary research goal was to evaluate a 360° controlled rotation about the $z$-axis through four rotations of the ADCS test bed. The timing and commands given are shown in Table 9 of Chapter III. Fig. 68 presents the quaternions of the ADCS test bed and the PhaseSpace system during the 360° rotation in a [0,2000,0] mG field.

Notice in the Fig. 68 that the ADCS test bed quaternions matched those from the PhaseSpace system until the -270° rotation. Despite the error, the ACDS test bed was able to control to the vicinity of the commanded quaternion $[0,0,0.7071,0.7071]^T$.

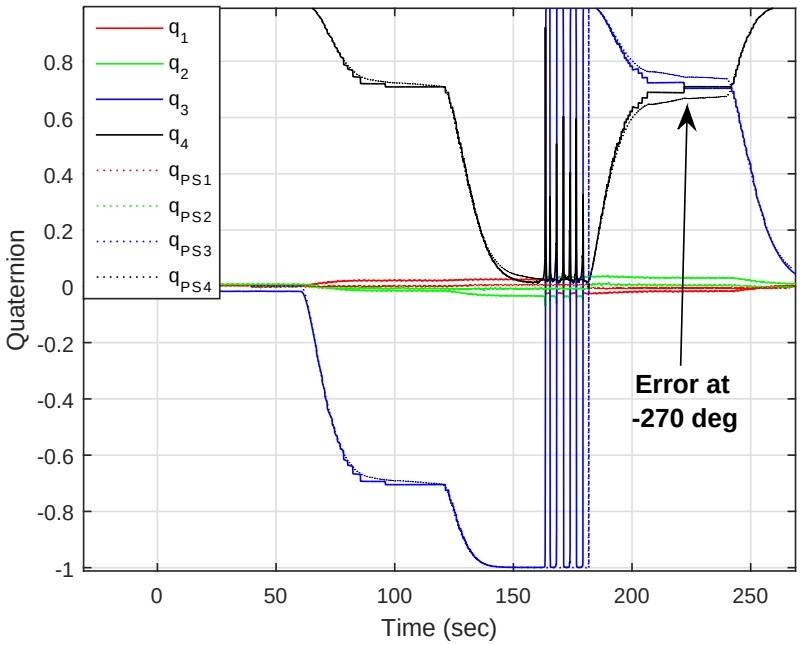


**Figure 68. Quaternions During Four Corner 260° Rotation**

This error will be characterized later in the chapter. The plot of the commanded torque from the PID controller is shown Fig. 69.

Notice that approximately 160 seconds into the test the torque oscillates the most while the ADCS test bed is commanded to the singularity. Even with the Helmholtz cage setting at [0,2000,0] mG the effects from the singularity cannot be negated as it is a mathematical problem that develops from the Rodrigues parameters in QUEST. Fig. 70 presents the Rodrigues parameters as calculated by QUEST during the four corner 360° rotation. Notice in Fig. 70 that the Rodrigues parameters are rather steady with values between negative one and one until after the 180° maneuver command is initiated. Around the singularity the $p_3$ term rapidly decreases until it passes the singularity then rapidly increases. Note that Fig. 70 shows that the ADCS test bed appears to have crossed the 180° position seven times based on $p_3$ term before the next maneuver was commanded at 180 seconds into the test.

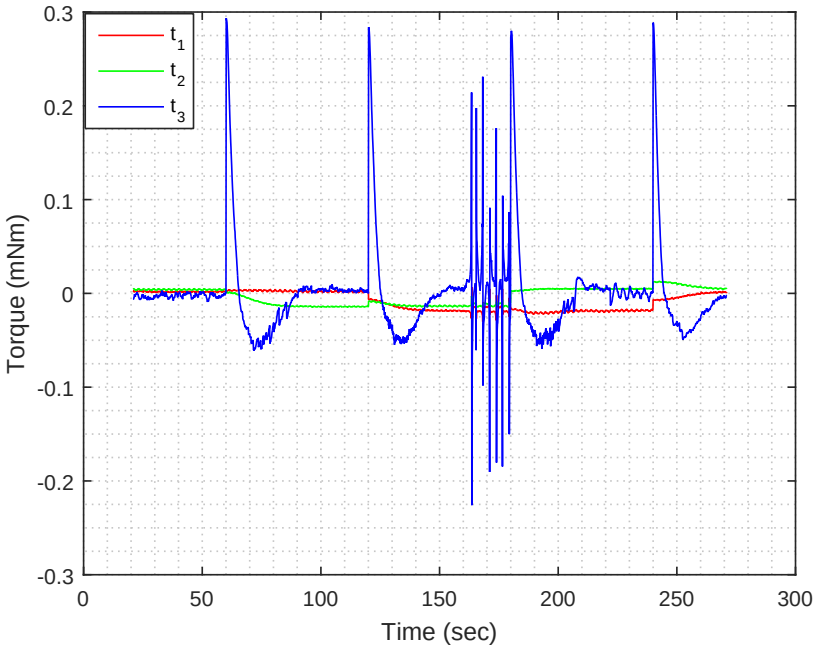


**Figure 69. Commanded Torque During 360° Rotation**

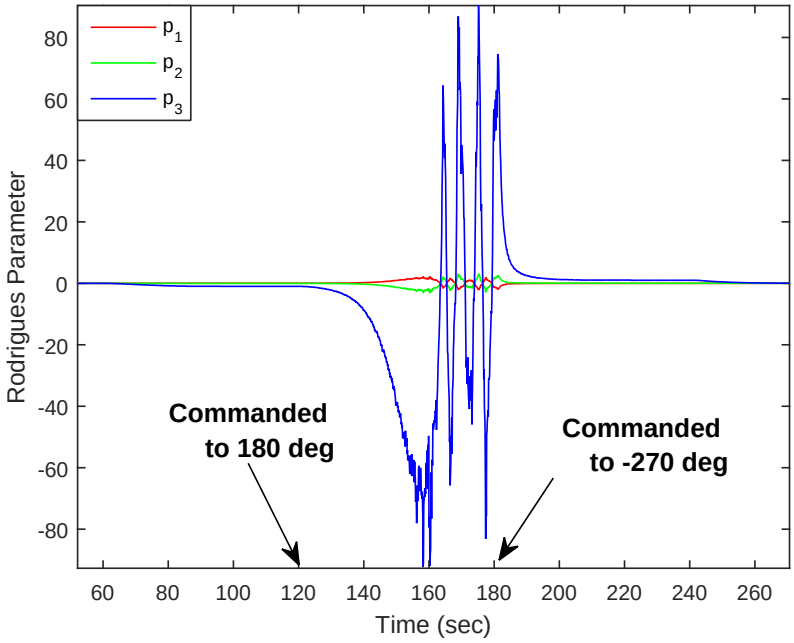


**Figure 70. Rodrigues Parameters During 360° Rotation**

## 4.6 Estimation and Control Accuracy Analysis

As presented earlier in the chapter, changing the magnetic field strength with the Helmholtz cage has affected the ADCS test bed QUEST result. This section presents the QUEST estimated quaternion accuracy as compared to the external PhaseSpace system truth data. As noted in the beginning of the chapter the quaternions will eventually be converted into Euler angles for easier comparison. The section begins with a body rate estimation analysis to compare the $\omega_i$ values with the body rate estimate $\omega_{i-est}$ calculated using the ADCS test bed quaternion. To aid in presenting the data, only the $z$-axis Euler angle and the $q_3$ and $q_4$ terms will be shown. This is based on the fact that only the $z$-axis of the ADCS test bed was fully controllable. The $x$-axis showed notable deviations in the wheel speed control authority testing section and the moment caused from the displacement of the CoR and the Com limited functional control of the $y$-axis. Furthermore the rotations are in the negative direction, but the Euler angle presented will be made positive to help display the data.

### 4.6.1 Body Rate Estimation Using Quaternions

It should be noted that this subsection is primarily included to help future research develop a method to obtain a "truth source" body rate estimate from the quaternion in the PhaseSpace system. As Chapter III discussed, the equations provided by [18] offer an excellent way to estimate the body rate of a spacecraft using only the quaternion. This research used the body rate estimate $\omega_{i-est}$ in the PID control law instead of the $\omega_i$ values created by Tibbs [4]. It was discovered early in the research that even though these values are calculated differently, they still produces the exact same result as shown in Fig. 71. The values in Fig. 71 are the same because the body rate estimate $\omega_{i-est}$ from the quaternions relies on the $\dot{\mathbf{q}}$ term from Eq. (33) in

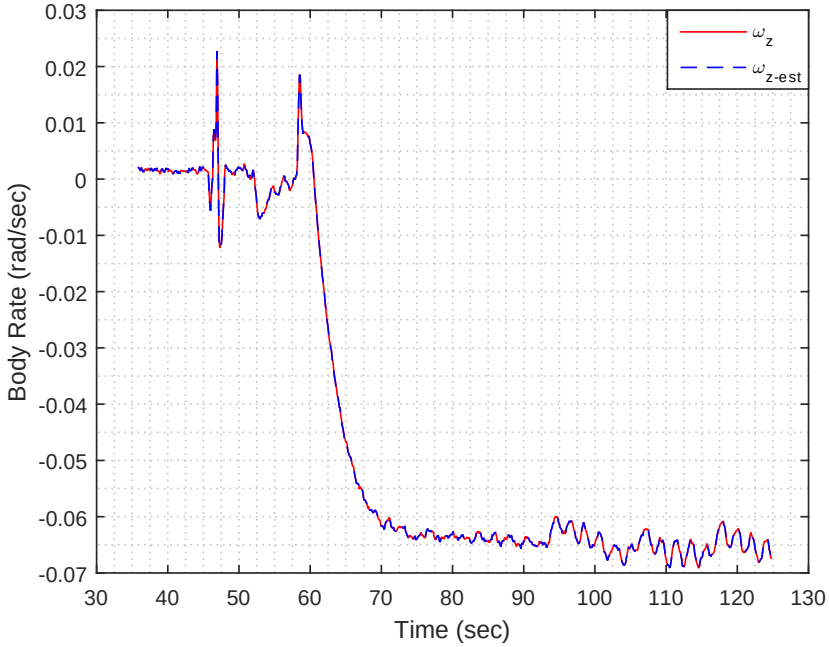


**Figure 71. Body Rate Estimate vs. ADCS Test Bed $\omega_z$**

Chapter II. These values could not be compared to the PhaseSpace system because the current API is not programmed to calculate or produce the true body rate from the Owl Server. The equations presented in Chapter III and the results discovered in this research will be helpful for future development of the PhaseSpace API and are presented here only to be discussed in Chapter V.

### 4.6.2 ADCS Test Bed Performance in Variable Magnetic Fields

This subsection presents the performance results from the ADCS test bed and the PhaseSpace system data collection. In order to make the quaternion difference between the two systems more straightforward to the reader, they will be presented as Euler angles. The angle error is simply the ADCS test bed angle subtracted from the PhaseSpace truth source measurement. Note that the angle has been made positive to better display the data. The results from the 90° rotation with the Helmholtz cage off are shown in Fig. 72. Note in Fig. 72 the angle error before the maneuver is

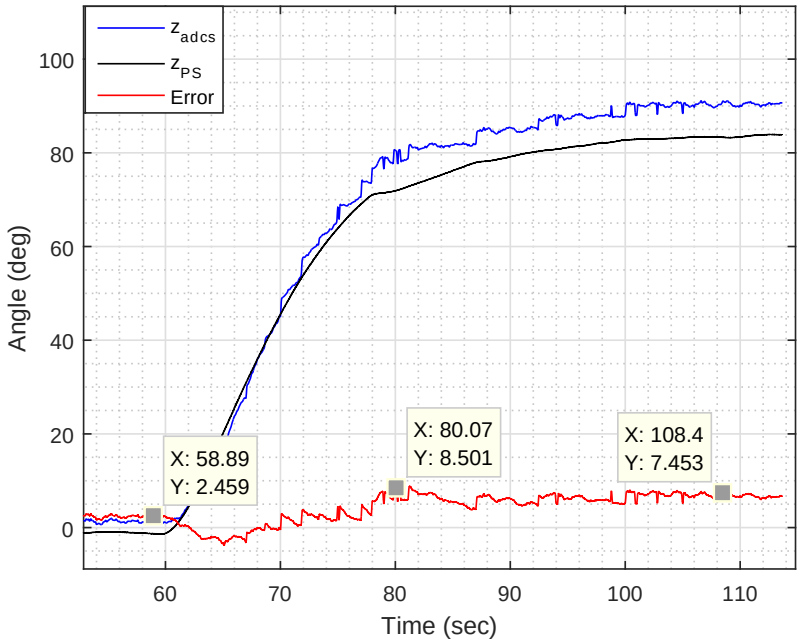


**Figure 72. Angle Error During 90° Rotation-Helmholtz Cage Off**

approximately 2.5° before the maneuver. This error is due to the slight misalignment with the PhaseSpace camera frame and the physical ADCS test bed and will be discussed further in the error analysis section. Also notice from Fig. 72 that the maximum error of approximately 8.5° occurs about eighty seconds into the maneuver. After the ADCS test bed reaches steady state the angle error remains in the vicinity of 7.5°.

The next test shown utilizes the Helmholtz cage at its maximum field strength setting of [0,2000,0] mG. The results of the 90° rotation are shown in Fig. 73. Notice in Fig. 73 the error prior to the maneuver at sixty seconds is approximately 0.17°. During the maneuver the largest angle error detected was 2.5° at approximately ninety seconds into the test. Once steady state control was achieved at the 90° orientation the angle error decreased to 1.4°. The difference in error between the test with the Helmholtz cage off and at [0,2000,0] mG is due to the accuracy of the QUEST estimate. The stronger magnetic field clearly produces a better quaternion which

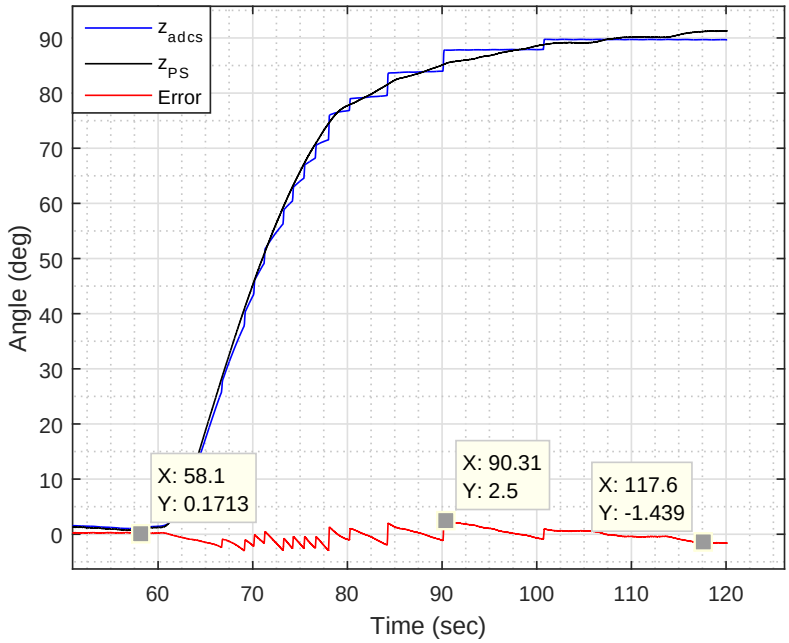


**Figure 73. Angle Error During 90° Rotation [0,2000,0] mG**

allows the ADCS test bed to perform more accurately. The results of the 90° rotation in a [0,471,0] mG field are shown in Fig. 74. Notice in Fig. 74 that a maximum error of 4.6° occurs at approximately seventy seconds into the test. The angle error during steady state was found to be approximately 1.3° as noted in Fig. 74. Notice also that the ADCS test bed angle and the PhaseSpace truth angle appear to converge in Fig. 74. This was an unexpected result during the research as the stronger [0,2000,0] mG was expected to produce better accuracy. This implies that the Analog Devices primary magnetometer is better calibrated for near Earth ambient conditions. After reviewing the Analog Devices magnetometer specifications [39], it was discovered that each axis of the magnetometer have individual tolerances and calibration methods. Using the [0,471,0] mG Helmholtz cage is an unrealistic measurement as no magnetic field will be perfectly uniform on orbit. This topic is left for future research in Chapter V.

Reducing the magnetic field down to [100,100,100] mG provides an overall mag-

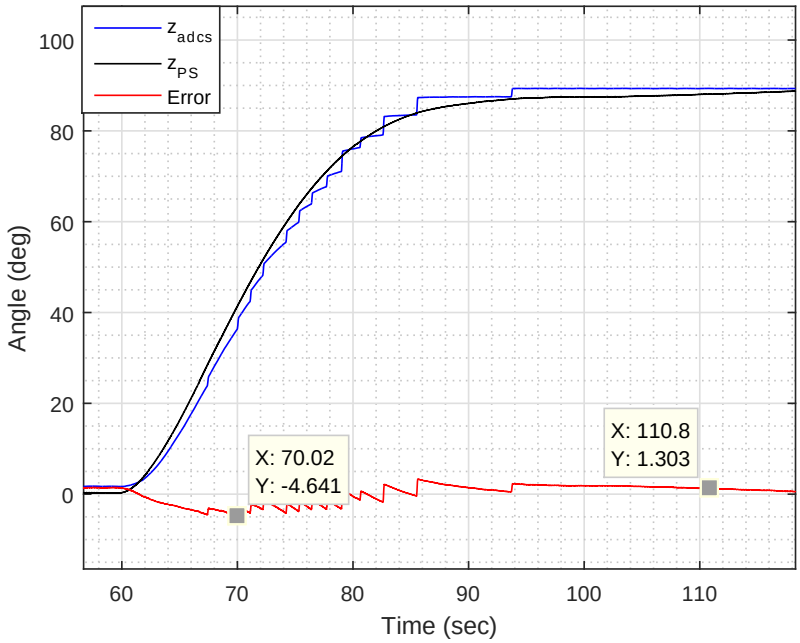


**Figure 74. Angle Error During 90° Rotation [0,471,0] mG**

nitude $B$ of 173.2 mG. The results from the 90° rotation in the reduced magnetic field are shown in Fig. 75 where you can see that a maximum error of 8.9° occurs approximately 76 seconds into the test. Notice also, that the steady state error after the maneuver is approximately 7.8°. The increase in angle error at reduced magnetic field strengths was expected during the research. Reducing the Helmholtz cage to [50,50,50] mG provides a magnitude $B$ of 86.6 mG which is the lowest strength magnetic field tested in the research. The results of the lowest magnetic field strength test are shown in Fig. 76 where you can see that the angle error stabilizes approximately 100 seconds into the test at approximately 13°. Note that control is still achieved, but the angle error is increased compared to the previous tests. This means the accuracy of the QUEST quaternion is being severely degraded as the magnetic field strength is decreased. The last performance test is the 360° rotation to investigate the accuracy of the attitude estimation along the entire $z$-axis in a [0,2000,0] mG field and is shown in Fig. 77. Notice that at approximately 160 seconds into the test the angle error

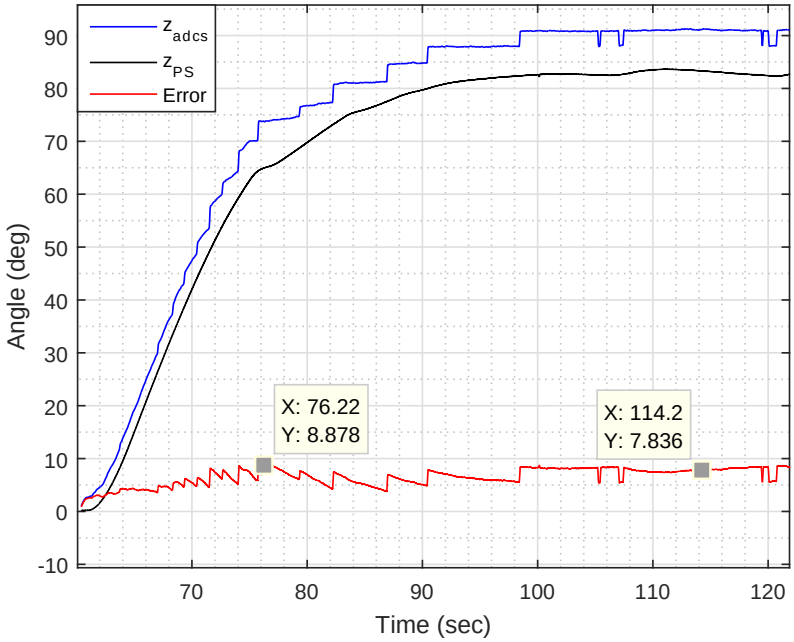


**Figure 75. Angle Error During 90° Rotation [100,100,100] mG**

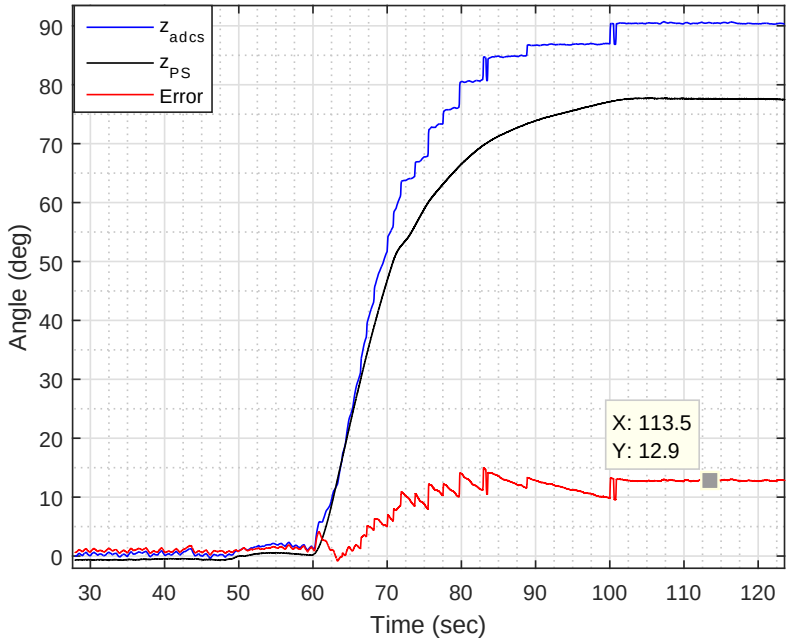


**Figure 76. Angle Error During 90° Rotation [50,50,50] mG**

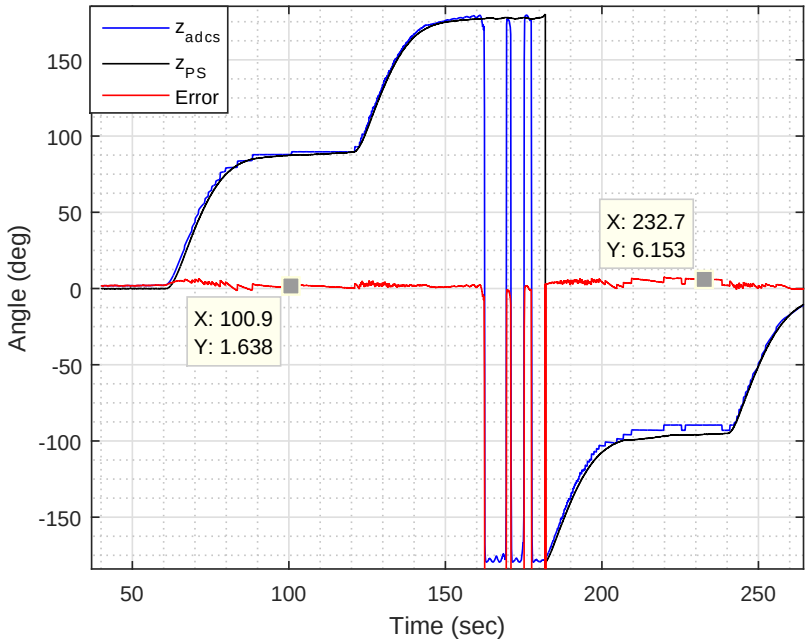


**Figure 77. Angle Error During 360° Rotation**

cannot be computed while the ADCS test bed is in the vicinity of the singularity at 180°. For the majority of the test the angle error is approximately ±2°, however as noted in subsection 4.5.4 there was significant error while commanded to the -270° orientation. The angle error in this orientation is approximately 6°.

## 4.7 Error Analysis

When using any external truth source it is important to investigate potential sources of error not considered in the results given. This section focuses on known errors in the PhaseSpace and ADCS test bed configuration. Furthermore, it was also discovered after the dynamic testing was completed that external environmental conditions may have had an influence on the results documented in this research.

### 4.7.1 PhaseSpace System Accuracy

The PhaseSpace system provides truth measurements for the position of the LED trackers to a sub-millimeter accuracy [41]. However, it does use a filtering process to best estimate the position of the LED trackers. From this estimation a singularity free quaternion is estimated based on the alignment of the user defined camera frame and rigid body editor. The use of the PhaseSpace system in this research assumes it is a black box recording the "true" quaternion. The error presents itself if the ADCS test bed is not exactly aligned with the rigid body defined frame in the Master Client software. Throughout this research the ADCS test bed was balanced and initialized to point at the 0° angle marker on the wall. During data reduction and analysis it became apparent that the air bearing is not entirely centered within the camera frame defined during the PhaseSpace calibration and alignment process. This error can be seen in many of the figures showing both the $q_3$ and $z_3$ variables prior to the sixty second maneuver time. The error is very consistent and was found to be approximately $\pm 2°$.

### 4.7.2 Solar Flare Induced Geomagnetic Effects

On 17 April 2016 a magnitude 6.7 solar flare was recorded by the Solar Dynamics Observatory [5]. Data from the NASA Advanced Composition Explorer (ACE) satellite is shown in Fig. 78,

where you can see that the flare was first detected on 18 April and appears to have lasted to the 21st of April 2016. The location of ACE is at the L1 liberation point between the Earth and the Sun, about 1,500,000 km forward of Earth. Its important to note that many of the documented results in this research were recorded 19 April to 23 April 2016. Although not presented in this research, the four corner 360° rotation test was conducted in an ambient Earth magnetic field on 22 April

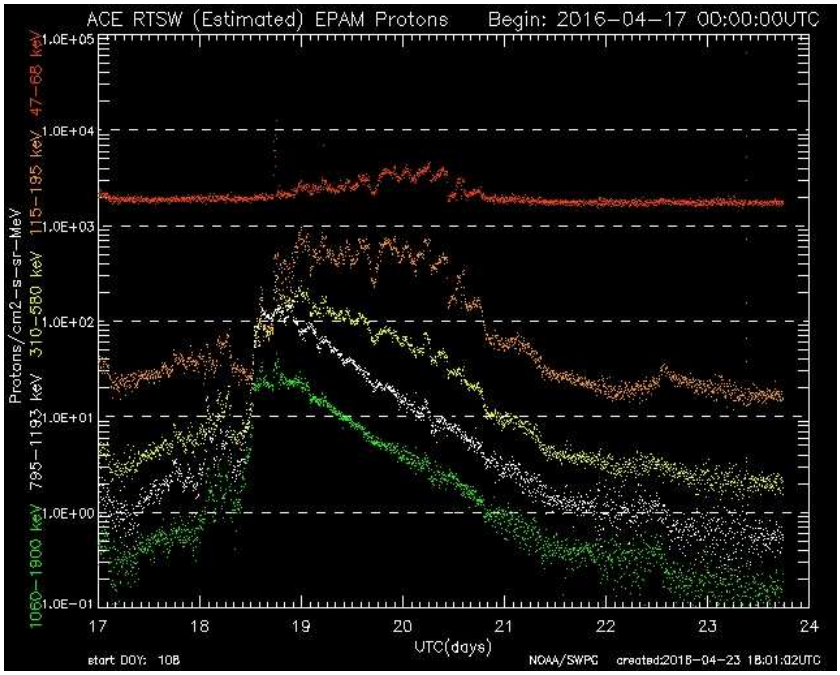


**Figure 78. ACE Detection of Solar Flare [5]**

2016. Active control was obtained around 180° for the first and only time during the research. Oscillations around the singularity were visually noted by the author and other observers. The test was repeated again on 26 April 2016 and control was not achieved at 180°. The result of these two test were not presented in the previous sections as the ground station truth magnetometer data was not recorded in real time during the tests. However, data was collected from the Analog Devices IMU primary magnetometer. The magnitude $B_1$ from both test dates during the four corner 360° maneuver are shown in Fig. 79.

Note in Fig. 79 that at sixty seconds the magnitudes of both data sets track fairly well. Note also that at 120 seconds into the test the ADCS test bed was commanded to the 180° orientation and the $B_1$ values differ slightly by approximately 4 mG. At 120 seconds the 180° maneuver is commanded. Notice the $B_1$ values are quite different from the two data sets. Also notice that during the 21 April test the $B_1$ leveled off during control around the singularity point at 180°. The 26 April test

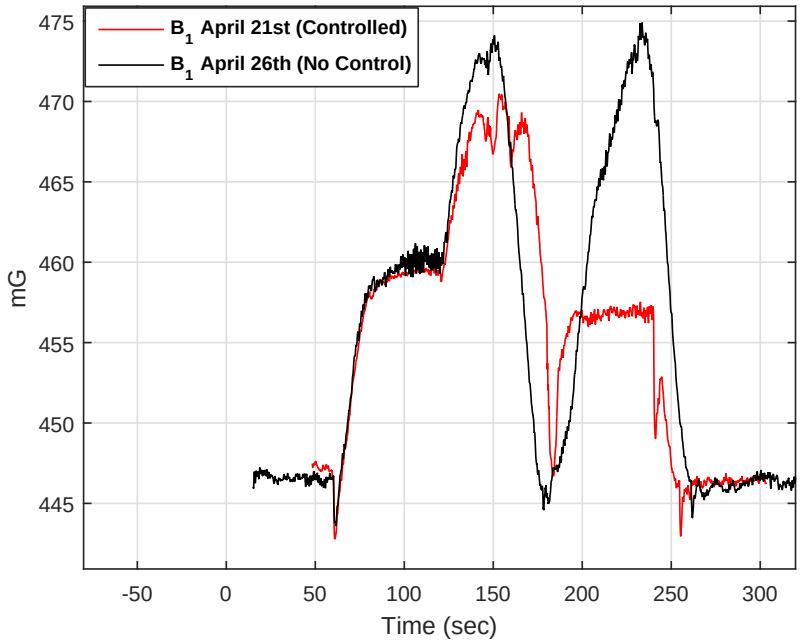


**Figure 79.** $B_1$ **Plot Before and After Solar Activity 360° Rotation**

behaved identical to the results presented in section 4.5.1 during the 170° maneuver with the Helmholtz cage off. For this reason is important to note that some of the error and accuracy during this research may have been influenced by the solar flare on 17 April 2016.

## 4.8 Chapter Summary

Chapted IV presented the results and analysis of the testing documented in section 3.4. The first section described how the data would be corrected for corrupted data points and how the MATLAB *interp1* function will be employed to interpolate data. The second section documented the model simulation results compared to the ADCS test bed performing a -90° rotation in a [0,2000,0] mG field. The third section presented the wheel speed control authority testing performed and highlighted the code variable mismatch issues experienced. The chapter continued by characterizing the magnetometers in five magnetic field strengths. The secondary external

magnetometer data performed comparable to the Analog Devices magnetometer only in the ambient Earth magnetic field during static testing. The Kalman filter was found to induce a 3 second delay into the magnetometer sensor data. Next, the external magnetometer data was used in QUEST with different sensor weighting. The quaternion estimate was found to degrade the output from QUEST and the external magnetometer was removed. The following section characterizes the ADCS test bed in the proximity of the singularity point at 180°. Control near the singularity point in an ambient Earth magnetic field could not be achieved due to the quaternion error increase. The ADCS test bed was found to be controllable around the singularity in a [0,2000,0] mG field as the quaternion estimate from QUEST was improved. The following section presents the estimation and control accuracy of the ADCS test bed in various magnetic fields. It was discovered that the magnetic field setting of [50,50,50] mG induced an angle error of 12.5° during a -90° rotation. The strongest magnetic field setting of [0,2000,0] mG allowed the ADCS test bed to control to 1.5°. Finally the last section documented sources of error in the research. The errors include the misalignment of the PhaseSpace software coordinate system with the physical ADCS test bed and the observed solar flare during the week of testing which may have altered the test results.

# V. Conclusions and Future Work

## 5.1 Summary of Research

The primary goal of this research was to characterize the ADCS test bed and use an external truth source to verify its control authority and estimation accuracy in typical magnetic field strengths on orbit. A secondary objective as discussed in Chapter I was to perform a controlled 360° rotation through four 90° rotations. To achieve the primary objectives, it was necessary to remove external sensor noise that would degrade the sensor measurements of the magnetometer. To investigate if the quaternion estimate could be improved a secondary external magnetometer was installed. A three wheel RWA was constructed and positioned away from both the primary and secondary external magnetometers to mitigate EMI. A quaternion error based PID controller was implemented using control gains based on the desired response. Static testing was performed to ensure EMI effects were removed from the magnetometers and verify the ADCS had adequate RWA speed control authority. It was discovered that the C code variable type mismatches in the main ADCS test bed algorithm caused OS noise which was shown to degrade the RPM command from the ADCS control card. Dynamic tests were performed atop an air bearing using a Helmoltz cage providing variable magnetic fields during each test. A PhaseSpace Impulse X2E motion capture system was installed and calibrated to record truth source data during the dynamic test. Data was collected from the ADCS test bed and compared to the external truth data.

The AFIT CubeSat test bed ground station, including physical properties and modifications of the 6U CubeSat used in this research, are discussed. A prototype ADCS test bed was documented that helped in experimental modifications and software development throughout the research. An attempt to manage the displacement

of the center of mass and the center of rotation of the air bearing is presented as it was determined that the CubeSat test bed would not have $x$- or $y$-axes control based on the stability requirements of the air bearing during dynamic tests. The final placement of CubeSat test bed allowed for installation of the PhaseSpace system LEDs and battery pack later in the research. The final ADCS test bed's MOI was measured and estimated then used to define the PID controllers gain settings. The ADCS test bed software including an overview of the control algorithm is presented followed by a discussion of the PhaseSpace system's hardware and software. The physical configuration of the final ADCS test bed was balanced and assigned a coordinate system in the PhaseSpace software to compare data. The data collection process through the use of Tera Term and the Owl Server are introduced. Finally, static and dynamic test procedures are discussed to verify the performance of the ADCS test bed.

The static and dynamic tests performed in the AFIT ADCS test bed utilized five different magnetic field settings, four of which used the Helmholtz cage. After initially discovering a quaternion error issue in the C code, the ADCS test bed was commanded through a series of rotations to capture performance data and compared to the PhaseSpace truth source. It was discovered that the second external magnetometer would require extensive biasing and calibration to be used in the ambient Earth magnetic field and performed poorly while using the Helmholtz cage under other magnetic field settings. The Kalman filter developed proved to operate to slow to be used in the attitude determination algorithm. The displacement of the RWA proved to mitigate much of the EMI experienced by the primary magnetometer in past research. The second magnetometer sensor measurement was assigned various weights in QUEST and the performance of the ADCS test bed was compared to the external PhaseSpace truth source.

At the lowest weighting value of 0.1 for second magnetometer in QUEST the

ADCS test bed began to show active control. The ADCS test bed quaternion estimate also began to match the PhaseSpace truth data. This highlights the importance of the sensor measurement weights in QUEST. Although only three sensors could be used in this research with the limited QUEST algorithm currently installed, it shows that any corrupted sensor data can significantly affect the quaternion estimate of a spacecraft. Ways to mitigate corrupted data could be implemented to lower the weighting automatically if EMI or noise can be detected. The singularity condition in this version of QUEST may not present a problem for some satellites, but CubeSats are susceptible as they typically deploy as secondary payloads. Deployment into an unknown orientation could cause the singularity condition to inhibit the mission performance if steps are not taken to mitigate its affects. One possible solution would be to command the spacecraft to a 90° rotation and reset the current quaternion to $[0,0,0,1]^T$ at the new orientation. This would effectively move the singularity 90° from the previous orientation. However, a better option would be to implement the modified Rodrigues parameters which provide a singularity free solution. As Chapter IV presents the Rodrigues parameters currently used in QUEST are erroneous in the vicinity of the singularity. Control near the singularity in an ambient magnetic field was only obtained once during the research and happened to occur during a solar flare event. This highlights that the current QUEST algorithm along with the current sensor measurements used on the ADCS test bed would benefit from the addition of a third vector measurement.

The increase of the magnitude $B_2$ from the second magnetometer during the ambient Earth magnetic field during dynamic testing was shown to be 68.4 mG which was five times higher than the change from the primary magnetometer $B_1$. It was determined that the second external magnetometer provided inconsistent results and was removed from QUEST before final performance testing was conducted. During

the simulated 500 km orbit magnetic field of [0,471,0] mG the ADCS test bed attitude estimate compared to the PhaseSpace was only 1.3° in error. As Chapter IV presents this was an unexpected discovery as in the 6 dB higher magnetic field test of [0,2000,0] mG the ADCS test bed showed an error of 1.4° compared with the PhaseSpace system during the same 90° rotation. This shows that the axis the magnetometer uses to collect sensor data may affect the attitude estimation. The primary magnetometer does have different tolerances and calibration requirements for each axis. It is the author's recommendation that the test be repeated with a magnetic field of [471,0,0] mG and [2000,0,0] mG in an effort to research the extent to which the magnetometer chip is biased along each axis.

As hypothesized in Chapter I, lowering the magnetic field strength degraded the ADCS test bed attitude estimation. This is evident in Chapter IV during the ambient Earth testing and the lower [100,100,100] mG and [50,50,50] mG tests. When compared to the PhaseSpace truth data the angle error increased from 7.5°, to 7.8°, and finally to 12.9° with each lower magnetic magnitude setting of the Helmholtz cage. This is caused by the increased error in the attitude estimate calculated by QUEST on the ADCS test bed as shown in Chapter IV. This increase in attitude error affects how the PID control law computes torque commands and was shown to reduce control.

The 6° of error occurring at the 270° orientation during the four corner test in the [0,2000,0] mG magnetic field highlights the axis sensitivity of the primary magnetometer. This field strength is 6 dB higher than the ambient Earth magnetic field and shows similar error as presented during the 90° rotation test with the Helmholtz cage off. This implies that the overall orientation of the magnetometer in the test bed can affect the attitude estimate. Future research should consider using another Analog Devices IMU in a rotated orientation from the primary IMU. The new sensor

measurements would require rotation matrices to be programmed, but would help future research explore the limitations along each axis of the two magnetometers. Next, the limitations of this research are discussed that are unique to this research.

## 5.2 Limitations and Applicability of Research

This research effort began by mitigating known issues in the ADCS test bed hardware. The EMI issues from the RWA were confronted first which later led the research into troubleshooting the ADCS C code to properly control the newly modified hardware. The quaternion error calculations in the code were found to have sign errors which were corrected after an extensive review of the equations found in Chapter II. The previously used primary magnetometer bias had to be modified to allow operation in other magnetic field strengths.

Many of the problems were solved through trial and error and are unique to the specific ADCS setup at AFIT. The current hardware and software code was customized solely for this research project. It should be noted that although the on board magnetometers didn't experience EMI from the RWA, EMI will likely have to be managed in future 1U ADCS designs. As designed and built the RWA used will not survive a space qualification vibration test and was constructed by hand using two previous AFIT RWAs.

Utilizing a secondary $\mu$controller to handle the Hall sensor interrupt commands on the RWA has potential implications in many other areas, specifically data management. The effects of OS noise should be investigated on any system that relies on interrupt commands, cross link communications, and looped control algorithms. This research highlighted issues discovered through variable type assignment. Although variable type mismatches may not cause significant issues in many applications they can become an issue when computational resources are extremely limited and variable

type changes occur many times per second.

The PhaseSpace system used as the truth source provided excellent data to compare with the data collected from the ADCS test bed. However, it was discovered that the air bearing placement is not at the exact center of the PhaseSpace capture volume. This is evident in the error analysis section of Chapter IV as the angle error was $\pm 2^{\circ}$ before the maneuver started. The testing presented in this research initialized the ADCS test bed toward the $0^{\circ}$ mark on the wall adjoining the Helmholtz cage. The error was discovered when the rigid-body was assigned to the markerIDs in the PhaseSpace Master Client software while the test bed was statically pointing at $0^{\circ}$ on the wall. This discovery implies that the air bearing should be re-centered, the angle markings along the wall be adjusted, or reassignment of the PhaseSpace camera and rigid body coordinate systems.

## 5.3 Potential Future Work and Research Opportunities

The following subsections offer recommended future research opportunities utilizing AFIT's CubeSat test bed, ground station, and PhaseSpace truth source.

### 5.3.1 Ground Station Improvements and Data Collection GUI

With the addition of the external PhaseSpace system as a true source, data collection and time syncing those data points are important for later analysis. The current process involves live collection of the ADCS telemetry data while the PhaseSpace system is being recorded only to be post processed at a later time. Development of an API that queries both the Owl Server and the ADCS telemetry stream at the same rate would greatly improve the current CubeSat test bed architecture. It would also be helpful to use a real time operating system to control the Helmholtz cage for on orbit simulations and to dynamically control the ADCS test bed from a GUI that

automatically collects both data sets. Furthermore, the entire IRGF model will not fit on the current ADCS test bed without significant memory upgrades. It would be prudent to investigate a command link via MATLAB and use Wi-Fi to command the ADCS test bed similar to the NPS CubeTas test bed. Work done by Lippert has demonstrated the feasibility of such a GUI. One of the main limitations of the current CubeSat ground station is the dated operating system. Many of the important computational resources such as MATLAB, STK, PhaseSpace, LABView, and even Tera Term have connection and time out issues during testing. The addition of the BTS SMART-DX system installed in the wind tunnel lab has a suite of MATLAB tools to better help the future development of the ADCS test bed ground station as some of the PhaseSpace output files are compatible.

### 5.3.2 Implementation of Magnetic Torque Coils and Attitude Sensors

It was shown in previous research that the torque coils interfere with the IMU sensors. The author installed two torque coils in the current ADCS test bed to research their effects on the magnetometers. However, they were not enabled and tested within the time constraints of this research. If the torque coils are shown to affect the magnetometer data, future research could investigate ways to improve estimation during coil use. The easiest way would be to add a star tracker or sun sensor into QUEST and lower the magnetometer sensor weight in QUEST during magnetic torque coil operation. Another possible solution could use a second external Analog Devices IMU deployed on a solar panel far away from the CubeSat body to mitigate erroneous EMI from the RWA and torque coils. Eventually the torque coils and supporting code should be calibrated for use in a realistic magnetic field typical of a CubeSat in orbit. Furthermore, the second magnetometer used in the research requires calibration and biasing. A better option would be to select another

magnetometer of comparable quality to the primary IMU used in this research.

### 5.3.3 Rigid-Body ADCS Test Bed with Automatic Mass Centering

A center of mass calibration system was designed by Sharp, but not implemented due to CAD model differences with the physical ADCS test bed platform. The system was designed to allow subtle adjustments to masses underneath the ADCS test bed during air bearing operations. With the constant addition and movement of wires to include the PhaseSpace system and supporting battery, balancing the CubeSat before testing became rather time consuming. Integrating a rigid body CubeSat design for AFIT along with an automatic mass balancing system would significantly increase the number of testing and research opportunities during the space vehicle design sequence at AFIT. This research could also produce a better estimate of the moment of inertia matrix for the ADCS test bed which would improve future simulation model accuracy.

### 5.3.4 Fan Assisted Multi-Axes Control

Similar to the Sim-Sat test bed at AFIT, a series of smaller propeller driven fans could be used to simulate three axis control on the ADCS test bed. This would require disabling the $x$- and $y$-axes motors or the integration of an external armature to support at least two fans with ample clearance from the ADCS test bed. Since each motor would also add a torque to the test bed a counter rotating solution should be approached. This idea was demonstrated by Lippert with a custom made counter-rotating quad propeller aerial device on the ADCS test bed. Once calibrated in the desired position the test platform was rebalanced to induce a large angle offset along the $x$- and $y$-axes. During the test the device was able to stabilize itself and remain steady in the desired calibrated position. To use this approach the fan distance from the center of mass of the ADCS test bed should be maximized to increase the moment

arm and decrease the size and power draw of the motor and to reduce potential EMI.

## 5.4 Impacts of Research

The results of this research highlight the sensitivity of the sensors used for spacecraft attitude estimation. Utilizing the Helmholtz cage to provide various field strengths showed that the accuracy of quaternion estimate from QUEST improved in artificially strong magnetic fields. The research removed external EMI from the magnetometer sensor and presented experimental testing to investigate other sources of noise. The variable type mismatch test showed that noise internal to the system can produce an undesirable operating system response. For the first time the AFIT CubeSat ADCS test bed was commanded a full 360° controlled rotation and compared to an external truth source. The discovery of the singularity in the Rodrigues parameters was investigated and will aid in the development and research of future CubeSat ADCS at AFIT.

# Bibliography


1. T. J. Doering, “Development of a Reusable Cubesat Satellite Bus Architecture for the Kysat-1 Spacecraft,” M. S. Thesis, University of Kentucky, 2009.

2. S. Chesi, Q. Gong, V. Pellegrini, R. Cristi, and M. Romano, “Automatic Mass Balancing of a Spacecraft Three-Axis Simulator: Analysis and Experimentation,” Journal of Guidance, Control, and Dynamics, vol. 37, no. 1, pp. 197–206, 2014. [Online]. Available: http://arc.aiaa.org/doi/abs/10.2514/1.60380

3. E. R. Dannemeyer, “Design and Analysis of an Attitude Determination and Con-trol Subsystem (ADCS) for AFIT’s 6U Standard Bus,” M. S. Thesis, Air Force Institute of Technology, Wright-Patterson Air Force Base, Ohio, March 2014.

4. M. L. Tibbs, “Design and Test of an Attitude Determination and Control System for a 6U CubeSat using AFIT’s Cubesat Testbed,” M. S. Thesis, Air Force Institute of Technology, Wright-Patterson Air Force Base, Ohio, March 2015.

5. “National Oceanic and Atmospheric Administration: Geomagnetic Calculators, Maps, Models and Software,” 2015. [Online]. Available: http://www.ngdc.noaa.gov/geomag/models.shtml

6. Wertz, James Richard, David F Everett and J. John, Space Mission Engineering: The New SMAD. Microcosm Press, 2011.

7. D. Miller, “Vibration Analysis of a 12U CubeSat Structural Design,” M. S. Thesis, Air Force Institute of Technology, Wright-Patterson Air Force Base, Ohio, March 2016.

8. “Space Test Program.” [Online]. Available: http://www.kirtland.af.mil/library/factsheets/factsheet.asp?id=6878

9. M. R. Brewer, “CubeSat Attitude Determination and Helmholtz Cage Design,” M. S. Thesis Air Force Institute of Technology, Wright-Patterson Air Force Base,, March 2012.

10. R. D. Loper, “PHYS 519: The Space Enviroment Course Notes,” AFIT Course PHYS 519 Lecture Slides Fall 2015.

11. Hall, Christopher D. "Spacecraft Attitude Dynamics and Control". Virginia Polytechnic Institute and State University, Unpublished Lecture Notes, 2011.

12. K. Bhavani and R. Vancour., “Coordinate Systems for Space and Geophysical Applications,” Technical report, Air Force System Command, Hanscom Air Force Base, Tech. Rep., 1991.

13. M. S. Grewal, L. R. Weill, and A. P. Andrews, “Appendix C: Coordinate Trans-formations,” Global Positioning Systems , Inertial Navigation , and Integration, p. 552, 2007.

14. P. Singla, D. Mortari, and J. L. Junkins, “How to avoid singularity when using Euler angles?” Advances in the Astronautical Sciences, vol. 119, no. SUPPL., pp. 1409–1426, 2005.

15. E. D. Swenson, “MECH 632: Intermediate Spacecraft Dynamics.” AFIT Course MECH 632 Lecture Slides Summer 2015.

16. D. L. Kunz, *Intermediate Dynamics for Aeronautics and Astronautics*. Air Force Institute of Technology, AFIT Course MECH 521 Course Book Fall 2014.

17. B.Wie, *Space Vehicle Dynamics and Control Second Edition*. American Institute of Aeronautics and Astronautics, 2008.

18. M. J. Sidi, *Spacecraft Dynamics and Control: A Practical Engineering Approach*. Cambridge University Press, 1997.

19. J. A. Hess, “Adaptive Nonlinear Estimation of Spacecraft Attitude Dynamics," Ph.D prospectus, Air Force Institute of Technology, Wright-Patterson Air Force Base, Ohio, 2016.

20. Sellers, Jerry Jon, William J Astore, Robert B Giffen and W. J. Larson., *Understanding Space: An Introduction to Astronautics*. Primis, 2000.

21. R. Patrick, “Analysis of a Near Real-Time Optimal Attitude Control for Satellite Simulators,” M. S. Thesis, Air Force Institute of Technology, Wright-Patterson Air Force Base, Ohio, 2016.

22. E. Herbert, “NPSAT1 Magnetic Attitude Control System Algorithm Verification, Validation, and Air-Bearing Tests,” M. S. Thesis, Naval Postgraduate School, Monterey, Ca., 2004.

23. V. L. Pisacane, *The Space Environment and its Effects on Space Systems*. Amer-ican Institute of Aeronautics and Astronautics, 2008.

24. F. L. Markley, “Attitude estimation or quaternion estimation?” Advances in the Astronautical Sciences, vol. 115, no. SUPPL., pp. 102–116, 2003.

25. F. L. Markley and D. Mortari, “Quaternion Attitude Estimation Using Vector Observations,” Journal of the Astronautical Sciences, vol. 48, no. 2, pp. 359–380, 2000.

26. H. W. Ott, *Noise Reduction Techniques in Electronic Systems 2nd Edition,* John Wiley and Sons, Inc, 1989.

27. K. B. Ferreira, P. Bridges, and R. Brightwell, “Characterizing application sensitiv-ity to OS interference using kernel-level noise injection,” 2008 SC - *International Conference for High Performance Computing, Networking, Storage and Analysis*, SC 2008, pp. 1–20, 2008.

28. P. Beckman, K. Iskra, K. Yoshii, and S. Coghlan, "The influence of operating systems on the performance of collective operations at extreme scale," Proceedings - IEEE International Conference on Cluster Computing, ICCC, 2006.

29. Jeffery B. Burl, *Linear Optimal Control: H2 and H-Infinity Methods*. Menlo Park, Ca.: Addison Wesley Longman, Inc.l, 1999.

30. W. E. Wiesel, *Modern Orbit Determination 2nd Edition*. Aphelion Press, 2010.

31. Peter S. Maybeck, *Stochastic Models, Estimation and Control: Volume 1*. Academic Press, 1979.

32. C. Shake, "Spacecraft Attitude Determination System Using Nano-Optical Devices and Linux Software Libraries," Journal of Aerospace Information Systems, vol. 10, no. 8, 2013.

33. C. P. Bridges, S. Kenyon, C. I. Underwood, and M. N. Sweeting, "STRaND : Surrey Training Research and Nanosatellite Demonstrator," 2011.

34. David M. Meissner, "*A Three Degrees of Freedom Test Bed for Nanonsatellite and CubeSat Attitude Dynamics, Determination, and Control,*" Masters Thesis, Naval Postgraduate School, 2009.

35. J. Gerber, "A 3-Axis Attitude Control System Hardware Design for a CubeSat by," M. S. Thesis, University of Stellenbosch, South Africa, 2014.

36. A. Klesh, S. Seagraves, M. Bennett, D. Boone, J. Cutler, and H. Bahcivan, "Dynamically driven Helmholtz cage for experimental magnetic attitude determination," Advances in the Astronautical Sciences, vol. 135, pp. 147–160, 2010.

37. J. C. Springmann and J. W. Cutler, "Attitude-independent magnetometer calibration with time-varying bias," Journal of Guidance, Control, and Dynamics, vol. 35, no. 4, pp. 1080–1088, 2012.

38. E. D. Swenson, "6U CubeSat Interface Control Document," AFIT Tech Report 2015.

39. Honeywell Corp. "Honeywell® HMC6343 Sensor Three-axis Compass with Algorithms."

40. Atmel Corp. "32-bit AVR® Microcontroller: AT32UC3C," pp. 1–1316.

41. PhaseSpace. LLC, "PhaseSpace Impulse X2E User Guide," Tech. Rep., 2015.

42. "Advanced Test and Evaluation TST 303," Defense Acquistion University (DAU) Couse Handbook, Tech. Rep., 2013.

43. T. Gaddis et al., *Starting Out With C++, 4th ed.* Scott Jones Publishers, 2004.

# REPORT DOCUMENTATION PAGE

*Form Approved*
*OMB No. 0704-0188*



| **1. REPORT DATE** *(DD-MM-YYYY)* | **2. REPORT TYPE** | **3. DATES COVERED** *(From - To)* |
|---|---|---|
| 16-06-2016 | Master's Thesis | Oct 2014-Jun 2016 |

**4. TITLE AND SUBTITLE**

Test and Verification of a CubeSat Attitude Determination and Control System in Variable Magnetic Fields

**5a. CONTRACT NUMBER**

**5b. GRANT NUMBER**

**5c. PROGRAM ELEMENT NUMBER**

**6. AUTHOR(S)**

Eric Alan Bassett, Capt., USAF

**5d. PROJECT NUMBER**

**5e. TASK NUMBER**

**5f. WORK UNIT NUMBER**

**7. PERFORMING ORGANIZATION NAME(S) AND ADDRESS(ES)**

Air Force Institute of Technology
Graduate School of Engineering and Management (AFIT/EN)
2950 Hobson Way
WPAFB OH 45433-7765

**8. PERFORMING ORGANIZATION REPORT NUMBER**

AFIT-ENY-MS-16-J-050

**9. SPONSORING / MONITORING AGENCY NAME(S) AND ADDRESS(ES)**

Space Vehicles Directorate
Air Force Research Laboratory
3550 Aberdeen SE, Bldg 497
Kirtland AFB, NM 87117
Timothy J. Shuck, Capt, USAF. (505) 853-4513, timothy.shuck@kirtland.af.mil

**10. SPONSOR/MONITOR'S ACRONYM(S)**

AFRL/RVES

**11. SPONSOR/MONITOR'S REPORT NUMBER(S)**

**12. DISTRIBUTION / AVAILABILITY STATEMENT**

Distribution Statement A. Approved for Public Release; Distribution Unlimited

**13. SUPPLEMENTARY NOTES**

**14. ABSTRACT**

The Center for Space Research and Assurance (CSRA) at the Air Force Institute of Technology (AFIT) continues to explore CubeSat initiatives for solving many current space security issues. Regardless of the mission requirements, the success of the CubeSat on orbit frequently depends on the Attitude Determination and Control System (ADCS) functioning correctly. Previous research at AFIT has demonstrated single axis control on a spherical air bearing test bed incorporated within a Helmholtz cage utilizing artificially strong magnetic fields for better signal to noise ratios which are not experienced on orbit. This research explores the process of redesigning, testing, and programming a new 6U CubeSat ADCS to operate in representative magnetic fields using a three wheel reaction wheel array (RWA). A second external magnetometer is utilized while its effect on the quaternion estimate (QUEST) is characterized. The RWA is modularized and displaced from the ADCS µcontroller by the addition of a separate µcontroller on the RWA to handle Hall sensor interrupts allowing the control and estimation task to run uninterrupted. The displacement of the RWA from the primary ADCS µcontroller, which includes the primary magnetometer, minimizes electromagnetic disturbances caused by the RWA on the magnetometer. A quaternion error Proportional-Integral-Derivative (PID) control law is used to control the ADCS test bed while an external motion capture system captures its true orientation. This research effort shows that the quaternion estimate degrades as the magnetic field strength is reduced. The ambient Earth magnetic field increased the final angle error by 7.1◦ during a 90◦ rotation maneuver when compared to the maximum Helmholtz cage condition.

**15. SUBJECT TERMS**

CubeSat, ADCS, Helmholtz Cage, Air Bearing, RWA, Controller, CubeSat Test Bed

| **16. SECURITY CLASSIFICATION OF:** | | | **17. LIMITATION OF ABSTRACT** | **18. NUMBER OF PAGES** | **19a. NAME OF RESPONSIBLE PERSON** |
|---|---|---|---|---|---|
| **a. REPORT** | **b. ABSTRACT** | **c. THIS PAGE** | | | Dr. Eric D Swenson, AFIT/ENY |
| U | U | U | UU | 154 | **19b. TELEPHONE NUMBER** *(include area code)* (937)255-3636 x.7479; eric.swenson@afit.edu |

**Standard Form 298 (Rev. 8-98)**
**Prescribed by ANSI Std. Z39.18**